UNIVERSITY OF OKLAHOMA

GRADUATE COLLEGE

STUDY OF TRANSPORT PHENOMENA IN TURBULENT CHANNEL FLOWS USING DIRECT NUMERICAL SIMULATION AND LAGRANGIAN SCALAR TRACKING

A DISSERTATION

SUBMITTED TO THE GRADUATE FACULTY

in partial fulfillment of the requirements for the

Degree of

DOCTOR OF PHILOSOPHY

By

QUOC TAN NGUYEN
Norman, Oklahoma
2016

Downloaded from SHAREOK. Persistent Handle URL: https://hdl.handle.net/11244/34749

STUDY OF TRANSPORT PHENOMENA IN TURBULENT CHANNEL FLOWS USING DIRECT NUMERICAL SIMULATION AND LAGRANGIAN SCALAR TRACKING

A DISSERTATION APPROVED FOR THE
SCHOOL OF CHEMICAL, BIOLOGICAL AND MATERIALS ENGINEERING

BY

_____
Dr. Dimitrios V. Papavassiliou, Chair

_____
Dr. Prakash Vedula

_____
Dr. Edgar A. O' Rear III

_____
Dr. Bin Wang

_____
Dr. Robert L. Shambaugh

© Copyright by QUOC TAN NGUYEN 2016
All Rights Reserved.

To my beloved family and LyLy

Acknowledgements

Words cannot describe my sincere appreciation to my advisor, Professor Dimitrios Papavassiliou. He has fulfilled my dream by giving me this wonderful opportunity to pursue my Doctorate degree at the University of Oklahoma. I thank him for his great support and patience in teaching me to become an independent researcher with high integrity and respect to others. He has always been available to help me in my most difficult times, and has always made me feel comfortable working with him. It is my pleasure to get to know him in person and to work with him as his student. I will always be appreciative of this wonderful time, and will always remember everything he has taught me.

I also would like to thank my committee members, Dr. Prakash Vedula, Dr. Bin Wang, Dr. O' Rear, Dr. Shambaugh, Dr. Alberto Striolo and Dr. Takumi Hawa for their comments and contribution in this work. They have brought their expertise in different fields to enhance my research. The computational resources provided by OU Supercomputing Center for Education & Research (OSCER) and XSEDE is greatly appreciated.

I would not have been able to finish this six year long journey without love and encouragement from my family and friends. I thank my family for always standing behind me. I thank my friends at CBME and members in my group, Chiranth, Kalyan, Ruby, Minh, Mesude and Frank, for helping me with my research and many great ideas and discussion. I save special thanks to LyLy for her unconditional love and support. Last but not least, I thank the University of Oklahoma for giving me an ideal environment to work and realize my dream.

Table of Contents

Acknowledgements iv

List of Tables viii

List of Figures ix

Abstract xvii

Chapter 1. Introduction 1

1.1 Turbulent Drag Reduction on Superhydrophobic Surfaces 1

1.1.1 Slip Boundary Condition 1

1.1.2 Superhydrophobic Surfaces (SHSs) 3

1.1.3 Slip on Superhydrophobic Surfaces – Laminar Flows 4

1.1.4 Slip on Superhydrophobic Surfaces – Turbulent Flows 6

1.2 Turbulent Dispersion 9

1.3 Turbulent-Laminar patterns in Poiseuille-Couette flow 11

Chapter 2. Numerical Methodology 16

2.1 Direct Numerical Simulation (DNS) 16

2.2 Lagrangian Scalar Tracking (LST) 17

Chapter 3. Turbulent plane Poiseuille-Couette flow as a model for fluid slip over Superhydrophobic Surfaces 21

3.1 Simulation Parameters and Procedure 21

3.2 Results and discussion 23

3.2.1 Turbulent flow statistics 23

3.2.2 Two-point velocity correlation coefficients 27

3.2.3 Reynolds stress analysis by quadrants 29

3.2.4 Vorticity magnitude and kinetic energy dissipation rate 31
3.2.5 Anisotropic turbulence and mechanism of drag reduction over superhydrophobic surfaces 33
Chapter 4. Flow-induced Separation in Wall Turbulence 50
4.1 Introduction 50
4.2 Simulation parameters and procedure 50
4.3 Results and discussion 52
4.3.1 Flow-induced separation 52
4.3.2 Separation Mechanism 58
4.3.3 A Model for Particle Displacement 62
Chapter 5. Probability Density Function of a puff dispersing from the channel wall 72
5.1 Introduction 72
5.2 Simulation parameters and procedure 75
5.3 Results and discussion 76
5.3.1 Statistical Analysis 76
5.3.2 Three-parameter Gamma distribution 82
5.3.3 Model Testing 92
5.3.4 Application of the Gamma 3P distribution model 98
Chapter 6. Turbulent-Laminar Patterns in Poiseuille-Couette flow 104
6.1 Introduction 104
6.2 Simulation parameters and procedure 105
6.3 Results and discussion 107
6.3.1 Results at Re = 323 (Re_τ = 24) 107

6.3.2 Results at Re = 1247 (Re_τ = 80) 113

Chapter 7. Conclusions and Future work 117

7.1 Turbulent drag reduction over Superhydrophobic Surfaces 117

7.2 Flow-induced separation in wall turbulence 118

7.3 Probability density function of a puff dispersing from the channel wall 118

7.4 Turbulent-Laminar patterns in transitional turbulence 119

7.5 Future Work 120

7.5.1 Flow-induced separation in wall turbulence 120

7.5.2 Probability density function of a puff dispersing from the channel wall .. 120

Bibliography 122

List of Tables

Table 4.1 Summary of cases of low and high Sc, in which separation is observed using the 0.5% purity criterion. The transition times τ_{95} and τ_{III} are also presented. 59

Table 4.2 Batchelor's constant b for different Sc 65

Table 5.1 Values of bin size for different Sc numbers 77

Table 5.2 P-values obtained from 3 pdf models: a) Inverse Gaussian; b) 3P Gamma; c) 3P Weibull with different Sc numbers at different time. Empirical data from one simulation were used in this case to determine the most appropriate pdf model for use, as P-values do not vary much between different simulations 79

List of Figures

Figure 1.1 Schematic diagram of slip at a fluid-solid interface 13

Figure 1.2 Computed turbulent-laminar pattern at Re = 350 in plane Couette flow by Tuckerman & Barkley (52). Above is the kinetic energy at y = 0, midway between bounding plates at y = ± 1 which move to the right and left in the streamwise direction. Turbulent bands consist of streamwise streaks and vortices. The bands are oriented in the direction denoted by x at an angle of 24^o from the streamwise direction, and are separated by a wavelength of 40 in the direction of the pattern wavevector, denoted by z. 14

Figure 1.3 Time series of spanwise velocity at 32 points along a line in the midplane x = y = 0 as the Reynolds number is decreased. Results are from a numerical study of plane Couette flow by Tuckerman & Barkley (54)..... 15

Figure 1.4 Turbulent-laminar patterns observed in a direct numerical simulation of plane Poiseuille flow by Tsukahara (55). Contour of streamwise fluctuating velocity in an (x,z) – plane at $y/\delta \approx 0.5$ for $Re_\tau = 80$. The direction of the mean flow is from left to right..... 15

Figure 2.1 Plane Poiseuille flow configuration 20

Figure 2.2 Plane Couette flow configuration 20

Figure 3.1 Mean streamwise velocity with no slip boundary condition (GWPH: data points from Gunther *et al.*(64); NKK: data points from Nakabayashi *et al.*(37), dashed lines: law of the wall) 36

Figure 3.2 Mean velocity profile in Poiseuille and Poiseuille-Couette flow with $U_s^+ = 1$, 2 and 4 (KK: data from Kuroda & Kasagi (79)). The inset figure to the right includes

results for different ratio of the Couette over the Poiseuille Reynolds number, denoted as γ (γ = Us + Ucenterline +). 36

Figure 3.3 Reynolds stress profile in Poiseuille and in Poiseuille-Couette flow with U_s^+ = 1, 2, and 4 (GWPH: data points from Gunther *et al.* (64); TK: data points from Thurlow & Klewicki (38))..... 37

Figure 3.4 Root mean squared velocity fluctuations for the Poiseuille-Couette simulations: (a) Streamwise velocity; (b) Normal velocity; (c) Spanwise velocity (GWPH: data points from Gunther *et al.*(64); NKK: data points from Nakabayashi *et al.*(37); TK: data points from Thurlow & Klewicki (38)). 38

Figure 3.5 Turbulent kinetic energy production in Poiseuille and Poiseuille-Couette flow with U_s^+ = 1, 2 and 4 (GWPH: data points from Gunther *et al.*(64); NKK: data points from Nakabayashi *et al.*(37))..... 39

Figure 3.6 Drag reduction obtained in Poiseuille-Couette flow with different values of U_s^+ (FKK: theoretical prediction of Fukagata *et al.* (82)) 39

Figure 3.7 Two-point correlation coefficient with streamwise separation for the streamwise fluctuating velocity in (a) Poiseuille, and (b) Poiseuille-Couette flow with U_s^+= 4 40

Figure 3.8 Two-point correlation coefficient with spanwise separation for the streamwise fluctuating velocity in (a) Poiseuille and (b) Poiseuille-Couette flow with U_s^+ = 4 41

Figure 3.9 Two-point correlation coefficient with spanwise separation for the normal fluctuating velocity in (a) Poiseuille and (b) Poiseuille-Couette flow with Us+ = 4 42

Figure 3.10 Two-point correlation coefficient with spanwise separation for the streamwise fluctuating velocity in Poiseuille and Poiseuille-Couette flow with Us+ = 4. This is calculated at the y-location of the maximum turbulent kinetic energy production. It is seen that there is an increase of the length scale in the spanwise direction, designated by the point of zero-crossing of the correlation coefficient. 43

Figure 3.11 Two-point correlation coefficient with spanwise separation for the normal fluctuating velocity in Poiseuille and Poiseuille-Couette flow with $U_s^+ = 4$. This is calculated at the *y*-location of the maximum turbulent kinetic energy production. It is seen that there is an increase of the length scale in the spanwise direction, designated by the point of zero-crossing of the correlation coefficient. 43

Figure 3.12. Fractional contribution of Reynolds stress of (a) quadrant 1 and (b) quadrant 3 44

Figure 3.13. Vorticity magnitude in the Poiseuille and Poiseuille-Couette flow with U_s^+ = 1, 2, and 4 45

Figure 3.14. Root mean square of fluctuating vorticity in (a) x-direction, (b) y-direction, (c) z-direction in Poiseuille and Poiseuille-Couette flow with $U_s^+ = 1$, 2, and 4. 46

Figure 3.15. Ratio of the streamwise and spanwise fluctuating vorticity components over the total fluctuating vorticity. ($Wx2$ and $Wz2$ are the mean square of the streamwise and spanwise fluctuating vorticity, respectively, and $W2$is the mean square of the fluctuating vorticity vector.)..... 47

Figure 3.16. Total dissipation rate in Poiseuille and Poiseuille-Couette flow with U_s^+ = 1, 2 and 4. 47

Figure 3.17. The Lumley triangle on the plane of the invariants II and III of the Reynolds stress anisotropy tensor: (a) Points close to the moving wall; (b) Points close to the stationary wall. The inset figures focus on the location of zero crossing of the Reynolds stress 48

Figure 3.18. Ratio of turbulence intensity in the streamwise direction over intensity in (a) the normal direction, and (b) the spanwise direction. The ratio increases with an increase of the slip velocity. 49

Figure 4.1 Locations of markers with Sc = 0.1 (green) and 500 (crimson) at different times from their simultaneous release: a) t = 50; b) t = 100; c) t = 220. Clear separation between the two clouds is observed in panel (b), while a thin overlap region is observed. 55

Figure 4.2 Number of markers in the overlap region, Nov, when markers with Sc = 0.1 are released simultaneously with markers of different Sc. a) Number of markers from the leading cloud, Sc = 0.1; b) Number of markers from the higher Sc trailing cloud. . 56

Figure 4.3 Number of markers in the overlap region when markers with Sc = 0.1 and 2400 are simultaneously released at different initial vertical positions; a) markers of the leading cloud; b) markers of the trailing cloud. 57

Figure 4.4 Separation time as a function of the ratio R_t of the τ_{III} of the low Sc over the τ_I of the high Sc. The solid line is Equation (4.4)..... 60

Figure 4.5 Mean displacement of particles with different Sc in: a) streamwise direction; b) vertical direction. Data obtained from LST simulations. 63

Figure 4.6 Prediction of vertical displacement in zone I: comparison between the model of Equation (4.8) (lines marked with open circles) and LST results (lines without any markings). 64

Figure 4.7 Mean vertical displacement of particles in the log layer. Data obtained from LST simulation. 66

Figure 4.8 Mean vertical displacement of different Sc. Results obtained from the LST data (lines without markers) and with our model based on Equations (4.8)-(4.10) are presented (lines marked with open circles). 67

Figure 4.9 Mean streamwise displacement of different Sc: a) Sc = 0.1, b) Sc = 6, c) Sc = 100. Results are obtained from LST data (lined without markers) and Batchelor's model (lines marked with open circles)..... 70

Figure 4.10 Front and back boundaries of 99% of population of clouds in the streamwise direction, using mean displacement and normal distribution to predict the concentration distribution. (a) Prediction for clouds with Sc = 0.7 and 30000 and (b) prediction for clouds with Sc = 6 and 7500..... 71

Figure 5.1 Locations of markers with Sc = 0.1 (green) and 500 (crimson) at different times from their simultaneous release: a) t = 50; b) t = 100; c) t = 220. Clear separation between the two clouds was observed in panel (b), while a thin overlap region was observed at $x \approx 1000$ - 1200 in panel (c). (Only the bottom half of the channel is shown, from $y = 0$ to 300) 73

Figure 5.2 Plotting of Xbmin and 3rd parameters from Inverse Gaussian, 3P Gamma and 3P Weibull distribution for one simulation. a) Sc = 6; b) Sc = 100; c) Sc = 2400 .. 86

Figure 5.3 a) Plotting of Mean streamwise displacement versus $t^{1.5}$ for different Sc numbers. b) The coefficient g was found to be a function of $Sc^{-0.5}$..... 89

Figure 5.4 (a) Plotting of mode values versus $t^{1.5}$ for different Sc numbers. (b) The coefficient k was found to be a function of $Sc^{-0.5}$ 90

Figure 5.5 Scaling of X_{bmin} with $Sc^{1/2}$ for different Sc at different times. Results were taken average from 2 different simulations. o : simulation results; – : line obtained from equation (5.11)..... 92

Figure 5.6 P-value obtained from goodness-of-fit test by using our pdf model and empirical data from 2 realizations; a) Sc = 6; b) Sc = 200; c) Sc = 1000 94

Figure 5.7 CDF error between using our pdf model and empirical data from 2 realizations for different Sc number. a) Sc = 6 at t^+ = 10; b) Sc = 6 at t^+ = 50; c) Sc = 200 at t^+ = 20; d) Sc = 200 at t^+= 50; e) Sc = 1000 at t^+ = 20; f) Sc = 1000 at t^+= 40.... 97

Figure 5.8 PDF of 2 puffs of particles with Sc 50 and 2400 at t+=50. Overlap area was clearly observed in this case, which implies that complete separation could not happen 99

Figure 5.9 Use of Gamma 3P distribution to calculate number of particles in the overlap region and compare with results from DNS-LST method, pair of Sc numbers 6 and 2400; a) number of particles of the leading puff; b) number of particles of the following puff. The Adjusted 3P Gamma line adds 100 more particles to the number of particles of the leading puff in the overlap region. 100

Figure 5.10 Use of Gamma 3P distribution to calculate number of particles in the overlap region and compare with results from DNS-LST method, pair of Sc numbers 50 and 2400; a) number of particles of the leading puff; b) number of particles of the

following puff. The Adjusted 3P Gamma line adds 100 more particles to the number of particles of the leading puff in the overlap region. 102
Figure 5.11 Use of Gamma 3P distribution to calculate number of particles in the overlap region and compare with results from DNS-LST method, pair of Sc numbers 6 and 7500; a) number of particles of the leading puff; b) number of particles of the following puff. The Adjusted 3P Gamma line adds 100 more particles to the number of particles of the leading puff in the overlap region. 103
Figure 6.1 A Ventricular Assist Device (VAD) prototype 105
Figure 6.2. Stress distribution in (a) plane Couette flow; Poiseuille-Couette flow with (b) R = 0.1; (c) R = 0.2 109
Figure 6.3. Contour plot of streamwise fluctuating velocity at midway plane y = 0 in a plane Couette flow (R=0). X is the streamwise direction 110
Figure 6.4. Streamwise fluctuating velocity with magnitude of 6 in the Couttle channel flow 110
Figure 6.5. Contour plot of streamwise fluctuating velocity at midway plane y = 0 in a plane Poiseuille-Couette flow (R=0.1). X is the streamwise direction 111
Figure 6.6. Fluctuating velocities in streamwise and spanwise direction at two random magnitude values at the midway plane y = 0 of a plane Couette flow (R=0) and plane Poiseuille-Couette flow (R=0.1) 112
Figure 6.7. Shear stress distribution in (a) plane Couette flow; (b) plane Poiseuille-Couette flow at R = 0.2; (c) plane Poiseuille-Couette flow at R = 0.5 115
Figure 6.8. Streamwise fluctuating velocity with magnitude of 4 at a midway plane y = 0 in a plane Couette flow (R=0) and plane Poiseuille-Couette flow with R = 0.5 115

Figure 6.9. Streamwise fluctuating velocity with magnitude of 5 at a midway plane y = 0 in a plane Couette flow (R=0) and plane Poiseuille-Couette flow with R = 0.5..... 116

Abstract

Study of turbulence has been carried out for several decades due to its popularity and importance in many engineering disciplines. In fact, turbulence is the most observed flow regime in nature and industry. Due to its significantly high transport rate compared to laminar flow, turbulence has found great applications and impact in several fields and attracted lots of interest.

Recent advancement of microfluidic devices has led to a desire to increase flow velocity in order to reduce length scales and time scales associated to many mixing processes happening within these devices, as those length scales and time scales associated with mixing in laminar flows are not suitable for practical applications. Researchers have recently employed superhydrophobic surfaces to increase volumetric flow rate and Reynolds numbers of flows inside these devices, hence led to great interest in study and application of superhydrophobic surfaces. On the other hand, turbulent drag force remains a great concern in many large scale applications, for i.e. automotive and ship building industry, as great amount of energy is consumed to compensate for loss of momentum. Recent studies have suggested superhydrophobic surfaces as a method to reduce skin-friction drag, thus reduce energy consumption. Though application of this type of surface in micro-scale devices has been well understood, the effect of such surface on the skin-friction drag in large-scale flows, such as turbulent flows around a ship, remains to be investigated. In this study, plane Poiseuille-Couette flow is simulated as a model for fluid slip over superhydrophobic surfaces. The purpose of the study is to explore the details of how specific slip affects the turbulence structure and the coherent structures in the viscous wall region and how

changes in these structures compare with other cases of turbulence drag reduction. The study also aims to provide further insights into the mechanism of turbulent drag reduction in cases of specified slip at the wall through study of turbulent flow statistics, quadrant analysis of the Reynolds stress, two-point correlations and trajectories on anisotropy invariant maps.

Another great impact of turbulence in engineering is its ability to enhance mixing, due to its high momentum and mass transfer rate. Significant studies have been done in turbulent dispersion and related issues. However, we present here a case where the opposite happens, in which simulation results indicate that particles can separate near the wall of a turbulent channel flow without use of any other means, given that they have sufficiently different Schmidt numbers. The physical mechanism of the separation is understood when the interplay between convection and diffusion, as expressed by their characteristic time scales, is considered, leading to the determination of the necessary conditions for a successful separation between particles.

Throughout my research, the combination of Direct Numerical Simulation (DNS) and Lagrangian Scalar Tracking (LST) has been widely used to simulate turbulent flow field and track trajectories of heat and mass markers traveling along with the flow. While this technique has proven to be of high fidelity, its computational cost remains a concern for many researchers. An attempt has been made herein to explore the form of the particles distribution, and we present the finding that Gamma 3P distribution is an appropriate probability density function (pdf) for use in predicting location and concentration distribution of puffs of particles with different Schmidt numbers (Sc) diffusing from the wall of a channel. Estimation of parameters of the

Gamma 3P distribution was successfully obtained. The use of Gamma 3P distribution could be found in estimating particles separation at different purity criteria, as well as predicting diffusion of particles in the channel for other applications.

Study of different wall-bounded shear flows at transitional regime also revealed the coexistence of turbulent-laminar patterns formed at an oblique angle to the flow direction. These patterns, however, behave differently in plane Couette flow and Poiseuille flow even at the same Reynolds number. This study would help shed some light on the mechanics of these special patterns, which prove to be important in many fluidic devices operating at transition regime.

Chapter 1. Introduction

1.1 Turbulent Drag Reduction on Superhydrophobic Surfaces

1.1.1 Slip Boundary Condition

For decades of studying fluid dynamics, researchers have been using the no-slip boundary condition for viscous fluids, which basically states that the fluid will have zero velocity relative to the solid boundary. Although this boundary condition has been accepted almost universally as the proper boundary condition to impose at the solid-liquid interface, its validity has been subject of debate extensively throughout the 19th and early 20th century by great amount of scientists (1). It is worth noticed that the no-slip boundary condition is no more than a convenient approximation that has been found to hold under most normal flow conditions (2).

The concept of a slip boundary condition was first introduced by Navier (3) and is shown schematically in Figure 1. In Navier's model, the magnitude of the slip velocity, u_o, is proportional to the magnitude of the shear rate experienced by the fluid at the wall

$$u_o = b\left|\frac{\partial u}{\partial y}\right| \qquad (1.1)$$

where b is the slip length. A study of gas flowing past a solid surface predicted a slip length on the order of the mean free path of the fluid, λ (4). Slip lengths on the same order were also reported in other studies. Therefore, for nearly all macroscopic flows of simple fluids, the slip length is so small that it can be neglected, b = O (1nm), and the no-slip boundary condition could be used without loss of accuracy.

Recent advancement in microfluidic devices has raised a desire to develop fluid-surface parings that can achieve slip lengths on the order of micrometers rather than nanometers. It was proved that the volume flow rate between two infinite parallel plates could be significantly enhanced if and only if the slip length is on the order of the channel height (5). For microfluidic devices, this means that slip length must be on the order of micrometers, rather than nanometers. Several studies have focused on quantifying the magnitude of the slip length and its dependence on parameters such as wettability and surface roughness (6-8)

The wettability of a surface is defined by the spreading coefficient, $S = \gamma_{SV} - \gamma_{LV} - \gamma_{LS}$, where γ_{SV}, γ_{LV}, and γ_{LS} are the solid-vapor, liquid-vapor and liquid-solid interfacial tensions, respectively (9). The solid is fully wetted by the liquid if $S > 0$, whereas for $S < 0$, the solid is only partially wet by the liquid, which forms a spherical end cap with an equilibrium contact angle defined by Young's law as $\theta = \cos^{-1}[(\gamma_{SV} - \gamma_{LS})/\gamma_{LV}]$. The surface is considered hydrophilic for $\theta < 90^o$, while for those with $\theta \geq 90^o$, the surface is hydrophobic. Many studies have found that surface hydrophobicity could produce slip lengths much larger than the mean free path (10, 11). Values of slip lengths greater than 40 molecular diameters were reported, which were not observed on hydrophilic and even moderately hydrophobic surfaces with $\theta < 100^o$. However, it was also found that slip length larger than a few tens of nanometers cannot be achieved. Creating slip lengths on the order of micrometers for it to be useful in practical applications requires the use of Superhydrophobic surfaces (SHSs).

1.1.2 Superhydrophobic Surfaces (SHSs)

A superhydrophobic surface is arbitrarily defined as a surface with a contact angle of higher than 150^{o} between the surface and a drop of fluid resting on it (12). This type of surface has been widely observed in nature (13-15). The lotus leaf is one of the most well-known and studied examples of superhydrophobic and water repellent natural surfaces (16-19). The water droplets roll on the surface carrying away dirt and debris. The self-cleaning property of the hydrophobic lotus leafs is attributed to the hydrophobic epicuticular wax associated with the micro/nanoscale hierarchical architectures formed by cilium-like nanostructures on the top of the microscale papillae. Other plant leaves show the same behavior of lotus leaf and are also micro/nanotextured. The taro leaf possesses a surface texture characterized by micrometer elliptic protrusions uniformly distributed on the surface.

It has been known that how a droplet of a liquid sits and rolls on a surface is determined by both the surface chemistry and the surface roughness or topography (16, 20, 21). The difference between a hydrophobic surface and a superhydrophobic surface lies not in the surface chemistry, but in the micro- or nanoscale surface roughness. A flat and smooth hydrophobic surface exhibiting an equilibrium contact angle of 115^{o} could be converted into a superhydrophobic surface exhibiting a contact angle greater than 150^{o} by roughening it, even without altering any surface chemistry (22). Synthetic superhydrophobic surfaces have recently been developed that are capable of obtaining contact angles that approach $\theta \approx 180^{o}$ with little to no measurable contact-angle hysteresis, which makes a water drop on it unstable and move easily across the surface (23-25).

1.1.3 Slip on Superhydrophobic Surfaces – Laminar Flows

Superhydrophobic surfaces were first tested in its ability to create larger slip length within laminar flows. As microfluidic devices are getting more popular, it has become extremely desirable to develop fluid-surface parings that could achieve slip lengths on the order of micrometers. This is explained as we take, for example, a pressure-driven flow between two infinite parallel plates separated by a distance H. If one of these plates support slip, the volume flow rate per unit depth is given by

$$q = \frac{H^3}{4\mu}\left(-\frac{dp}{dx}\right)\left[\frac{1}{3} + \frac{b}{b+H}\right] \qquad (1.2)$$

For a given pressure gradient, dp/dx, and fluid viscosity, μ, the volume flow rate, or effect of shear-free air-water surface on velocity profile, would be considerably enhanced if the slip length is on the order of the channel height.

Several experiments have been conducted with low Reynolds number flows over micro- or nano-textured surfaces, coated with Teflon or other hydrophobic materials. In flows over superhydrophobic surfaces, the boundary condition experienced by the fluid in contact with the solid is no slip; however, the air-water interfaces supported between the micro- or nanofeatures are shear-free. Ou and colleagues (26, 27) used a series of lithographically etched and silanized silicon surfaces with precisely controlled microsurface topology consisting of regular arrays of microposts and microridges to study effect of topological changes on the flow. They were able to obtain drag reductions greater than 40%, with slip length greater than 25μm. Gogte and colleagues (28) examined effects of textured superhydrophobic surfaces for both droplets moving down an inclined surface and an external flow near the surface (hydrofoil). They found evidence of appreciable drag reduction in the presence of surface texture combined with

superhydrophobic coating. While the highest drop velocities were achieved on surfaces with irregular textures and characteristic feature size of roughly 8μm, drag reduction on the order of 10% or higher was obtained with application of the same surface in a water tunnel. The authors explained the behavior as a result of reduction of the contact area between the surface and the fluid, which can be interpreted in terms of changing the macroscopic boundary condition to allow nonzero slip velocity. Another study by Tretheway and Meinhart (29), though performed on hydrophobic microchannel walls, has also found a slip length of approximately 1μm. They found that when the surface was hydrophilic (uncoated glass), the measured velocity profiles were consistent with solutions of Stokes' equation and the well-accepted no-slip boundary condition. However, when the microchannel surface was coated with a 2.3 nm thick monolayer of hydrophobic octadecyltrichlorosilane, an apparent velocity slip was measured above the solid surface and was approximately 10% of the free-stream velocity. Though for a slip length of 1μm, slip flow is negligible for length scales greater than 1mm, but must be considered at the micro- and nano scales. Choi and Kim (30) engineered a nanostructured superhydrophobic surface that minimizes the liquid-solid contact area so that the liquid flows predominantly over a layer of air. The surface has demonstrated dramatic slip effects with a slip length of approximate 20μm for water flow and 50μm for 30 weight % glycerin. These studies have confirmed the existence of liquid slip over superhydrophobic surfaces, when most of the flows are in laminar state.

1.1.4 Slip on Superhydrophobic Surfaces – Turbulent Flows

Even though effects of superhydrophobic surfaces on velocity profile of flows in microfluidic devices are evidence, the effect on skin-friction drag in large-scale flows is still unclear. Fundamentally, the superhydrophobic drag-reduction mechanism should be independent of whether the flow is laminar or turbulent. It is because in turbulent flows, there exists a thin laminar sublayer exists very near to the wall, to a height, y, in wall units of $y^+ = \frac{y}{\nu}(\frac{\tau_w}{\rho})^{1/2} = 5$. However, the question is that whether the influence of the shear-free air-water interface on the velocity profile extends into the chaotic region above the laminar sublayer and has dramatic effect on drag reduction.

One of the pioneer works in studying effects of superhydrophobic surfaces in turbulence was that of Min and Kim (31). They performed turbulent channel flow simulations at a friction Reynolds number of Re_τ = 180 with an arbitrary, but not unreasonable, slip length boundary in both parallel and perpendicular to the flow direction. Their results demonstrated a decrease in wall shear stress with increasing slip length applied parallel to the flow direction, but an increase in wall shear stress for slip applied perpendicular to the flow direction. This work demonstrated that flow slip at the surface could help achieve skin-friction drag reduction in turbulent boundary layers, at least in principle.

Another DNS study was performed by Martell et al. (32, 33) in which drag reduction performance of syperhydrophobic surfaces in turbulent channel flow at friction Reynolds numbers of $Re_\tau \approx 180$, $Re_\tau \approx 395$ and $Re_\tau \approx 590$ was investigated. The top surface of each microfeature was taken to be no slip, whereas the suspended liquid-gas interface between the microfeatures was simulated as flat and shear-free. One side

of the microchannel was modeled as superhydrophobic, while the other side has a no-slip boundary condition. Their results showed a slip velocity and drag reduction that increase with both the increasing microfeature spacing and surface coverage of the shear-free air-water interface. For the largest microfeature spacing, an average slip velocity over 80% of the bulk velocity was obtained, and the wall shear stress reduction was found to be greater than 50%. Their work provides evidence that superhydrophobic surfaces are capable of reducing drag in turbulent flow situations by manipulating the laminar sublayer. The mean velocity profile near the superhydrophobic wall continues to scale with the wall shear stress and the log layer is still present, but both are offset by a slip velocity that is primarily dependent on the microfeature spacing.

Only a few experimental studies of superhydrophobic drag reduction in turbulence are available. Daniello et al. (34) performed an experiment using a rectangular flow cell with smooth and superhydrophobic polydimethylsiloxane (PDMS) walls with 30μm and 60 μm wide microridges spaced 30 μm and 60 μm apart, respectively. They performed pressure-drop and PIV measurements to investigate effects of SHSs on drag reduction in turbulent flows at $2000 < Re < 10{,}000$, with transitional effects considered to persist up to $Re = 3000$. Effect of the superhydrophobic wall was not observed for low-Re experiments. This is, however, not unexpected for flows in laminar or transitional regime. For pressure driven flow between two infinite parallel plates, the volume flow rate could only be significantly increased if the slip length is comparable to the channel height. Based on previous laminar regime studies over similar superhydrophobic micro-features, the slip length was approximately 25 μm and independent of Reynolds number (27). In their

experiment, slip length at this order could produce drag reduction of approximately 1% only. The increase of Reynolds numbers, however, led to substantial increase in slip velocity along the superhydrophobic wall and drag reduction. The maximum drag reduction from pressure-drop measurements approached 50%, whereas slip lengths of 80 μm were observed at the largest Reynolds number tested. This phenomena could be explained using analytical solutions developed by Philip (35, 36), in which the influence of the shear-free air-water interface on the velocity profile was shown to extend into the flow at a distance roughly equal to the microridge spacing. For the superhydrophobic surface to impact the turbulent flow, the spacing must approach the thickness of the viscous sublayer. As the Reynolds number is increased, the viscous sublayer thickness is decreased in dimensional form, thus lead to increase of impact of the superhydrophobic surface on the slip velocity and drag reduction.

While the above studies showed that drag reduction can be obtained in turbulent flows over superhydrophobic surfaces and that slip boundary conditions are appropriate to use when simulating turbulent flows over SHSs, the details of how specific slip affects the turbulence structure and the coherent structures in the viscous wall region, and how changes in these structures compare with other cases of turbulence drag reduction need further exploration. The present work provides further insights into the mechanism of turbulent drag reduction in cases of specified slip at the wall. The slip is simulated with the use of a Poiseuille-Couette type of flow. Poiseuille-Couette flow has been simulated in the past (37, 38), but its use to examine the flow structure and the implications for drag reduction has been employed by Spencer *et al.* (39) for low Reynolds number flow. The analysis herein covers turbulent flow statistics, quadrant

analysis of the Reynolds stress, two-point correlations, turbulent vorticity and trajectories on anisotropy invariant maps. This detailed examination provides an understanding of the mechanism by which finite slip velocity at the wall affects flow structures and leads to drag reduction.

1.2 Turbulent Dispersion

The dispersion of particles by molecular means (i.e, Brownian motion) from the source in x-direction has been described earlier by Einstein (40), in which he developed a relation that describes dispersion of particles in term of the mean-squared displacement from the source in the streamwise direction:

$$\frac{d\overline{X^2}}{dt} = 2D \qquad (1.3)$$

where D is the molecular diffusivity. Taylor (41) developed a similar relation for the rate of dispersion of fluid particles from a point source in homogeneous, isotropic turbulence:

$$\frac{d\overline{X^2}}{dt} = 2\overline{u^2}\int_0^t R^L(\tau)d\tau \qquad (1.4)$$

where $\overline{u^2}$ is the mean-square of the x-component of the velocity of fluid particles and R^L is the Lagrangian correlation coefficient. An important implication of Taylor's equation is that the history of the particle motion affects the rate of dispersion through R^L. At small times, the Lagrangian correlation coefficient is close to one, making the dispersion increases with time to the second power. At large times $R^L = 0$, and thus the dispersion changes linearly with time. At large times, the dispersion rate is a constant given by

$$\frac{d\overline{X^2}}{dt} = 2\overline{u^2}\tau^L \qquad (1.5)$$

where the Lagrangian time scale is defined as

$$\tau^L = \int_0^\infty R^L(\tau)d\tau \qquad (1.6)$$

Dispersion of heat or mass markers introduces an additional complication, as they could move off of the fluid particle on which they travel as a result of molecular diffusion. This makes the trajectory of a scalar marker in the flow field does not coincide with the trajectory of a fluid particle. A relation for dispersion in this case was developed by Saffman (42) by using a material autocorrelation function R_d^L, which correlates fluid velocity components along the trajectories of markers instead of fluid particles. The dispersion was expressed as below

$$\overline{X^2} = 2\overline{u^2}\int_0^t (t-\tau)R_d^L(\tau)d\tau + 2Dt \qquad (1.7)$$

with

$$R_d^L(\tau) = \frac{1}{3}\frac{\overline{V_i(\vec{x}_o,t_o)V_i(\vec{x}_o,t_o+\tau)}}{\overline{u^2}} \qquad (1.8)$$

where $V_i(\vec{x}_o, t_o)$ is the ith component of the fluid velocity at the location $\vec{X}(\vec{x}_o, t_o)$ of a marker that was released at location $\vec{x}_o$ at t = 0. The main difference between the material autocorrelation and the Lagrangian correlation is that the former correlates fluid velocity components along a scalar marker trajectory, instead of along the trajectory of fluid particles. Note that both the theories developed by Taylor and Saffman were for homogeneous and isotropic turbulence.

Corrsin (43) studied line source diffusion in a homogeneous shear flow with a constant mean velocity gradient. The Lagrangian dispersion in the direction of the flow,

X, was found to be different from the dispersion in the direction of the velocity gradient, Y, which is described by Taylor's analysis. It is

$$Y = \int_0^t v(t_1)dt_1 \qquad (1.9)$$

$$X = \int_0^t [\frac{d\overline{U}}{dy} Y(t_1) + u(t_1)]dt_1 \qquad (1.10)$$

where u and v are the particle velocities in the direction of the flow and in the direction of the velocity gradient, respectively. For large times the dispersion becomes

$$\overline{Y^2} = 2\overline{v^2}\tau_y^L t \qquad (1.11)$$

$$\overline{X^2} = \frac{2}{3}(\frac{d\overline{U}}{dy})^2\overline{v^2}\tau_y^L t^3 \qquad (1.12)$$

where τ_y^L is the Lagrangian timescale in the y-direction.

The behavior of a large number of passive scalar markers, as described by Taylor, Saffman and Corrsin, is fundamental to passive scalar transport using the Lagrangian framework. Based on Taylor's theory, Hanratty (44) developed a method to study turbulent heat transfer in wall turbulence, in which he used the dispersion of heat particles from an infinite number of continuous line sources of heat at one wall to describe a hot plate and an infinite number of continuous line sinks along the other wall to describe a cold plate.

1.3 Turbulent-Laminar patterns in Poiseuille-Couette flow

Turbulence transition in wall-bounded shear flows has long been an interesting and challenging research field. Three classis wall-bounded shear flows are plane Couette, plane Poiseuille, and pipe flow. Normally transition flows contain turbulent regions coexist with laminar regions. There exist, however, a particular regime in which

alternating turbulent and laminar bands coexist and are aligned next to each other. Prigent et al. (45, 46) discovered the existent of regular turbulent-laminar patterns in counter-rotating Taylor-Couette flow. It is worth noticed that observation of more irregular versions was made earlier by several researchers (47-51). Regular turbulent-laminar banded patterns were also observed in experiments on plane Couete flow (45, 46), and also in numerous simulations of plane Couette flow (52-54), of plane Poiseuille flow (55) and of counter-rotating Taylor-Couette flow (56-58).

The turbulent-laminar patters observed above, especially in plane Couette flow, could be defined as essentially steady, spatially periodic pattern of distinct regions of turbulent and laminar flow emerges spontaneously from uniform turbulence near transition to laminar state. Their most striking features are the large wavelength and the oblique angle they form to the streamwise direction, as seen in Figure 1.2 in which simulation of plane Couette flow at transitional regime revealed the existence of such patterns.

Barkley and Tuckerman (52-54) have performed several numerical simulations of plane Couette flow at different Reynolds numbers. They show timeseries of spanwise velocity at 32 equally spaced points in the z direction as the Reynolds number is lowered in discrete steps, as plotted in Figure **1**.**3**. The authors defined four turbulent patterned regimes, which are called uniform, intermittent, periodic, and localized. In the uniform regime, turbulence extends across the entire domain, while in the intermittent regime, laminar patches randomly appear and disappear. Laminar and turbulent regions are found to be permanent and coexist in the periodic regime, while only a single turbulent region is surrounded by laminar flow in the localized regime. In this last

regime, the turbulent region is localized in space and the laminar region is actually described by the linear plane Couette profile.

While several studies of turbulent-laminar patterns have been carried out in plane Couette flow and counter-rotating Taylor-Couette flow, little effort has been put in studying this type of patterns in Poiseuille flow. Recent direct numerical simulation study of Tsukahara (55) has revealed existence of turbulent – laminar patterns in Poiseuille flow at low Reynolds number (Re = 1400), as seen in Figure **1.4**. The author also observed that these structures were equilibrium and self-sustained. Moreover, both the turbulent and laminar bands propagate with the streamwise velocity same with the bulk velocity and are inclined at an angle of 24^{o} with respect to the streamwise direction.

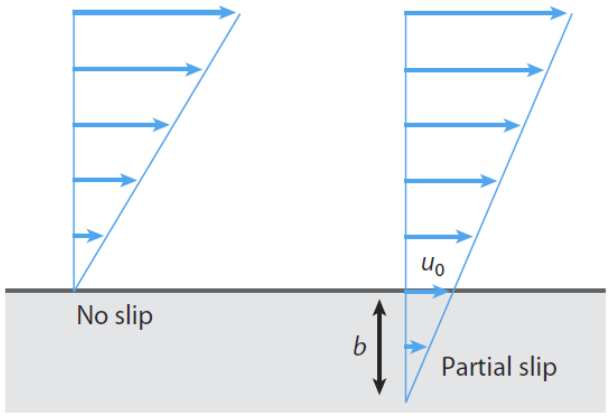


Figure 1.1 Schematic diagram of slip at a fluid-solid interface

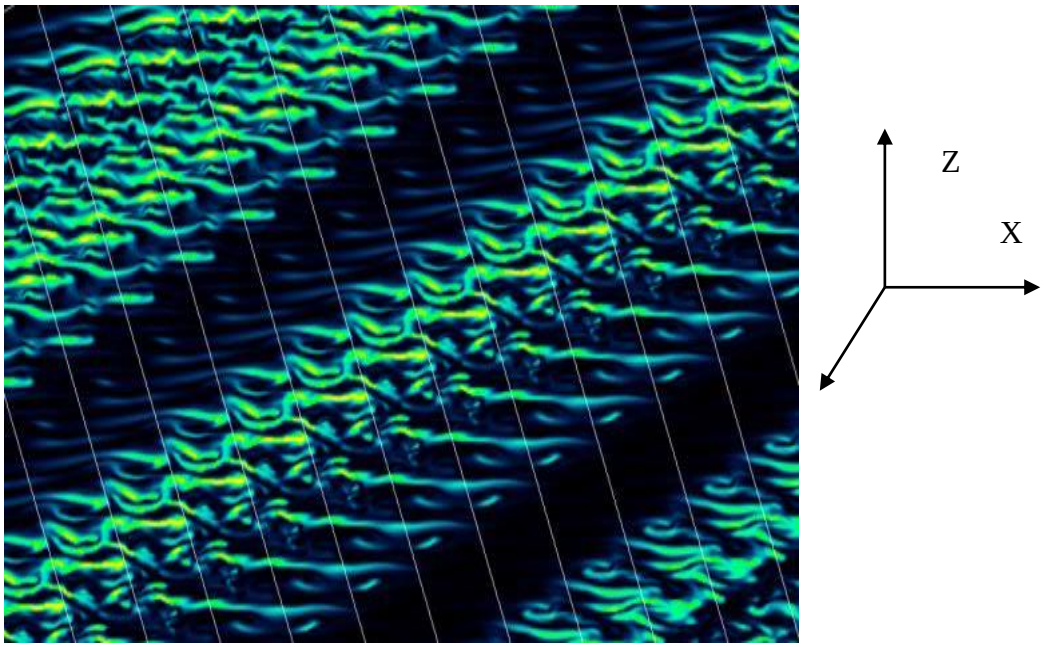


Figure 1.2 Computed turbulent-laminar pattern at Re = 350 in plane Couette flow by Tuckerman & Barkley (52). Above is the kinetic energy at y = 0, midway between bounding plates at y = ± 1 which move to the right and left in the streamwise direction. Turbulent bands consist of streamwise streaks and vortices. The bands are oriented in the direction denoted by x at an angle of 24^{o} from the streamwise direction, and are separated by a wavelength of 40 in the direction of the pattern wavevector, denoted by z.

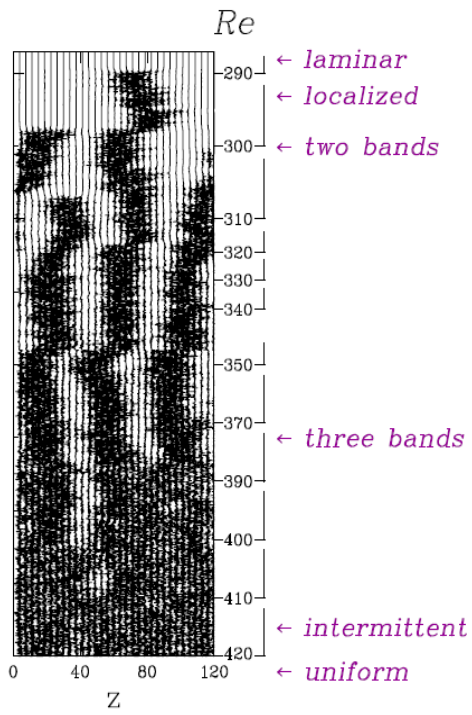


Figure 1.3 Time series of spanwise velocity at 32 points along a line in the midplane x = y = 0 as the Reynolds number is decreased. Results are from a numerical study of plane Couette flow by Tuckerman & Barkley (54)

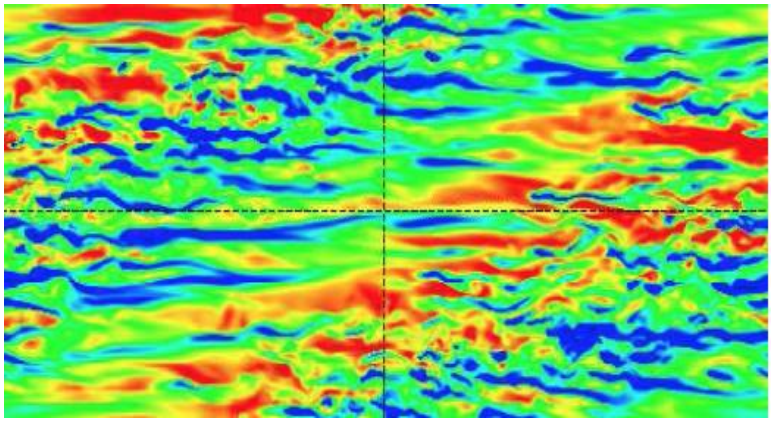


Figure 1.4 Turbulent-laminar patterns observed in a direct numerical simulation of plane Poiseuille flow by Tsukahara (55). Contour of streamwise fluctuating velocity in an (x,z) – plane at $y/\delta \approx 0.5$ for $Re_\tau = 80$. The direction of the mean flow is from left to right.

Chapter 2. Numerical Methodology

2.1 Direct Numerical Simulation (DNS)

The Direct Numerical Simulation (DNS) technique is used to solve numerically the Navier-Stokes equation by resolving the different spatial and temporal scales existing in a turbulent flow (59-62). Lyons et al. (63) used a pseudospectral algorithm to determine the turbulent velocity field and the results obtained have been validated with experiments by Gunther et al. (64). In this algorithm, the rotational form of the Navier-Stokes equation was first made dimensionless by using the wall variables, i.e., the kinematic viscosity, v, and the friction velocity, $u^* = (\tau_w/\rho)^{1/2}$. The rest of the variables, like the length, time etc, were expressed in terms of these wall variables, and hence these quantities were scaled with the so-called viscous wall units. Another interesting case considered here was the plane Couette flow, where the walls of the channel move relative to each other. The algorithm of Lyons et al. was suitably modified to account for the wall behavior (65, 66). The fluid in both cases was considered to be an incompressible Newtonian fluid with constant density, constant viscosity and constant thermal conductivity. The assumption that the viscous heating effects and the body forces are negligible was also made. The mean pressure gradient acted as the driving force for the Poiseuille channel flow, while the motion of the channel walls in opposite directions (which generates a region of constant shear stress) acted as the driving force for flow in plane Couette flow. The streamwise component of the velocity vector at the channel walls, which was set to zero in Poiseuille flow due to stationary walls, is non-zero for the case of plane Couette flow. The bottom wall moved in the negative x

direction, while the top wall moved in the positive *x* direction. The Figure 2.1and Figure 2.2 depict the picture of turbulent Poiseuille and plane Coeutte flow, respectively. The general description of the DNS is universal to all the studies in this dissertation. Some of the specific details of each study will be described briefly in the corresponding Chapter.

2.2 Lagrangian Scalar Tracking (LST)

The method of stochastic tracking of heat or mass markers in a turbulent flow field, and the statistical post-processing of the results to obtain scalar profiles is termed as Lagrangian scalar tracking (LST). The passive scalar markers released into the flow field are assumed to be point markers with no size and mass. There are no interactions between the markers. Hence, the trajectory of a marker does not affect the trajectories of other markers, and it does not affect the flow, an assumption that is realistic for dilute solutions. Therefore, "passive scalar transport" is simulated. A Direct Numerical Simulation in conjunction with the tracking of scalar markers, LST, has been used in our laboratory to study scalar transfer based on direct calculations of the behavior of such sources (65, 67-70). The tracking algorithm of Kontomaris et al. (71) is used to track individual trajectories of these markers in space and time in a Lagrangian framework, in conjunction with the DNS. The combined DNS/LST approach has been previously used to study heat transfer in high Prandtl or Schmidt number fluids (72, 73). Discussion about the accuracy of this method and comparisons of the results with experimental findings can also be found in previous publications (67, 74-76). Mass markers are released into the flow field after the velocity field reaches steady, fully

developed state. If $\vec{V}(\overrightarrow{x_0}, t)$ is the Lagrangian velocity of a particle that was at location $\overrightarrow{x_0}$ at time $t = t_0 = 0$, then the position $\vec{X}(\overrightarrow{x_0}, t)$ of the marker at time t is calculated based on the equation

$$\vec{V}(\vec{x}_0, t) = \frac{\partial \vec{X}(\vec{x}_0, t)}{\partial t} \tag{2.1}$$

At this point we make a basic assumption that a marker at any time has the velocity of the fluid particle on which it rides, which means that the relation between the Lagrangian velocity and the Eulerian velocity $\vec{U}$ is $\vec{V}(\vec{x}_0, t) = \vec{U}[\vec{X}(\vec{x}_0, t), t]$. Since the mass markers can move off a fluid particle due to molecular diffusion, the diffusion effect has been represented by adding a random walk on the marker motion after each simulation time step. The value of the diffusion step is estimated by a Gaussian distribution in each space direction with a zero mean and a standard deviation, σ, depending on the Schmidt number, *Sc*, ($\sigma = \sqrt{2\Delta t^+ / Sc}$) where Δt^+ is the time step of the simulation.

Besides the common error due to discretization, the numerical error with the LST methodology can be caused by the number of markers considered. Papavassiliou and Hanratty (67) and Papavassiliou (74, 75) have addressed this issue by examining the statistics of marker trajectories with databases of 16,129 markers and repeating the calculations with the half the number of markers. They have found that results of acceptable accuracy can be obtained with half the number of markers. Mitrovic (77) had further the investigation with a set of 16,129 markers and a set of almost one order of magnitude larger, 145,161 markers. The study showed that the average difference in the statistical behavior of runs with the same Sc and different number of markers is less

than 1.5%. The study stated that the use of samples with an order of 10^4 markers can provide accurate results for the generation of first order statistics. A balance between the computational cost that is associated with the creating of large data sets and acceptable accuracy of the results should be considered when employing the LST methodology. In each study, different Sc's and different number of scalar markers are released. Also, the orientation of the release is unique to the different studies. Hence, a brief description of the flow and marker parameters, specific to the particular study, has been provided in the corresponding Chapters.

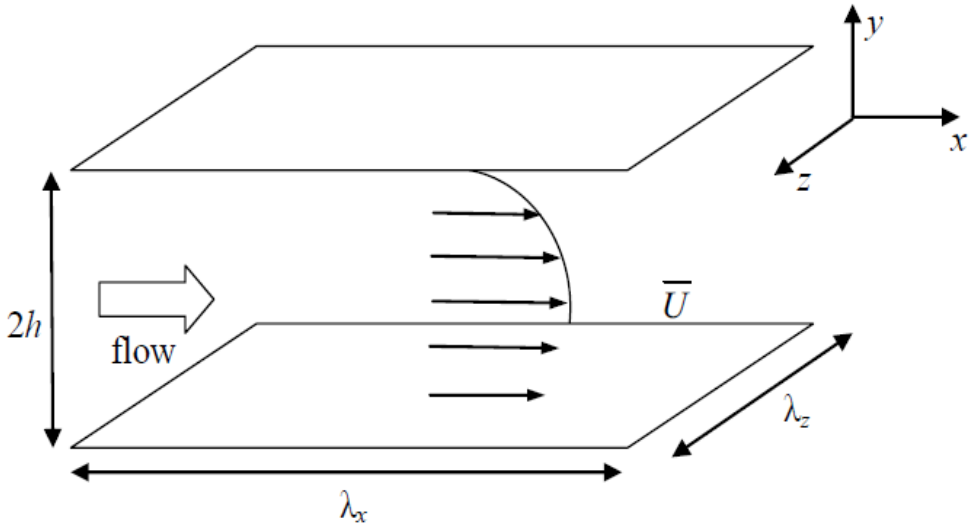


Figure 2.1 Plane Poiseuille flow configuration

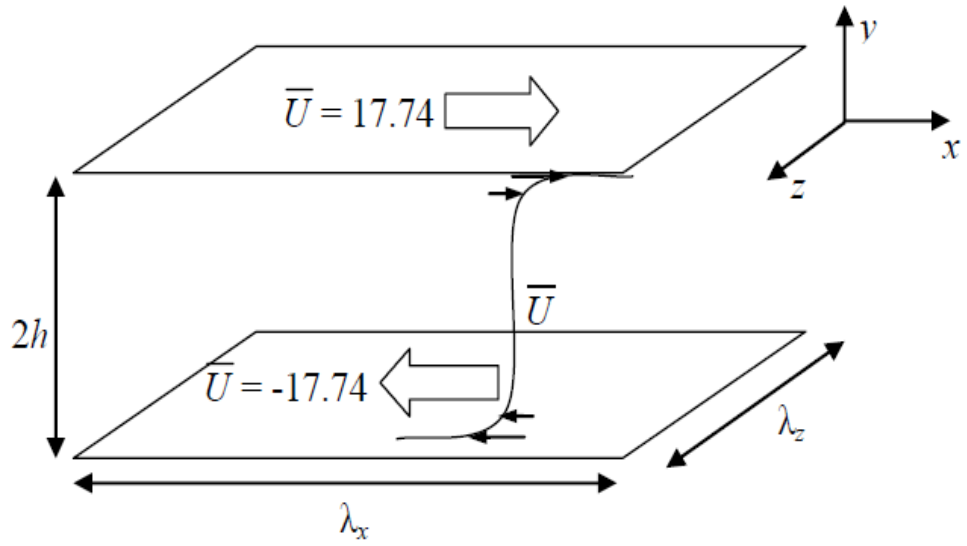


Figure 2.2 Plane Couette flow configuration

Chapter 3. Turbulent plane Poiseuille-Couette flow as a model for fluid slip over Superhydrophobic Surfaces

3.1 Simulation Parameters and Procedure

In this study, we performed direct numerical simulation of a turbulent plane Poiseuille-Couette flow as a model for fluid slip over superhydrophobic surfaces. The flow was simulated in a computational box of size $8\pi h$ x $2h$ x $2\pi h$ in x, y and z directions, respectively (h is half of the channel-height and is equal to 300, made dimensionless with the viscous length scale that is based on the kinematic viscosity of the fluid and the friction velocity, $u_\tau = \sqrt{\frac{\tau_w}{\rho}}$, where τ_w is the shear stress at the wall and ρ is the density of the fluid). The flow was assumed to be periodic in the streamwise, x, and spanwise, z, directions with lengths of periodicity equal to the box size in those two directions. Flow of an incompressible and Newtonian fluid was simulated at Reynolds number of 5,700, based on half of the channel height and the mean centerline velocity. The computational box had a resolution of 512 x 129 x 256 in x, y, z directions (the resolution in Kolmogorov length scales increased from 0.06 next to the wall to 1.71 at the channel center). A uniform mesh was used in x and z, while a non-uniform mesh based on Chebyshev collocation points was used in the y direction (63). The time step in dimensionless viscous units was 0.15.

In this simulation, the Navier-Stokes equations were resolved and integrated in time by using a pseudo-spectral fractional step method mentioned above (63). This algorithm has been validated in simulating plane Poiseuille flow and plane Couette flow

through comparisons with laboratory measurements and other DNS results at similar conditions (63, 64, 66).

In order to model a channel wall with specified slip, Poiseuille-Couette flow was simulated as a model of controlled slip boundary conditions applied on the channel walls. In this type of flow, along with a constant pressure gradient, the top wall of the channel was set to move in the positive streamwise direction (flow direction), while the bottom wall moved with an equal velocity but in the opposite direction. Relative velocities between the two channel walls were equal to 1, 2 and 4 viscous wall units. Based on the Galilean invariance of the Navier-Stokes equations, by subtracting the velocity at the bottom wall from the channel velocity field, one obtains the velocity field for the case in which the bottom wall is stationary and the top wall moves in the positive x-direction with velocity equal to the relative velocity between the two walls. This approach corresponds to a fixed slip velocity in the streamwise direction applied as a boundary condition at the top wall, and represents the use of a superhydrophobic surface as the top wall. The mean shear rate at the wall is then determined by the numerical solution of the flow equations. The application of different slip velocities at the top wall is equivalent to choosing different surfaces with a different degree of superhydrophobicity, for example when the spacing between the microscale ridges etched on the wall changes.

The numerical procedure used was similar to that followed in Spencer *et al.* (39) for a Reynolds number half of what is presented herein. The first run of the Poiseuille-Couette flow was initiated using a turbulent velocity field obtained from a fully developed, stationary-state Poiseuille flow simulation. The stationary state of the flow

was determined by comparing second order statistics, Reynolds stress and turbulent kinetic energy production averaged over a period of 2,000 viscous time units. Each simulation was run for 4,000 viscous time units to obtain stationary state, and then for another 4,000 time units to obtain enough data for analysis. Each simulation was used as the initial condition for the next simulation at higher relative wall velocity. The turbulence statistics presented from now on are averages over 4,200 dimensionless time units.

3.2 Results and discussion

3.2.1 Turbulent flow statistics

Data obtained by the simulations were analyzed in detail. The flow was characterized by the calculation of standard statistical quantities, like the turbulence intensities and the production of turbulence kinetic energy, and the differences from case to case were documented and presented in this section. Our results point out that shear stress at the moving wall is reduced, while it increases at the stationary wall, when compared to ordinary Poiseuille flow. All the results are then normalized with the friction velocity at the bottom (stationary) wall. Such normalization with the largest friction stress has been adopted in prior works (37-39, 78, 79). In their analysis of experimental data for flow through a channel with walls of different roughness, Hanjalic & Launder (78) scaled intensities by the wall friction velocity at the roughened wall. The shear stress was higher close to that wall than close to the smooth wall. Kuroda & Kasagi (79) also normalized their computational results by the shear stress at the stationary wall for plane Poiseuille-Couette flow.

The mean velocity profile for the case of Poiseuille flow, which employs zero slip as the boundary condition, in the half channel height is plotted in Figure 3.1 and is compared with other published data. In the viscous sublayer, the law of the wall $U^+ = y^+$ is clearly observed, while a logarithmic relation $U^+ = 2.6\ln y^+ + 4.5$ is shown in the log-law region (note that a superscript + is used to denote dimensionless variables, and U^+ is the mean streamwise velocity). This relation is comparable to the relation $U^+ = 2.5\ln y^+ + 5.5$ presented by Kim *et al.* (59) for a lower Reynolds number. One can see that our data match pretty well with the previous work of Gunther *et al.* (64), and with results of Nakabayashi *et al.* (37) for y^+ from 10 to 140 (note that Re_τ is the friction Reynolds number, and is defined based on the friction velocity and half of the channel height in viscous wall units).

In Figure 3.2 we plot the mean velocity profile in the channel with slip boundary condition at the top wall. This wall is at $y^+/d^+ = 0$, with d^+ being the channel height ($d^+ = 2h^+$), and U_s^+ is the slip velocity applied at the top wall. One sees that the use of a slip boundary condition at the top wall has little to no effect on the velocity profile close to the bottom wall. However, close to the top wall, the mean velocity is increased with the peak location shifted towards the moving wall. This trend was also observed in the work of Kuroda & Kasagi (79), as is also shown in Fig. 2. Note that the peak velocity in the data of Kuroda & Kasagi is pretty close to the moving wall due to extremely high wall velocity (12.2 in viscous wall units) used in that work (corresponding to a high value of γ, which is defined as the ratio of the Couette over the Poiseuille Reynolds number as introduced in (38): $\gamma = \frac{U_s^+}{U_{centerline}^+}$).

Figure 3.3 is a presentation of the Reynolds stress profile in the channel (u^+ and v^+ stand for the fluctuating velocities in the streamwise and vertical directions, respectively). A decrease in the maximum values of the Reynolds stress close to the moving wall is seen as the slip velocity is increased. This decrease of Reynolds stress has also been observed in previous studies (39, 80). Due to the decrease of shear stress at the top wall, one would expect a change in the *y*-position at which the total stress and the Reynolds stress become zero. Indeed, the shift in the location of zero stress is clearly observed in the figure. In the case of no wall movement, good agreement between our data and those of Thurlow & Klewicki (38) and Gunther *et al.* (64) is observed and presented. Note that Reynolds stress values of Thurlow & Klewicki are lower than our data due to their lower Poiseuille flow Reynolds number (7,500) compared to ours (11,400).

The root mean squared (rms) of the turbulent velocity fluctuations in all three directions is plotted in Figure 3.4. It should be noticed that in all cases the maximum rms of the velocity fluctuations in the region close to the moving wall decreases significantly, especially in the normal and spanwise directions. This indicates that the effect of slip velocity at the wall is to decrease turbulent intensity. One can find similar trends in Min & Kim (31) and Spencer *et al.* (39). On the other wall, turbulence intensities in the normal and spanwise directions increase slightly, when U_s^+ increases. Such behavior can be explained as a result of the increasing Couette character of the flow as U_s^+ increases, since Couette flow produces higher turbulence intensity compared to Poiseuille flow, mostly in the *y* and *z* directions (39, 66).

The effect of the moving wall on the production of the turbulent kinetic energy (TKE), defined as $\overline{(uv)}^{+}\mathrm{d}U^{+}/\mathrm{d}y^{+}$, is clearly observed in Figure 3.5. Close to the moving wall, the maximum production is significantly decreased to about half of its original value, as the slip velocity increases to 4. The location at which this maximum production occurs remains unchanged, when it is scaled with the channel height. This location, however, would be shifted away from the wall when scaled with the friction velocity at the stationary wall (*i.e.*, it is shifted from 10.9 wall units in Poiseuille flow to 14.0 wall units away from the moving wall for U_s^+ = 4). This trend has also been reported in a previous drag reduction study with polymer solution (81).

With the increase of the mean velocity in the channel and the decrease of Reynolds stress, turbulence intensities and turbulent kinetic energy production, it is reasonable to expect that drag reduction is present. Drag reduction is defined as

$$DR = 1 - \frac{\tau_w}{\tau_{wo}} \qquad (3.1)$$

where the stress at the wall for Poiseuille flow with the same pressure drop as the Poiseuille-Couette flow is designated as τ_{wo}. In this work, data are normalized with the shear stress at the bottom wall. As a result, the shear stress at the top wall is -1.000, -0.924, -0.859, and -0.734 for U_s^+ = 0, 1, 2, and 4, respectively. The shear stress at the bottom wall, after normalization, is 1 in all cases.

Values of drag reduction are plotted in Figure 3.6. These values are compared with results from the relationship of Fukagata *et al.*(82), who suggested that the following equation relates the slip length with drag reduction

$$l_x^+ = \frac{1-u_\tau^+}{(u_\tau^+)^2}\left(\frac{1}{\kappa} lnRe_{\tau 0} + F\right) - \frac{1}{\kappa u_\tau^+} lnu_\tau^+ \qquad (3.2)$$

with $\kappa = 0.41; F = 3.2$. The superscript + indicates that scaling with the friction velocity and corresponding wall units at the stationary wall is applied, as noted previously. The data are in good qualitative agreement with the above prediction, and they are comparable to drag reduction results obtained with the use of a polymer solution (81).

3.2.2 Two-point velocity correlation coefficients

The picture that emerges up to now about the effects of the streamwise slip velocity on the turbulence is that the profiles of the mean velocity and the mean Reynolds stress are modified and their maximum and zero, respectively, are shifted in the case of Poiseuille-Couette flow. This finding is not new – it is in agreement with prior published work. At the same time, turbulence intensities are weaker as the slip velocity increases, leading to drag reduction. However, what does this mean for the near wall coherent structures, and what are the changes in the flow events that contribute to decreasing the mean Reynolds stress are the questions that need to be explored. The modification of the Eulerian length scales of the near wall structures can be quantified by examining the two-point correlation coefficients.

We define the two-point streamwise fluctuating velocity correlation coefficient with streamwise separation $Ru^+u^+(\delta)\,|x^+$ as

$$Ru^+u^+(\delta)|x^+ = \frac{<u^+(x^+=0)u^+(x^+=\delta)>}{<(u^+)^2(x^+=0)>} \qquad (3.3)$$

Note that the symbol <á n> indicates average over all the grid points in the *xz* plane. Similar definitions are applied for the two-point normal fluctuating velocity correlation coefficient with streamwise separation $Rv^+v^+(\delta)|x^+$. The streamwise and

normal fluctuating velocity correlation coefficients with spanwise separation, $Ru^+u^+(\delta)|z^+$ and $Rv^+v^+(\delta)|z^+$, respectively, are also defined in a similar manner.

Due to the assumption of periodicity in the streamwise and spanwise directions, and symmetry across the center-plane of the channel, one needs to plot only one-fourth of the Poiseuille channel. On the other hand, half of the channel needs to be shown for the cases with moving walls. Figure 3.7 is a plot of values of $Ru^+u^+(\delta)|x^+$ for the two cases that are mostly different (Poiseuille flow and $U_s^+ = 4$) in the *xy* plane. The correlation was calculated at the last reported time step in each simulation sequence. Note that due to normalizing with the shear stress at the bottom (stationary) wall, the values of the box size in *x, y,* and *z* in dimensionless units are multiplied by a factor larger than 1. In both cases, it is observed that the length scale associated with the correlation coefficient increases with the distance from the wall in the viscous sublayer. Moreover, the length scale increases with U_s^+. Specifically, the streamwise distance at which the two-point correlation coefficient reaches zero close to wall in Poiseuille flow is approximately 1350, but increases to around 1600 in the case of $U_s^+ = 4$. If we define a macroscopic length scale by using the zero contour line, at the vertical position close to the moving wall at which turbulent kinetic energy production reaches its maximum (see Figure 3.5), we find this scale to be 1365 for Poiseuille flow, but close to 1645 in case of $U_s^+ = 4$.

With spanwise separation, it is also found that the length scale increases with the distance from the wall, and the macroscopic length scale increases with U_s^+. The correlation coefficients with spanwise separation for the streamwise and normal fluctuating velocities are plotted in Figure 3.8 and Figure 3.9. Again, one should note

the changes in nondimensional values of the box size in *y* and *z* dimensions. In Figure 3.10 and Figure 3.11 an increase in the length scale in the spanwise direction can be seen, when using the zero contour lines that appear in Figure 3.8 and Figure 3.9 to define this length scale.

These findings for the correlation coefficient in *x* and *z* directions, along with the decrease of turbulent intensities, suggest that the near-wall eddies become longer in the streamwise direction, thicker in the spanwise direction, and also weaker close to the wall with the specified slip in the streamwise direction. Similar changes have been reported in Spencer *et al.*(39) for Poiseuille-Couette flow, who found an increase in the integral length scale in the streamwise direction. More importantly, similar changes have been observed in the case of turbulence drag reduction with the use of polymers. Housiadas & Beris (83) found wider eddies in the spanwise direction, and Stone *et al.*(80) observed larger length scales in the buffer layer. Due to these changes, eddies would be less effective in transferring momentum from the viscous sublayer to the outer region of the flow and vice versa.

3.2.3 Reynolds stress analysis by quadrants

Modifications of the mean Reynolds stress profile and a change in the distance from the wall at which the mean Reynolds stress crosses zero are expected, since there are changes in the mean viscous shear of a channel with a wall exhibiting streamwise slip. The ones among the Reynolds stress-generating coherent structures that are modified can be revealed with further analysis. In the previous section, it was documented that, in general, the near wall eddies tend to become longer and weaker. A

quadrant analysis of the Reynolds stresses can further differentiate whether this observation applies equally to all coherent structures, or whether a selective change in flow events occurs that affects in different ways the flow structures that are involved in the momentum exchange between the outer and the inner regions of the flow.

Four different Reynolds stress quadrants can be defined based on the sign of the streamwise and normal fluctuating velocities. Quadrants 1 and 3 contain x and y fluctuating velocities with the same sign (either both positive or both negative), while quadrants 2 and 4 have x and y fluctuating velocities with opposite signs (note that quadrant 2 has positive normal fluctuating velocities, while quadrant 4 contains negative ones). The relative contribution of each quadrant to the total Reynolds stress can be represented in terms of a fractional contribution, which is defined as

$$Quadrant\ i\ contribution\ = \frac{|Reynolds\ stress\ of\ Quadrant\ i|}{\sum_{i=1}^{4}|Reynolds\ stress\ of\ Quadrant\ i|} \tag{3.4}$$

The most significant changes in fractional contribution values occur in quadrants 1 and 3 and are plotted in Fig. 12. It is observed that in the region close to the top wall (wall with specified slip velocity), the contribution of quadrant 1 is decreased, while that of quadrant 3 clearly increases as the slip velocity increases. This finding could be represented in terms of the change of fluid movement relative to the wall, as illustrated in the inset sketches. The plane represents the top wall, and the decrease (or increase) of the size of an arrow implies the decrease (or increase) of fluid movement in the direction of the arrow. One sees that as the slip velocity at the top wall increases, the amount of fluid moving faster than the mean flow and moving toward the top wall (corresponding to fluid in quadrant 1) decreases, while the fluid that moves slower than the mean flow and moves away from the top wall (corresponding to fluid in quadrant 3)

increases. If we define sweep events as fluid structures moving faster than the mean flow and moving fluid towards the wall region, and ejection (or burst) events as those structures that move slower than the mean velocity and carry fluid away from the wall (Lombardi *et al.* (84)), then it is obvious that as the slip velocity gets higher, sweep events are weakened and ejections happen more often.

This indicates that not only the length scales close to the channel wall are modified (as discussed in the previous section), but also the exchange of momentum between the outer region of the flow and the inner region of the flow close to the wall with velocity slip is modulated relative to the no-slip case. There is a reduction of transport of momentum from the outer flow toward the wall.

3.2.4 Vorticity magnitude and kinetic energy dissipation rate

In this section we investigate the changes in the vorticity and the effects of the slip on the relative magnitude of the different components of the vorticity. Based on the previously described findings about weakened turbulence intensity and the weakening of the sweep events, it is expected that the fluctuating vorticity magnitude is reduced as well. The question that is posed is whether this expected vorticity magnitude reduction occurs because of disproportionate changes in one component of the vorticity.

Vorticity magnitude (W) of the fluctuating velocity is plotted in Figure 3.13. In all cases, the magnitude of vorticity at the region close to the moving wall decreases dramatically, while it remains almost unchanged at the other wall. The decrease is up to 30% in the case with $U_s^+ = 4$ compared to the Poiseuille flow case, as it drops from 0.38 to 0.27. This result is consistent with the decrease of Reynolds stress in the viscous

sublayer that we observed, since vortices in the flow direction generated at the wall are mostly responsible for creating the Reynolds stresses in the viscous wall layer (85). Studies of drag reduction with a polymer solution have also indicated a suppression of vortices (80, 81).

An analysis of different components of vorticity is conducted and presented in Figure 3.14, in which the root mean squared values of vorticity in the *x, y,* and *z* directions are presented. A significant decrease of vorticity magnitude in all three directions at the region close to the moving wall is observed.

From Figure **3.14**, one may see that the vorticity of the fluctuating velocity in the direction normal to the channel walls is relatively small compared to that in the streamwise and spanwise directions. In the near wall region, the *z*-vorticity dominates over the other two, while in the region far away from the wall, the vorticity in the streamwise direction is dominant. Further study reveals that the vertical location at which the mean square of fluctuating vorticity in the *x* and *z* directions are equal is shifted away from the wall when the slip velocity at the top wall increases, as shown in Figure 3.15. As the slip velocity at the wall is increased, the domination of the spanwise vorticity over the other two vorticity components expands farther into the center region of the channel. In other words, vortices in the streamwise direction are suppressed more than those in the spanwise direction.

Following the reduction of TKE production we may expect that the dissipation of the TKE would decrease as well. The dissipation rate could be expressed as

$$\varepsilon = \nu\overline{\left(\frac{\partial u_i}{\partial x_j} + \frac{\partial u_j}{\partial x_i}\right)\frac{\partial u_j}{\partial x_i}} = \nu\overline{\left(\frac{\partial u_i}{\partial x_j}\frac{\partial u_j}{\partial x_i} + \frac{\partial u_j}{\partial x_i}\frac{\partial u_j}{\partial x_i}\right)} \tag{3.5}$$

in which the first cross-multiplying term in the right hand side stands for the anisotropic dissipation rate, and the second represents the isotropic rate. Values of the dissipation rate, as a summation of both isotropic and anisotropic components, are presented in Figure **3.16**. Corresponding to the decrease of the vorticity magnitude at the region close to the moving wall, the dissipation rate also shows a dramatic drop in this region, while it remains almost the same close to the bottom wall.

3.2.5 Anisotropic turbulence and mechanism of drag reduction over superhydrophobic surfaces

The observations described up to now represent phenomenological differences between the turbulence close to a wall with streamwise slip and a wall with zero slip. In order to investigate the reason for these differences, the effects of wall movement on the anisotropy of turbulence are examined through the calculation of the invariants of the Reynolds stress anisotropy tensor within the Lumley triangle (86). It is convenient to define here the anisotropy tensor using the notation below:

$$a_{ij} = \frac{\overline{u_i u_j}}{q^2} - \frac{1}{3}\delta_{ij} \tag{3.6}$$

where subscripts i,j designate the direction of the velocity fluctuations and δ_{ij} is the Kronecker delta. The scalar invariants of the Reynolds stress anisotropy tensor are as follows (note that repeated indices imply summation):

$$II_a = a_{ij}a_{ji} \qquad III_a = a_{ij}a_{jk}a_{ki} \tag{3.7}$$

Figure **3.17** is a plot of the second and third scalar invariants within the Lumley triangle. The two curves in the triangle represent axisymmetric turbulence. Turbulence

strained by axisymmetric expansion corresponds to the right curve, while the left curve indicates turbulence strained by axisymmetric contraction. The straight line corresponds to two-component turbulence, which is observed in the near wall region. The two corner points, one at the right and one at the left hand side of the map, indicate the limiting states of turbulence that correspond to one-component turbulence and two-component isotropic turbulence, respectively. It is obvious that close to the wall moving in the *x* direction, the movement of the wall (corresponding to slip velocity) has forced turbulence in this region to tend toward the limiting state located at the right corner point of the triangle. In this limiting state, turbulence satisfies not only the two-component limit but also axisymmetry at large and small scales (87). In the opposite side, close to the other wall, one can observe turbulence moving away from this limiting state, but not significantly. This trend, opposite to the behavior close to the moving wall, is consistent with the trends that we found and discussed when examining the second order statistics, and may be explained due to the relative strength of the Couette effect discussed earlier.

This finding, that turbulence close to the moving wall tends towards the limiting one-component state and thus will satisfy both the two-component limit and axisymmetry at large and small scales (87), is further confirmed by comparison of streamwise turbulence intensity with turbulence intensity in the other two directions, as plotted in Figure **3.18**. It is obvious that the domination of streamwise intensity over the intensity in the other two directions is enhanced as the slip velocity increases. The *x* direction is therefore the axis of symmetry close to the wall, i.e., small scale turbulence is locally invariant to rotation around the *x* axis.

Since turbulence (at small scales) close to the wall is locally axisymmetric, then it must satisfy the following kinematic constraints imposed by local axisymmetry (88)

$$\overline{\left(\frac{\partial^n u}{\partial y^n}\right)^2} = \overline{\left(\frac{\partial^n u}{\partial z^n}\right)^2}$$

$$\overline{\left(\frac{\partial^n v}{\partial y^n}\right)^2} = \overline{\left(\frac{\partial^n w}{\partial z^n}\right)^2} \tag{3.8}$$

$$\overline{\left(\frac{\partial^n v}{\partial z^n}\right)^2} = \overline{\left(\frac{\partial^n w}{\partial y^n}\right)^2}$$

A Taylor series expansion of the instantaneous fluctuating velocity in the near-wall region ($y \rightarrow 0$, given that y is the direction normal to the wall) which satisfies the continuity equation $\frac{\partial u_i}{\partial x_i} = 0$ is (89)

$$u = a_1 y + a_2 y^2 + \cdots$$

$$v = \quad b_2 y^2 + \cdots$$

$$w = c_1 y + c_2 y^2 + \cdots$$

Jovanovic & Hillerbrand (87) have shown that by inserting the above series expansion into the kinematic constraints above, all coefficients a_i, b_i and c_i must vanish. This is equivalent to a significant suppression of small scale turbulence in the near-wall region, leading to laminarization and significant drag reduction.

The specification, therefore, of a streamwise slip has forced turbulence close to the wall to tend towards the one-component limit, leading to suppression of turbulence at small scales and drag reduction. This explanation is also supported by the drag reduction by polymers study of Dimitropoulos *et al.* (90), who showed the transition of wall turbulence towards the one-component limit as higher levels of drag reduction were obtained with a polymer solution, and of Tamano *et al.*(91)who observed a suppression of conventional turbulence near solid surfaces in a polymer solution.

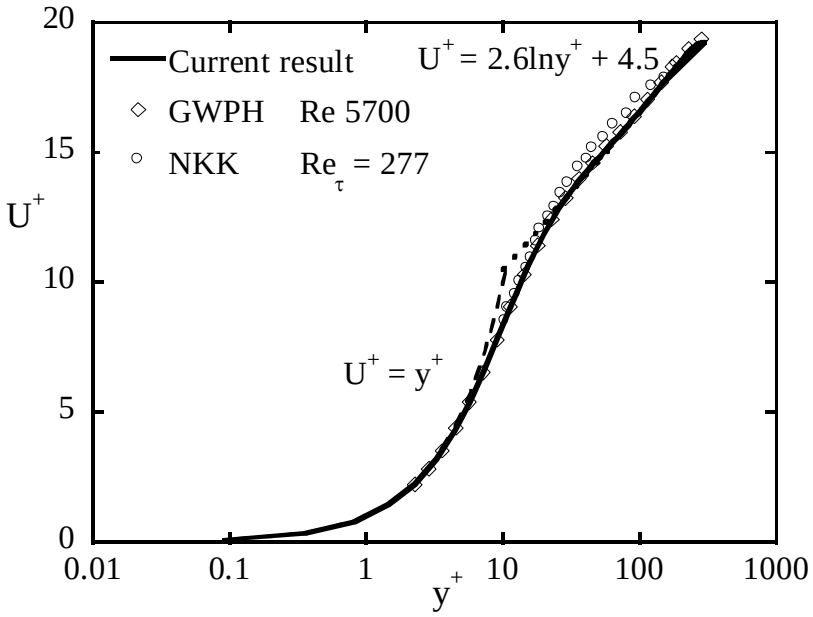


Figure 3.1 Mean streamwise velocity with no slip boundary condition (GWPH: data points from Gunther *et al.*(64); NKK: data points from Nakabayashi *et al.*(37), dashed lines: law of the wall)

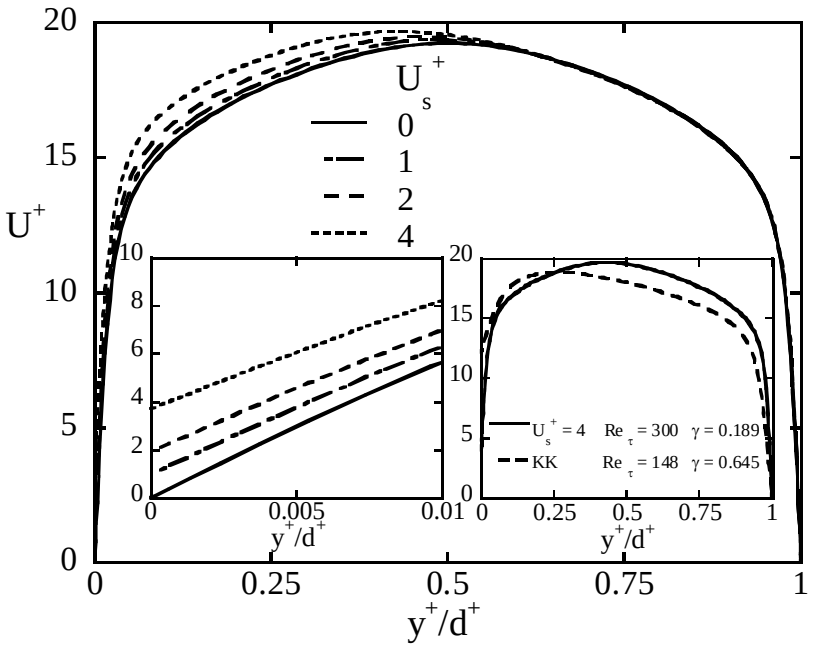


Figure 3.2 Mean velocity profile in Poiseuille and Poiseuille-Couette flow with U_s^+ = 1, 2 and 4 (KK: data from Kuroda & Kasagi (79)). The inset figure to the right includes results for different ratio of the Couette over the Poiseuille Reynolds number, denoted as γ ($\gamma = \frac{U_s^+}{U^+_{centerline}}$).

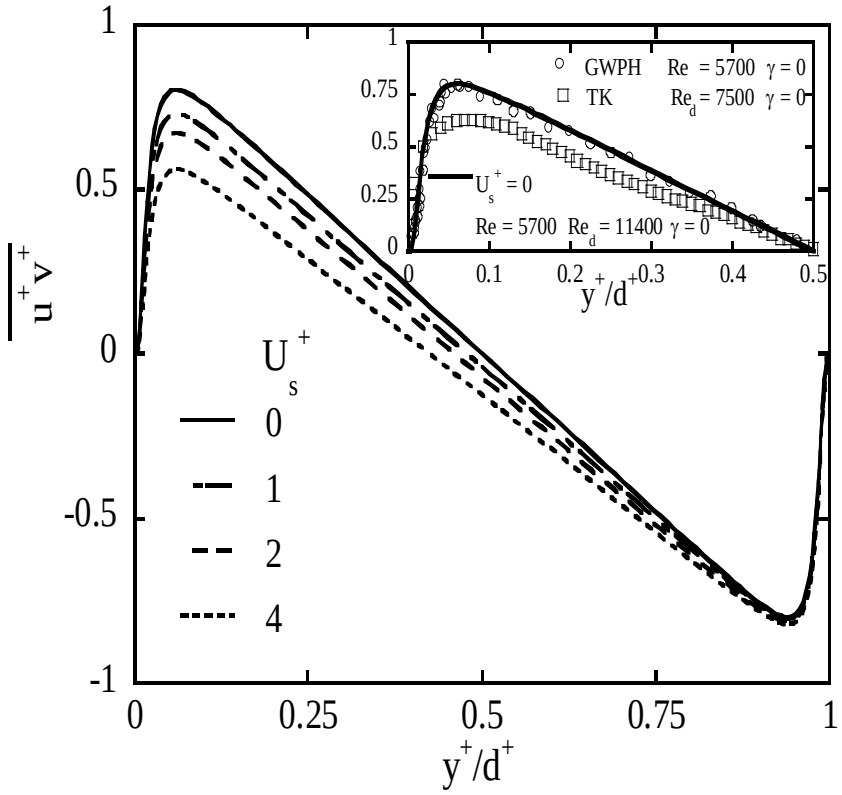
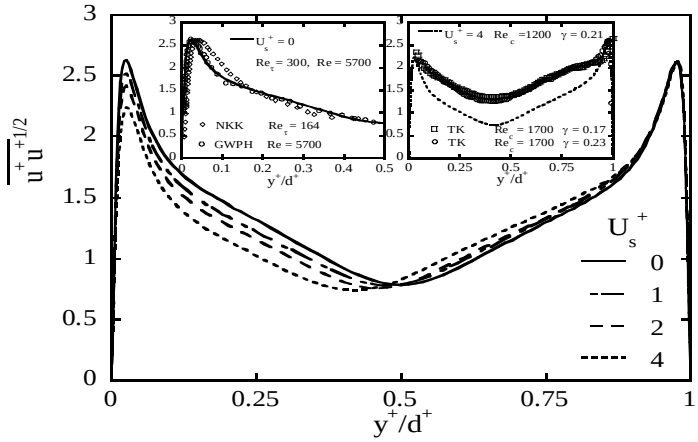
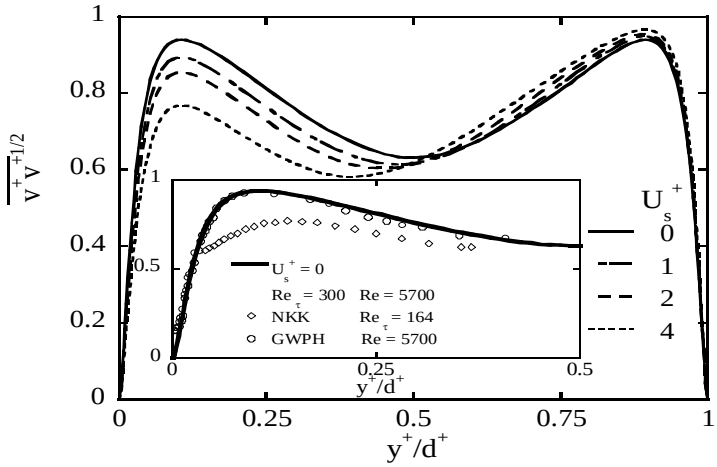


Figure 3.3 Reynolds stress profile in Poiseuille and in Poiseuille-Couette flow with U_s^+ = 1, 2, and 4 (GWPH: data points from Gunther *et al.* (64); TK: data points from Thurlow & Klewicki (38))

a)



b)



c)

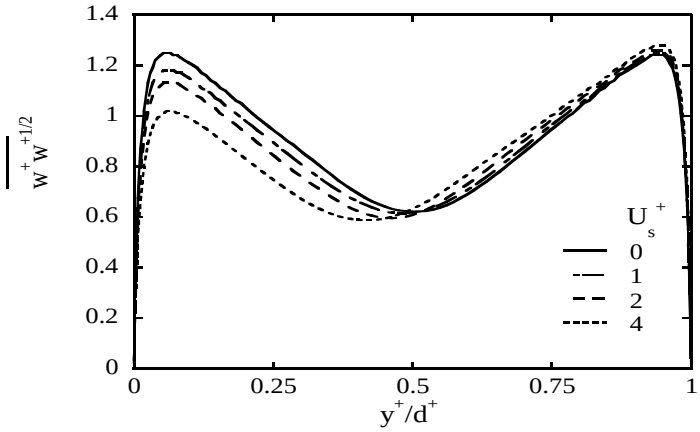


Figure 3.4 Root mean squared velocity fluctuations for the Poiseuille-Couette simulations: (a) Streamwise velocity; (b) Normal velocity; (c) Spanwise velocity (GWPH: data points from Gunther *et al.*(64); NKK: data points from Nakabayashi *et al.*(37); TK: data points from Thurlow & Klewicki (38)).

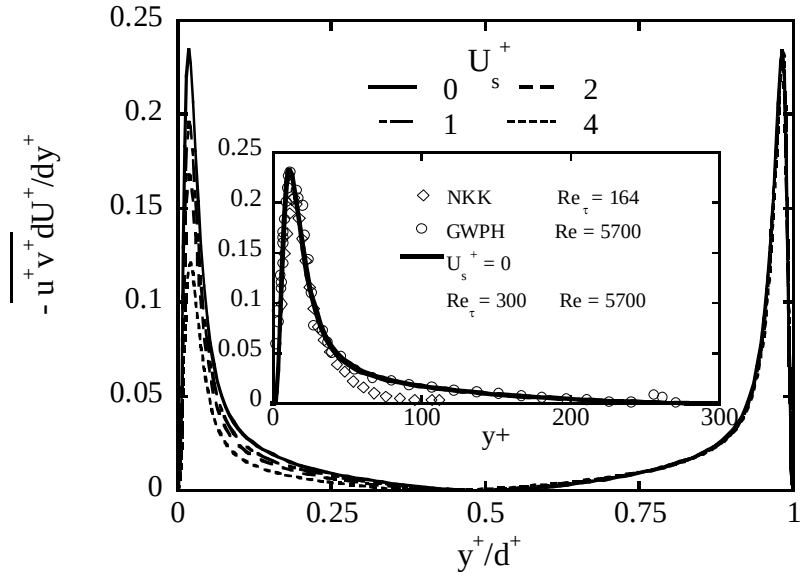


Figure 3.5 Turbulent kinetic energy production in Poiseuille and Poiseuille-Couette flow with U_s^+ = 1, 2 and 4 (GWPH: data points from Gunther *et al.*(64); NKK: data points from Nakabayashi *et al.*(37))

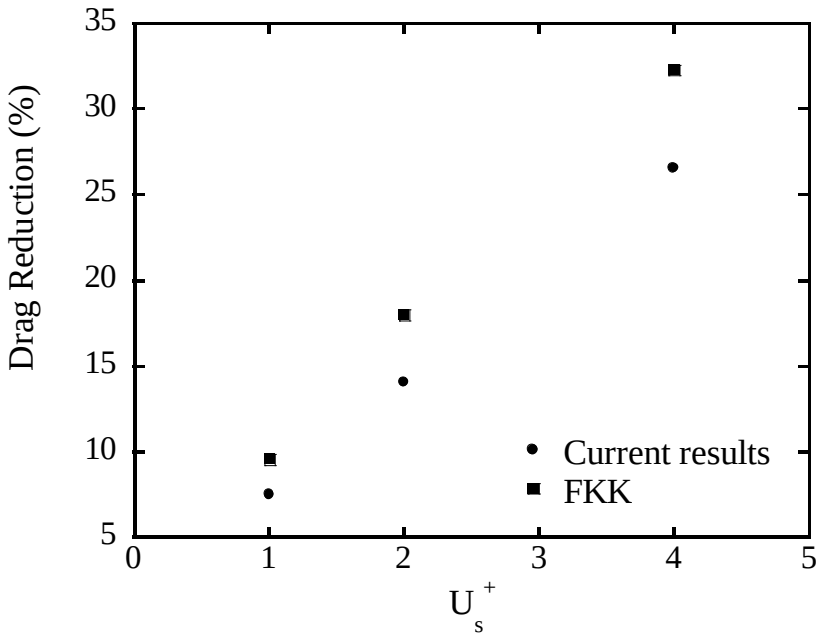
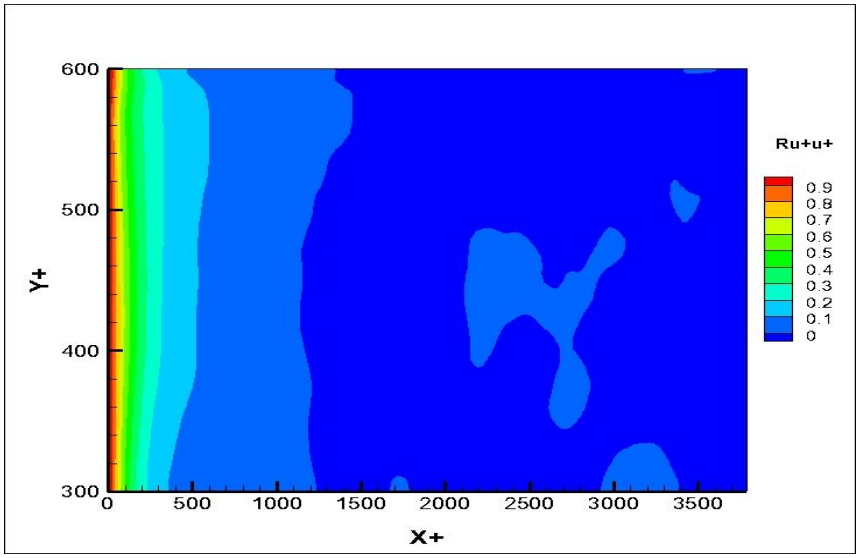


Figure 3.6 Drag reduction obtained in Poiseuille-Couette flow with different values of U_s^+ (FKK: theoretical prediction of Fukagata *et al*. (82))

a)



b)

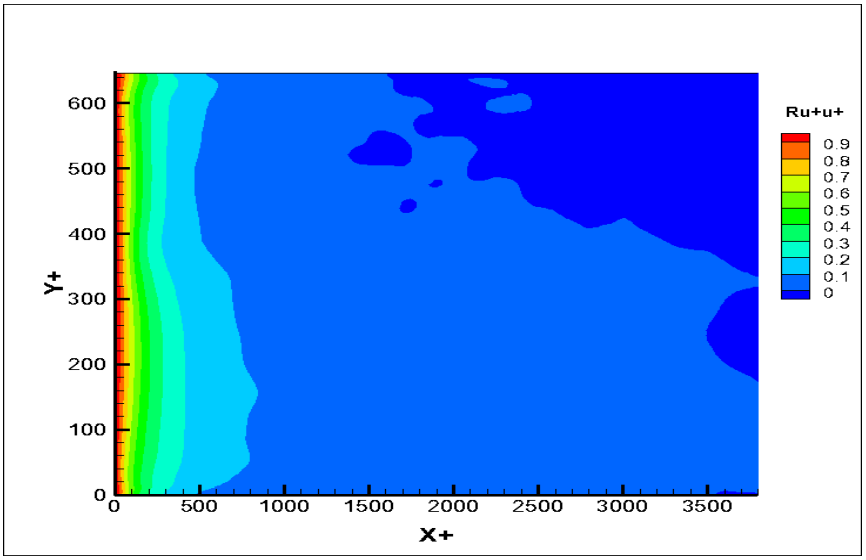
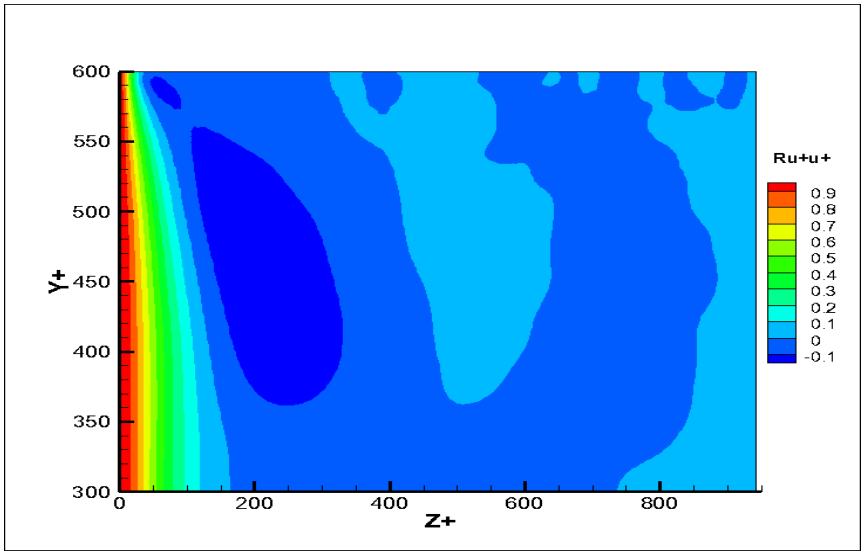


Figure 3.7 Two-point correlation coefficient with streamwise separation for the streamwise fluctuating velocity in (a) Poiseuille, and (b) Poiseuille-Couette flow with $U_s^+ = 4$

a)



b)

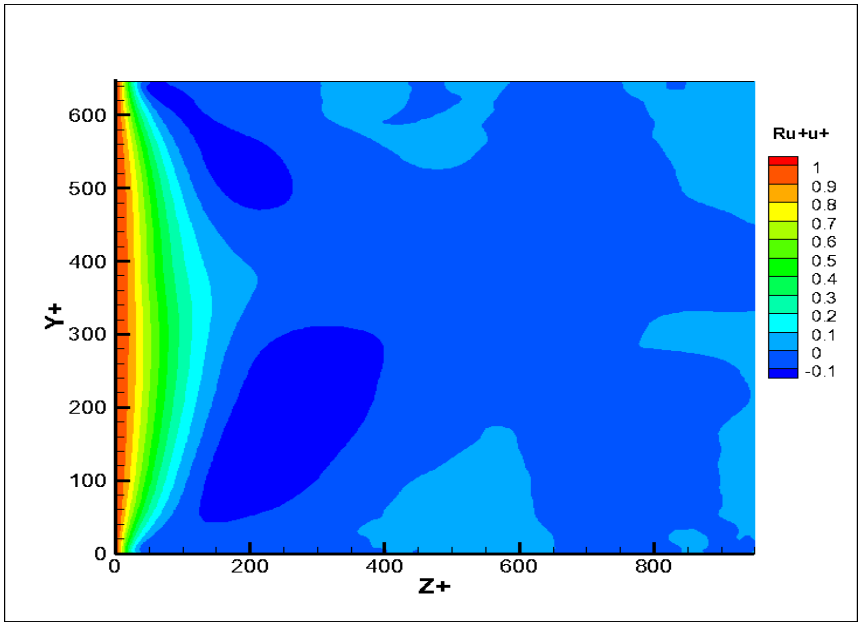
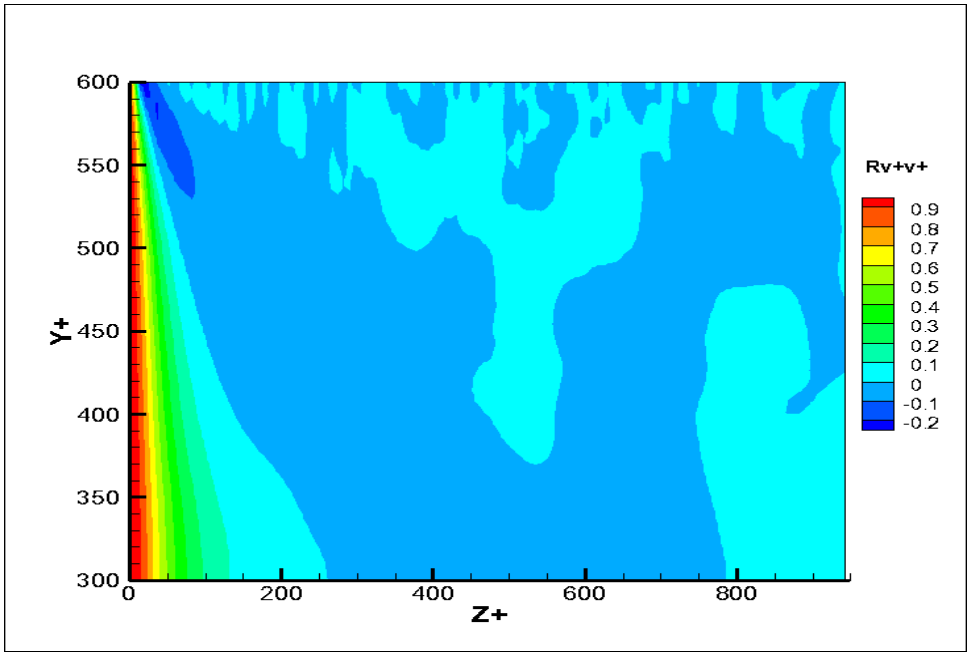


Figure 3.8 Two-point correlation coefficient with spanwise separation for the streamwise fluctuating velocity in (a) Poiseuille and (b) Poiseuille-Couette flow with $U_s^+ = 4$

a)



b)

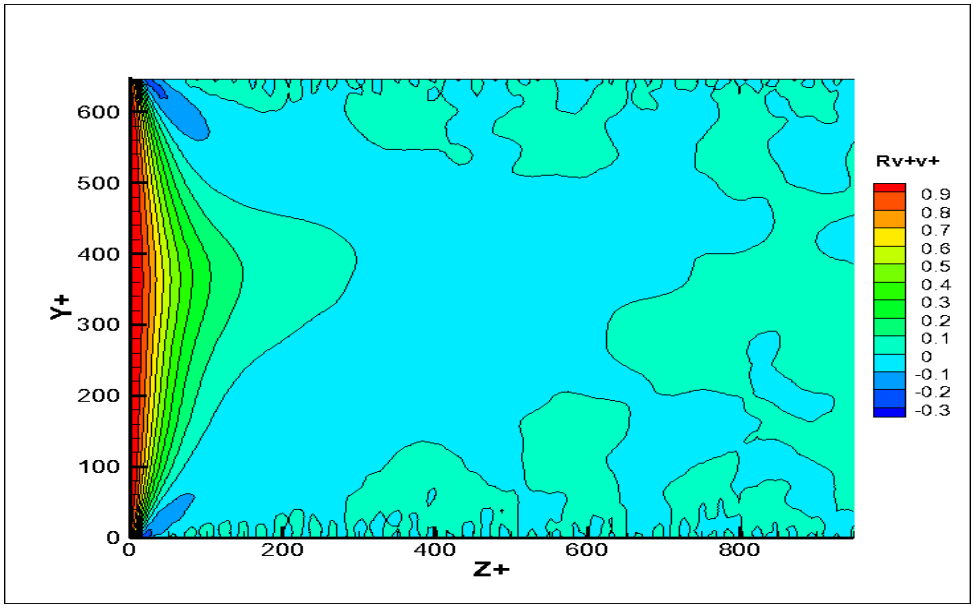


Figure 3.9 Two-point correlation coefficient with spanwise separation for the normal fluctuating velocity in (a) Poiseuille and (b) Poiseuille-Couette flow with Us+ = 4

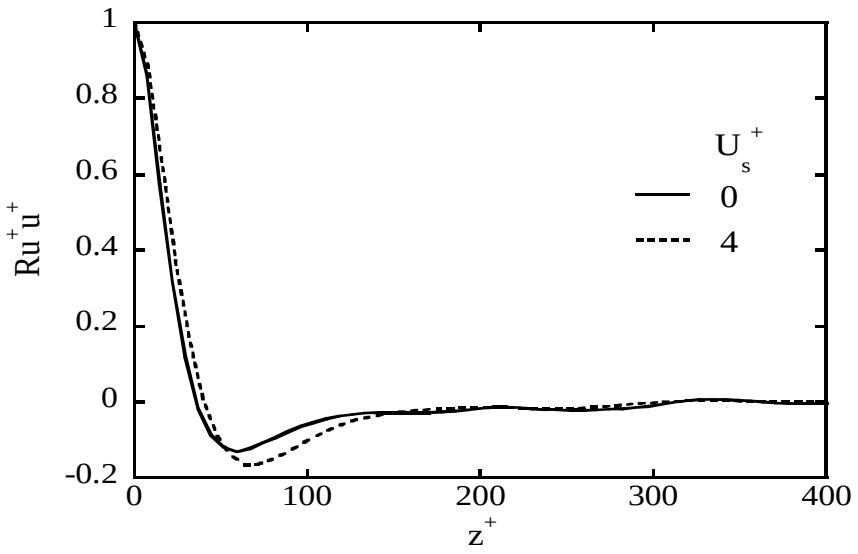


Figure 3.10 Two-point correlation coefficient with spanwise separation for the streamwise fluctuating velocity in Poiseuille and Poiseuille-Couette flow with Us+ = 4. This is calculated at the y-location of the maximum turbulent kinetic energy production. It is seen that there is an increase of the length scale in the spanwise direction, designated by the point of zero-crossing of the correlation coefficient.

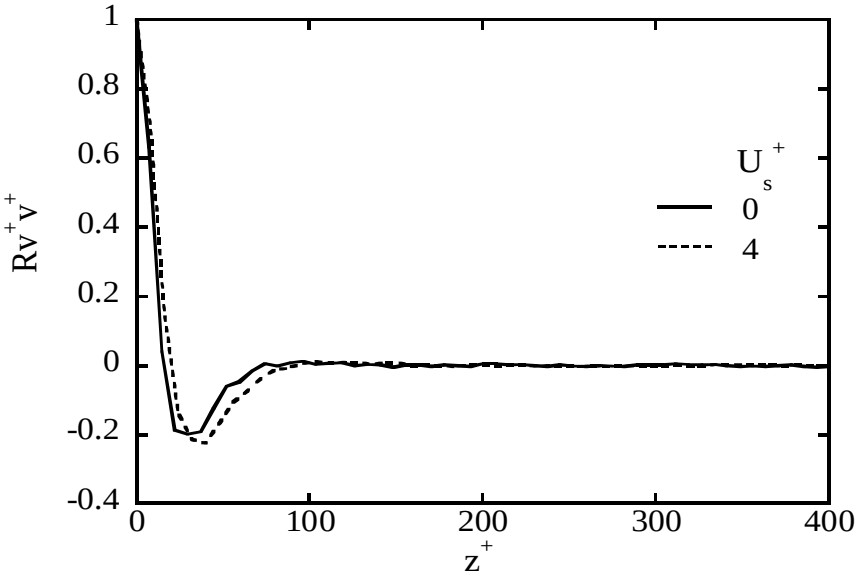
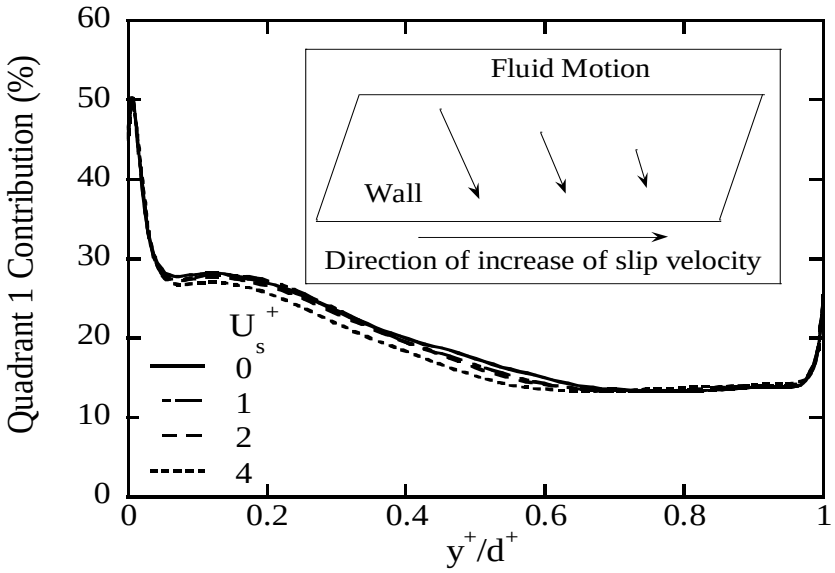


Figure 3.11 Two-point correlation coefficient with spanwise separation for the normal fluctuating velocity in Poiseuille and Poiseuille-Couette flow with $U_s^+ = 4$. This is calculated at the *y*-location of the maximum turbulent kinetic energy production. It is seen that there is an increase of the length scale in the spanwise direction, designated by the point of zero-crossing of the correlation coefficient.

a)



b)

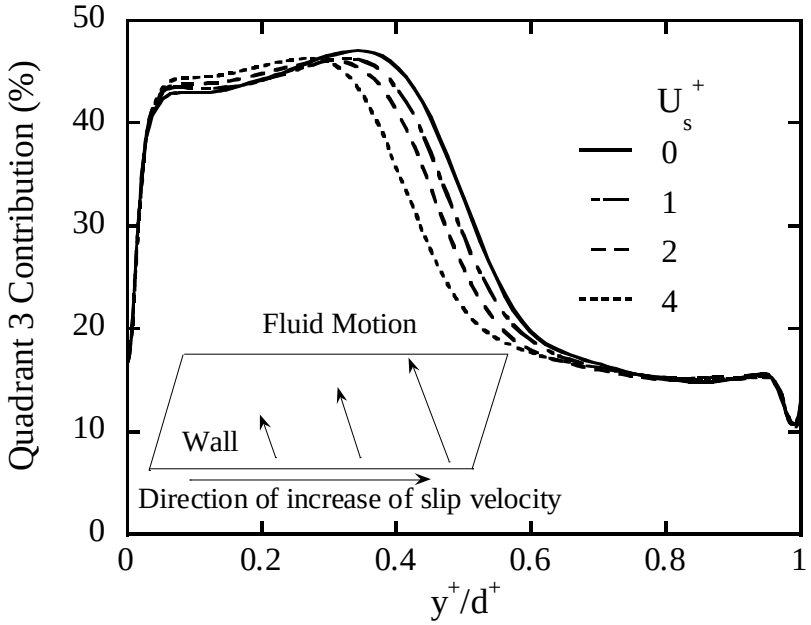


Figure 3.12. Fractional contribution of Reynolds stress of (a) quadrant 1 and (b) quadrant 3

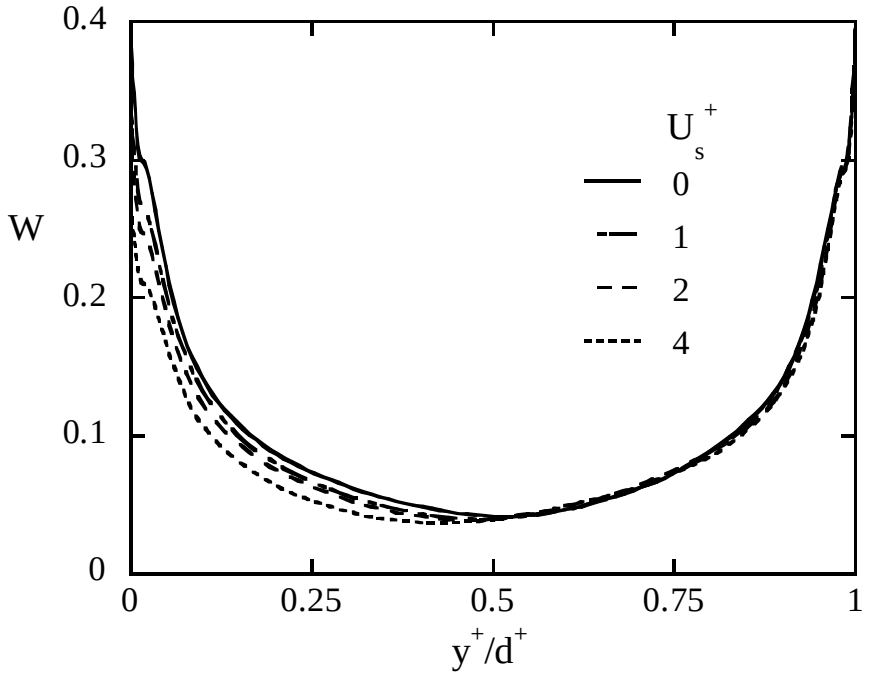
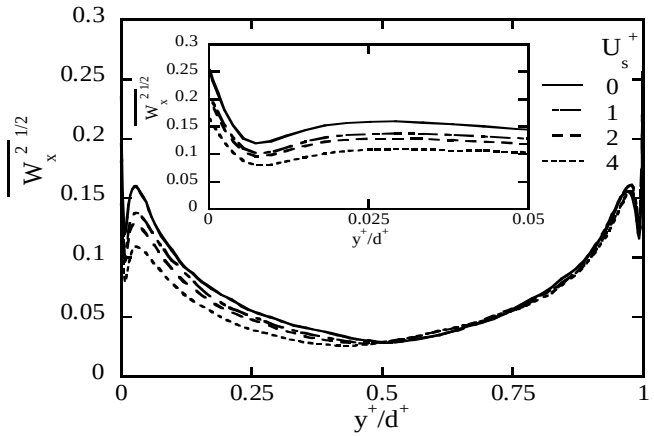
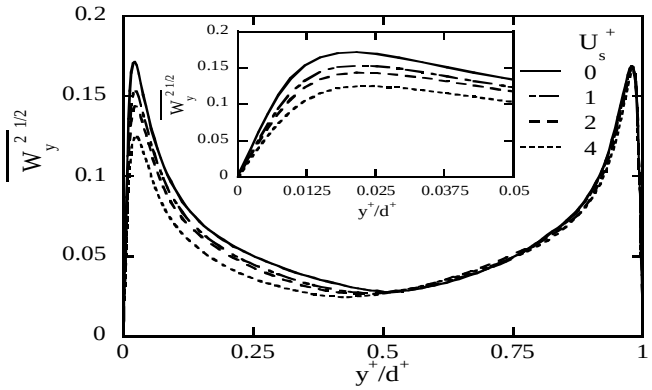


Figure 3.13. Vorticity magnitude in the Poiseuille and Poiseuille-Couette flow with $U_s^+ = 1$, 2, and 4

(a)



(b)



(c)

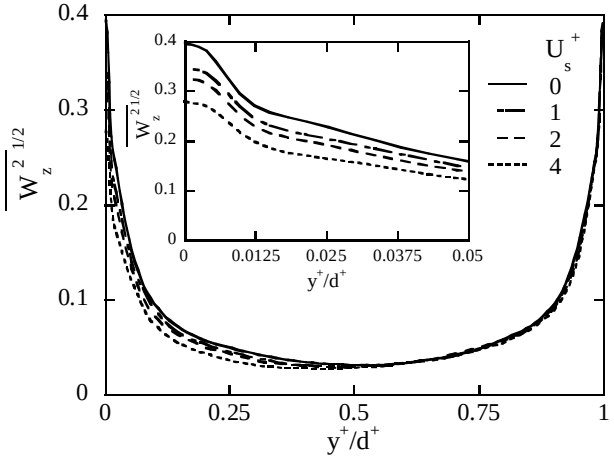


Figure 3.14. Root mean square of fluctuating vorticity in (a) x-direction, (b) y-direction, (c) z-direction in Poiseuille and Poiseuille-Couette flow with U_s^+ = 1, 2, and 4.

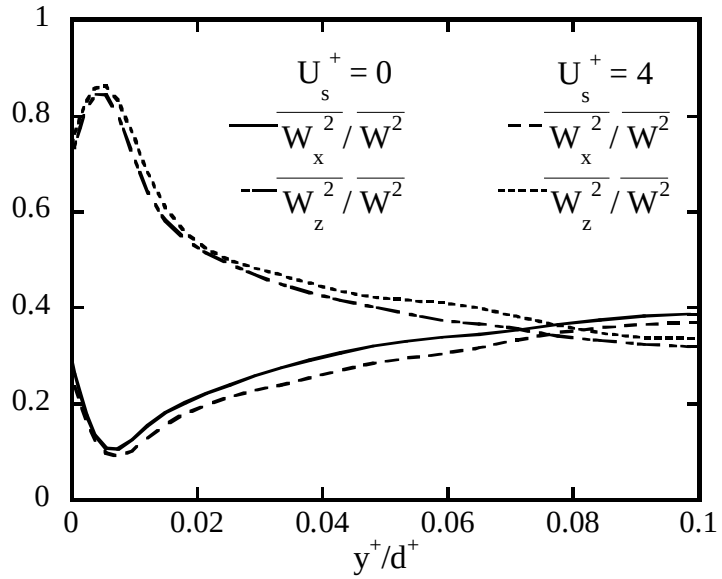


Figure 3.15. Ratio of the streamwise and spanwise fluctuating vorticity components over the total fluctuating vorticity. ($\overline{W_x^2}$ and $\overline{W_z^2}$ are the mean square of the streamwise and spanwise fluctuating vorticity, respectively, and $\overline{W^2}$is the mean square of the fluctuating vorticity vector.)

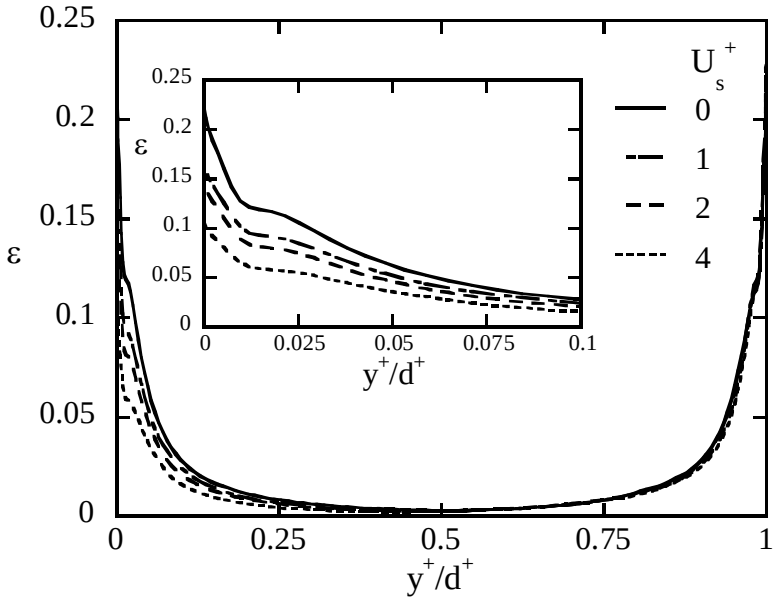
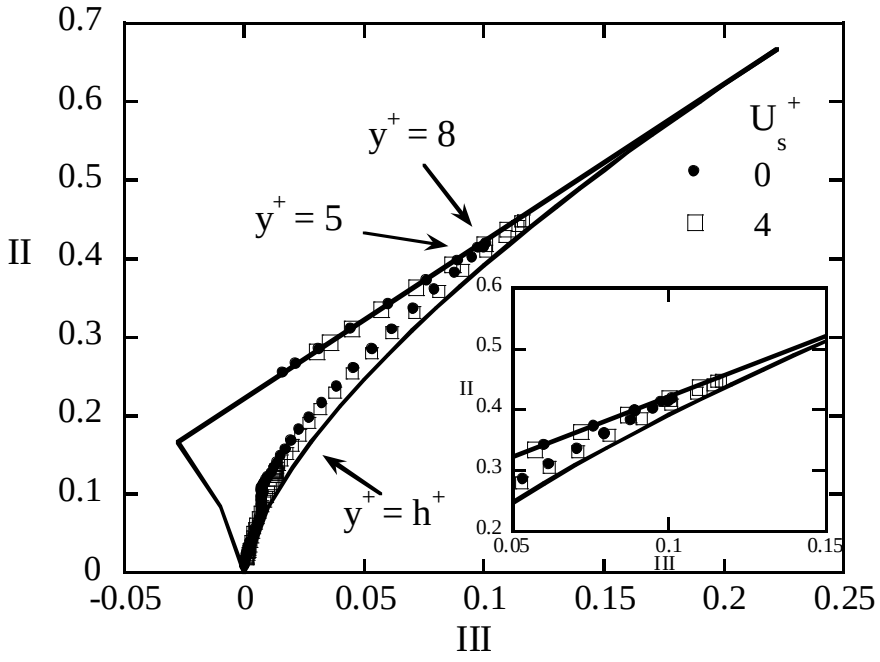


Figure 3.16. Total dissipation rate in Poiseuille and Poiseuille-Couette flow with U_s^+ = 1, 2 and 4.

(a)



(b)

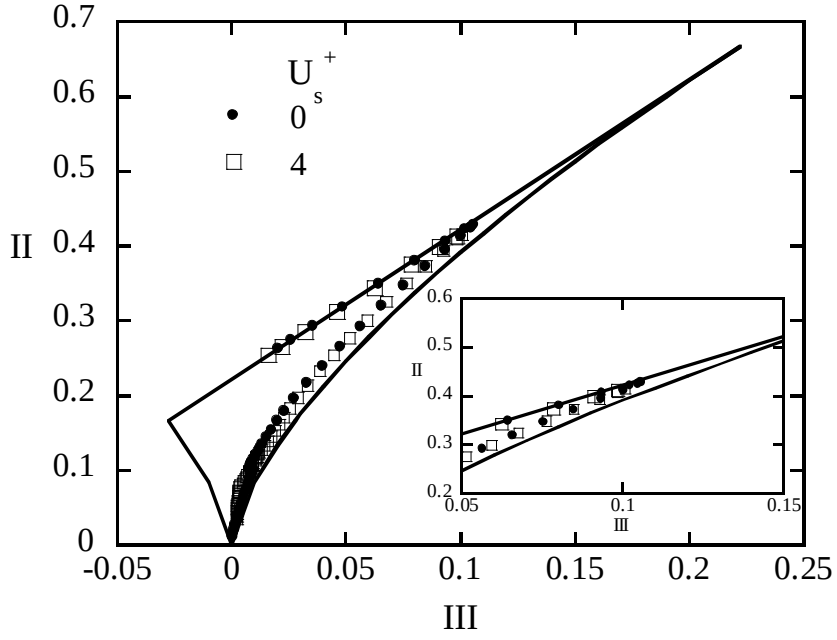
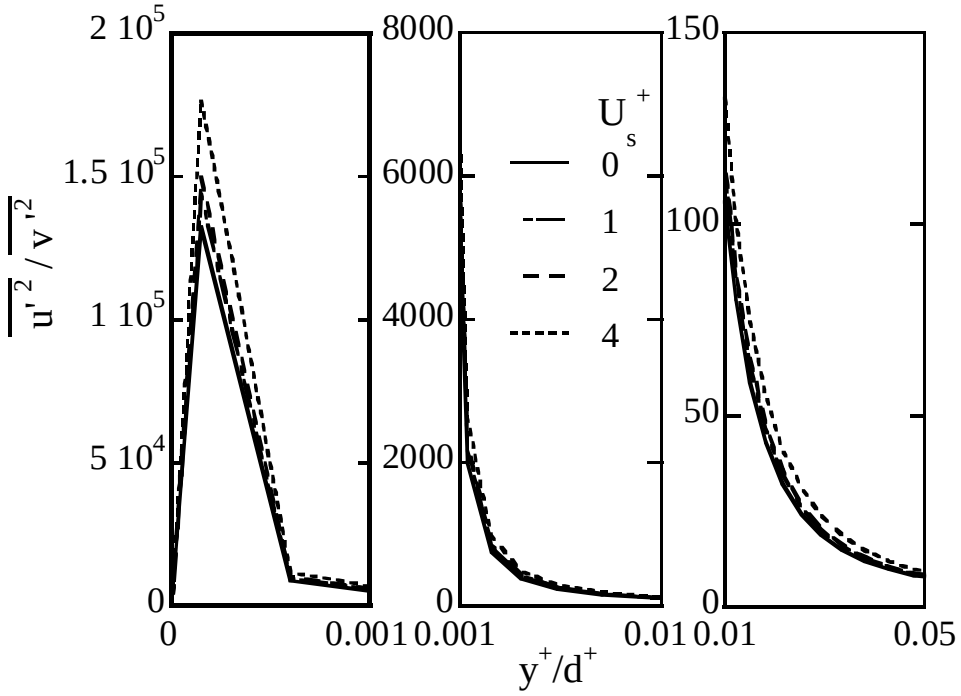


Figure 3.17. The Lumley triangle on the plane of the invariants II and III of the Reynolds stress anisotropy tensor: (a) Points close to the moving wall; (b) Points close to the stationary wall. The inset figures focus on the location of zero crossing of the Reynolds stress

(a)



(b)

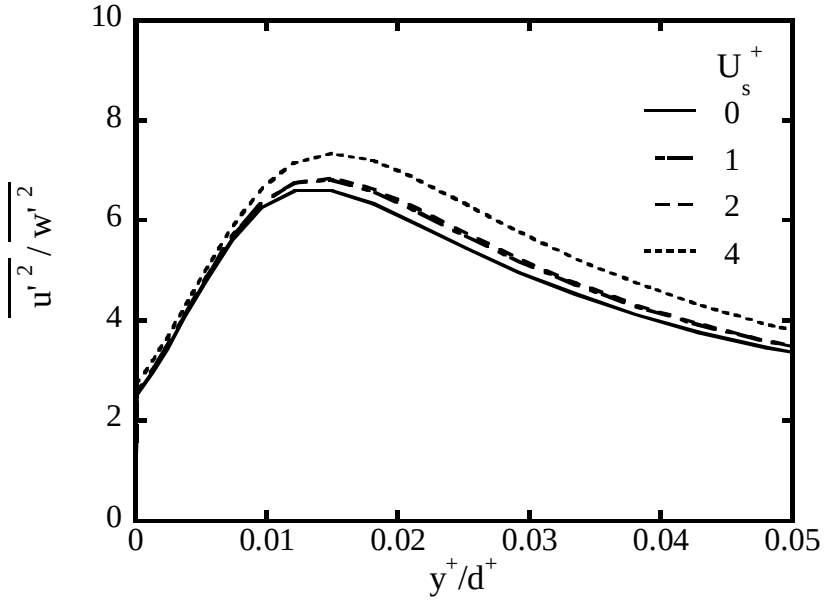


Figure 3.18. Ratio of turbulence intensity in the streamwise direction over intensity in (a) the normal direction, and (b) the spanwise direction. The ratio increases with an increase of the slip velocity.

Chapter 4. Flow-induced Separation in Wall Turbulence

4.1 Introduction

Separation of particles in a flow field is important in many processes, such as biological analysis, environmental assessment and food processing. As the number and applications of microfluidic devices increase, different separation techniques, both passive and active, have been employed not only in the laboratory but also in industry. While passive techniques only rely on the flow field and device geometry, active techniques utilize effects of external fields for better performance (92). Some popular passive techniques are pinched flow fractionation (PFF) (93-95), inertia and dean flow fractionation (96, 97), membrane-based methods (98-102), and hydrodynamic filtration (103, 104). Active techniques could use electric fields (105-108), centrifugal forces (109, 110), or different types of external field as in field-flow fractionation (111-114).

In most of these cases, the flows are at rather low Reynolds number. On the other side, separation of particles in turbulence has not been explored. Instead, particle transport related issues have been investigated with a focus on turbulent mixing (115-117) and particle dispersion (118-123). This is because the fluctuating velocity in turbulence usually leads to rapid mixing, instead of separation. In this work we present the opposite, the case where particles can be separated in turbulence without using any means other than the turbulent flow field.

4.2 Simulation parameters and procedure

A numerical method that involves a combined direct numerical simulation (DNS) of the flow field and Lagrangian scalar tracking (LST) of mass markers is used.

The pseudo-spectral DNS algorithm documented by Lyons et al. (63), and validated with experiments by Gunther et al. (64) is implemented. All variables are made dimensionless using the friction velocity, u^*, and the kinematic viscosity of the fluid, ν, namely, the *viscous wall units*. The dimensions of the computational box are $4\pi h$ x $2h$ x $2\pi h$ in the streamwise, x, normal, y, and spanwise, z, directions, respectively, where h = 300 is the half channel height. The computational box is meshed with 256 x 129 x 256 grid points in the x, y and z directions. The Reynolds number based on the mean centerline velocity and half of the channel height is 5,700. The channel is simulated as infinitely long in x and z and with periodic boundary conditions with periodicity lengths of $4\pi h$ and $2\pi h$, respectively. No-slip and no-penetration boundary conditions are imposed at the rigid channel walls. The fluid flowing in the channel is an incompressible Newtonian fluid with constant density and viscosity.

Scalar markers that represent mass particles are released into the flow field. These markers are passive and do not affect the flow field, which is realistic for dilute solutions. The tracking algorithm of Kontomaris et al. (71) is used to track individual trajectories of these markers in space and time in a Lagrangian framework, in conjunction with the DNS. The combined DNS/LST approach has been previously used to study heat transfer in high Prandtl or Schmidt number fluids (72, 73). Discussion about the accuracy of this method and comparisons of the results with experimental findings can also be found in previous publications (67, 74-76).

Mass markers are released into the flow field after the velocity field reaches steady, fully developed state. If $\vec{V}(\overrightarrow{x_0}, t)$ is the Lagrangian velocity of a particle that was

at location $\overrightarrow{x_0}$ at time $t = t_0 = 0$, then the position $\vec{X}(\overrightarrow{x_0}, t)$ of the marker at time t is calculated based on the equation

$$\vec{V}(\vec{x}_0, t) = \frac{\partial \vec{X}(\vec{x}_0, t)}{\partial t} \tag{4.1}$$

At this point we make a basic assumption that a marker at any time has the velocity of the fluid particle on which it rides, which means that the relation between the Lagrangian velocity and the Eulerian velocity $\vec{U}$ is $\vec{V}(\vec{x}_0, t) = \vec{U}[\vec{X}(\vec{x}_0, t), t]$. Since the mass markers can move off a fluid particle due to molecular diffusion, the diffusion effect has been represented by adding a random walk on the marker motion after each simulation time step. The value of the diffusion step is estimated by a Gaussian distribution in each space direction with a zero mean and a standard deviation, σ, depending on the Schmidt number, *Sc*, ($\sigma = \sqrt{2\Delta t^+/Sc}$) where Δt^+ is the time step of the simulation. Multiple values of *Sc* are examined (*Sc* = 0.1, 0.7, 6, 20, 50, 100, 200, 500, 1000, 2400, 7500, 15000, 30000, 40000, and 50000) representing different substances. For each *Sc*, 10000 markers are released instantaneously at the entrance of the computational box (x = 0). The markers are distributed with uniform spacing ($2\pi h/10000$) from a line in the spanwise direction. To study the effect of the vertical position of release, markers are also released at different elevated locations, y_o = 0, 1, 2, 4, 5, 7, 9, 11, 13, 14, 15 wall units away from the bottom wall.

4.3 Results and discussion

4.3.1 Flow-induced separation

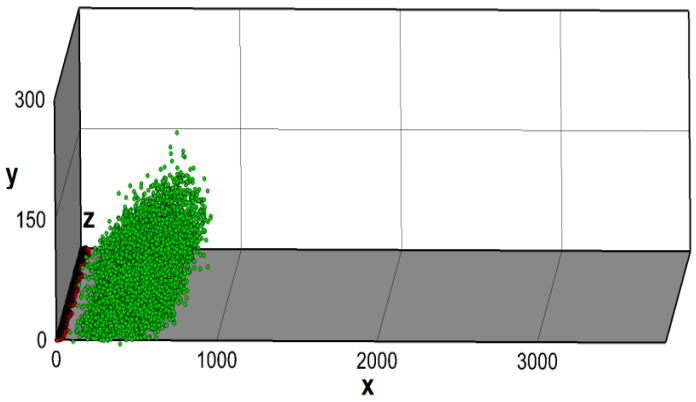
With the term *flow-induced separation* we mean that turbulence in a flow field can be used for particle separation when different particles have different diffusivity.

Previous results in our laboratory have shown that markers with lower *Sc*, released at the channel wall, would diffuse into the flow field faster than markers with higher *Sc* (75). This effect is clearly shown in Figure **4.1**, in which positions of markers with *Sc* of 0.1 and 500 at different times are displayed. Both types of markers were released into the turbulent flow field from the bottom wall ($y_o = 0$), at the same line ($x = 0$) and at the same time. The markers painted green are the markers with $Sc = 0.1$ and the crimson markers have $Sc = 500$. It is seen that the $Sc = 0.1$ markers form a leading cloud, while a trailing cloud is formed by the $Sc = 500$ markers. This is caused due to the differences in the diffusivity of the two types of particles. Low *Sc* markers have high molecular diffusivity, so they can diffuse with larger Brownian random motion jumps away from the near-wall region, where they can get convected by the larger turbulent velocity fluctuations in the *y* direction and by larger mean velocity in the streamwise direction. High *Sc* markers have low diffusivity and they cannot leave the region next to the channel wall as fast as the lower *Sc* markers, so they are trapped in a low velocity region for a long time.

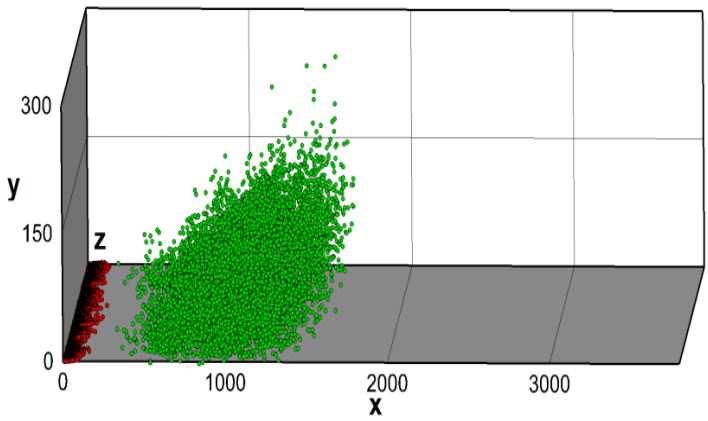
At this point, it is convenient and necessary to define an *overlap region* based on the streamwise location of the clouds of markers with the two different *Sc*. The overlap region is the region between the slowest moving marker of the leading cloud and the fastest moving marker of the trailing cloud. The number of markers from each cloud within the overlap region can be used to quantify the separation of the two clouds. In Figure **4.1**, as time advances, a clear separation can be observed between the leading and the trailing clouds. Eventually, however, the trailing cloud will catch up with the leading cloud forming a short overlap region. This happens because at some point in

time several markers from the trailing, high *Sc* cloud, will leave the viscous sublayer close to the channel wall and will start moving fast due to the turbulent mean flow, while some of the low *Sc* particles will diffuse back in the viscous wall region and will move slower than the rest of the particles of their type. The number of particles present in the overlap region reduces to zero when separation occurs, and becomes some finite number when the trailing cloud catches up with the leading cloud.

(a)



(b)



(c)

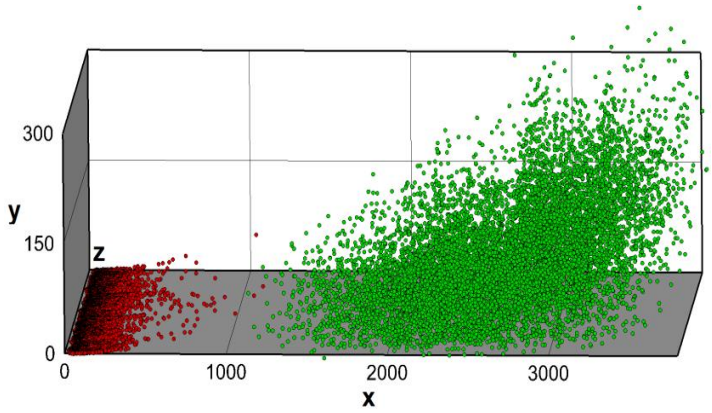
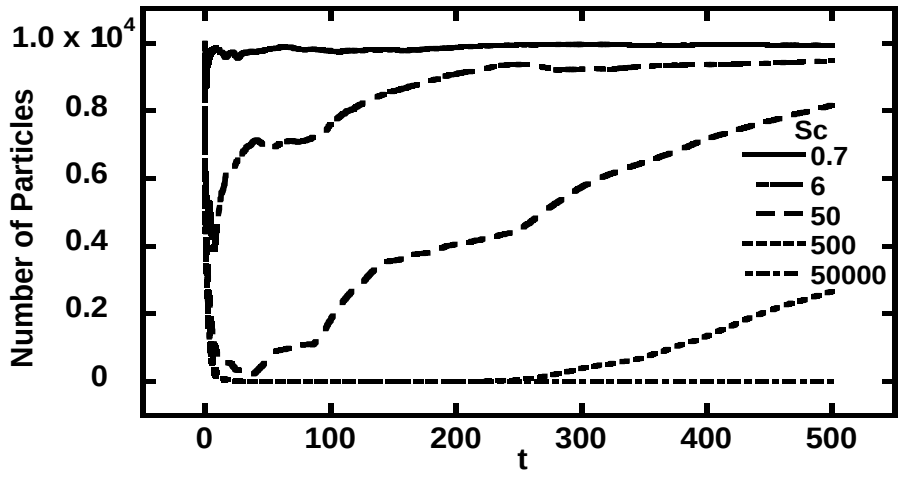


Figure 4.1 Locations of markers with Sc = 0.1 (green) and 500 (crimson) at different times from their simultaneous release: a) t = 50; b) t = 100; c) t = 220. Clear separation between the two clouds is observed in panel (b), while a thin overlap region is observed.

To explore the effects of *Sc* on particle separation, the number of markers in the overlap region of two clouds is shown in Figure **4.2** for several cases with different *Sc*. In all these cases, the *Sc* = 0.1 markers always form the leading cloud, while the trailing cloud is formed by markers with *Sc* = 0.7, 6, 50, 500 or 50000. All markers are released simultaneously from the channel wall, at $y_0 = 0$. It is apparent that the two clouds with the largest *Sc* difference show the least number of markers in the overlap region for the longest time. As the *Sc* for the two clouds becomes comparable, there does not exist a time at which the overlap region disappears and separation does not occur.

Markers are also released from different sources elevated away from the wall at locations mentioned previously. In Figure **4.3**, we show the number of markers from the leading cloud, in (a), and trailing cloud, in (b), that are in the overlap region for markers with *Sc* = 0.1 and *Sc* = 2400 released at *y* = 0, 5 and 15. It is obvious that separation occurs most effectively when the markers are released from the wall.

(a)



(b)

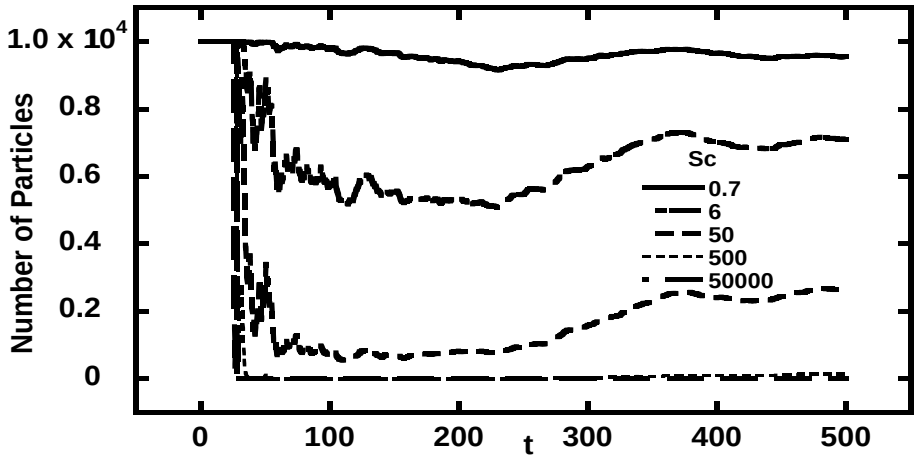
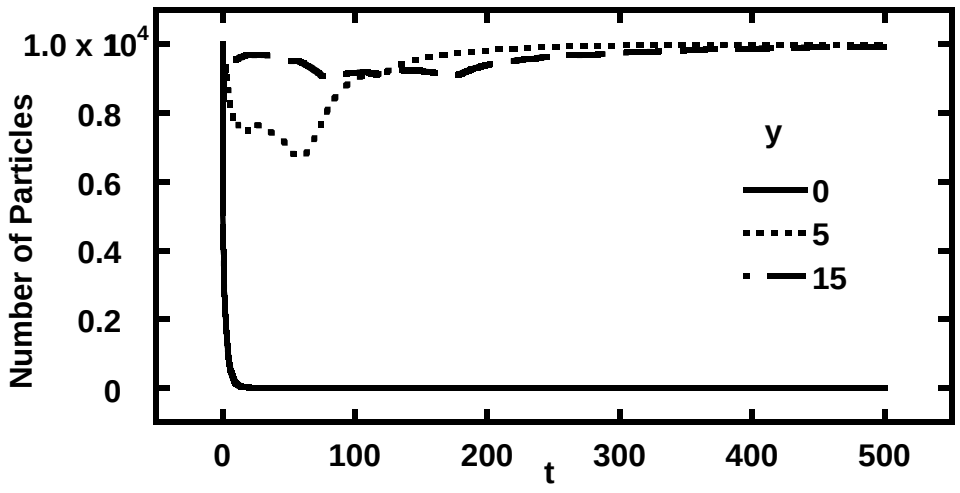


Figure 4.2 Number of markers in the overlap region, Nov, when markers with Sc = 0.1 are released simultaneously with markers of different Sc. a) Number of markers from the leading cloud, Sc = 0.1; b) Number of markers from the higher Sc trailing cloud.

(a)



(b)

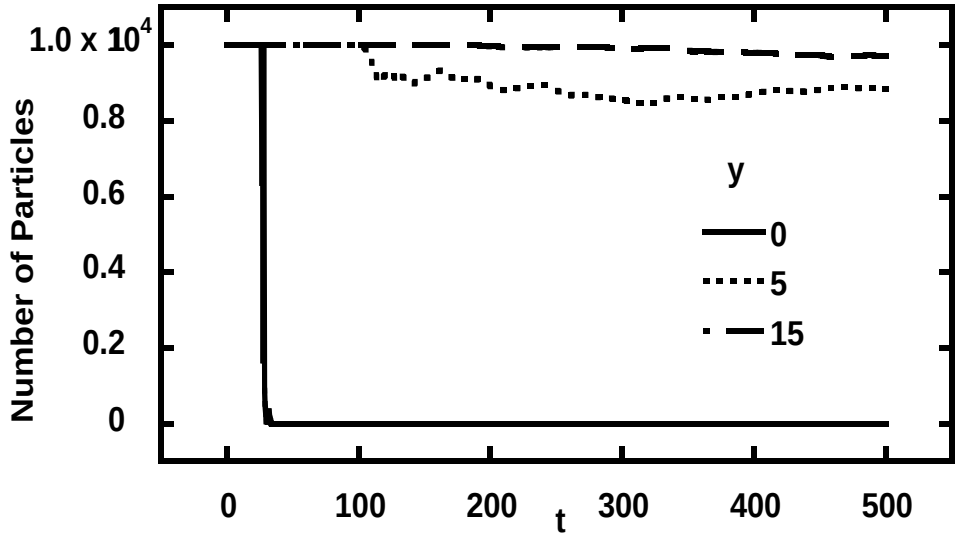


Figure 4.3 Number of markers in the overlap region when markers with Sc = 0.1 and 2400 are simultaneously released at different initial vertical positions; a) markers of the leading cloud; b) markers of the trailing cloud.

4.3.2 Separation Mechanism

The question that arises now is what the mechanism behind this type of separation is, and whether there is any constraint for a successful separation. Herein, we consider the two clouds to be separated if less than 0.5% of the total number of markers of any cloud (leading or trailing) is present in the overlap region. It has been shown above that if the two *Sc* are too close to each other, separation would not occur. In Table 4.1, we present the minimum value of the higher *Sc* for each of the lower *Sc* in order for separation to occur. To smooth out fluctuation effects in the instantaneous flow fields, three different simulations with different initial velocity fields were used to calculate the reported results, which were determined as average values from the three runs.

The physics of why the separation occurs can be revealed when one considers the development of an instantaneous cloud of particles released in a turbulent flow field – this cloud is usually called a *puff*. Careful experiments have shown that there are different zones of development of a puff, which are distinct based on the physical mechanism of dispersion that is dominant in each zone (124, 125). Simulations have also shown that when markers are released into the flow field, they move through three stages: zone I, in which molecular diffusion dominates dispersion; zone II, which is a transition zone; and, finally, zone III, in which turbulent convection dominates dispersion. Within zone I there is a zone in which 95% of particle displacement happens because of molecular diffusion. The average time spent by markers of different *Sc* in this first zone, τ_{95}, and the time at which the particles move into zone III, τ_{II} , are also included in Table 4.1, as obtained through the following empirical equations (75):

$$\tau_{95} = 8.34 * Sc^{0.38} \qquad (4.2)$$

$$\tau_{II} = 101.2 * Sc^{0.35} \qquad (4.3)$$

Table 4.1 Summary of cases of low and high Sc, in which separation is observed using the 0.5% purity criterion. The transition times τ_{95} and τ_{III} are also presented.

Low *Sc* (τ_{III})	0.1 (46)	0.7 (90)	6 (190)	20 (289)	50 (398)	100 (507)
High *Sc* (τ_{95})	100 (48)	500 (89)	7500 (248)	15000 (323)	30000 (420)	40000 (468)

The ratio R_t of the τ_{III} of the low *Sc* over the τ_{95} of the high *Sc* of all successful separation cases is related to the separation time (defined as the time at which separation begins, τ_S). The correlation obtained is shown in the following equation and plotted in Figure 4.4

$$\tau_S = a * \exp(b*R_t^2) \qquad (4.4)$$

with values of the two parameters found to be $a = 11$, $b = 2.5$.

The ratio R_t in Equation (4.4) gives information about the difference of the relative motion of markers with these two *Sc*. It is observed that separation will happen faster if this ratio becomes smaller. If the ratio is smaller than 1 (which happens for successful separation cases), it is implied that markers with lower *Sc* enter zone III before the markers with higher *Sc* leave zone I. Turbulent convection is the dominant transport mechanism in zone III – this means that the leading cloud gets accelerated by turbulent convection before the trailing cloud exits the molecular diffusion regime. This process would cause the two clouds to separate. The two cases that have this ratio slightly larger than 1 (1.01 and 1.08) are very close to the limit for classifying a case as successful separation (99.5% of the clouds are separated). For this study, where we defined separation as the point at which 0.5% or less of a cloud can be in the overlap region, the upper limit of R_t is 1.08. If the ratio gets higher, more markers with high *Sc* would leave zone I before markers with low *Sc* enter zone III. Because of that, more

high *Sc* markers accelerate and catch up with the low *Sc* markers and the needed purity constraint will not be satisfied.

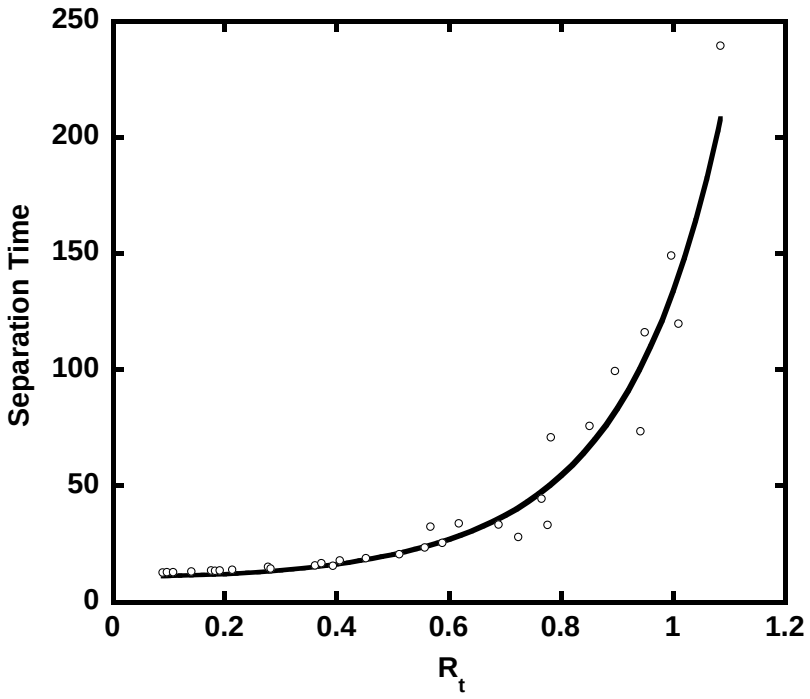


Figure 4.4 Separation time as a function of the ratio R_t of the τ_{III} of the low Sc over the τ_I of the high Sc. The solid line is Equation (4.4).

Since the times for zone transitions occur as a function of *Sc* in Equations (4.2) and (4.3), the limit 1.08 of the time zones ratio can be expressed as a relationship between the *Sc* of the particle cloud pairs. In order to have separation then, it is required that

$$\frac{Sc_{Low}}{Sc_{High}} \leq 0.001 * Sc_{High}^{0.09} \qquad (4.5)$$

Given the separation criterion of 0.5% and Equation (4.5) as a constraint for achieving separation, this method could be employed in practice. For example, consider the separation of colloidal particles (with radii between 1nm and 1μm) in water at room

temperature. Using the equations below (126), one can calculate the corresponding *Sc* of a particle with a given size, as

$$D_{AB} = \frac{\kappa T}{6\pi\mu_B R_A} \tag{4.6}$$

$$Sc = \frac{R_A 6\pi\mu_B \nu}{\kappa T} \tag{4.7}$$

where D_{AB} is the diffusivity of particle A in the continuous phase B, T is the absolute temperature, κ is the Boltzmann constant, R_A is the radius of the spherical particle A, μ_B is the dynamic viscosity and ν is the kinematic viscosity of the continuous phase. Since the *Sc* depends linearly on the radius, one can easily calculate the ratio of *Sc*, and check whether Equation (4.5) is satisfied.

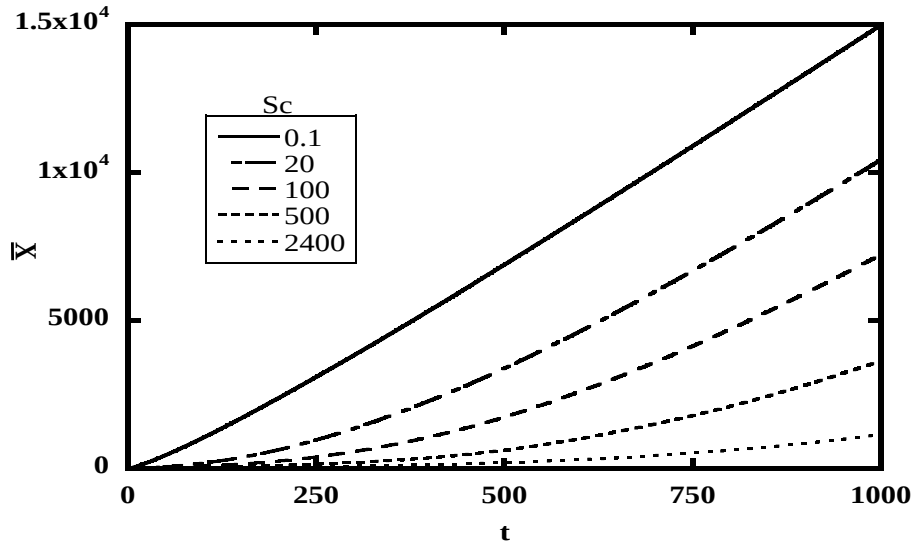
As an example, this method could be applied to separate viruses from red blood cells in normal saline 0.9% as the continuous phase. This is an example that is offered as a proof of concept calculation. Given that the diffusivity value of red blood cells in water is 10^{-13} (m^2/s) (127), and assuming that the viscosity and density of normal saline are equal to those of water due to very low concentration of sodium chloride, the corresponding *Sc* of red blood cells in saline is about 10^7. Different types of viruses, with diameters ranging from 10nm to 100nm (128), would have *Sc* from 23,445 to 234,450 (for instance, the diameter of HIV virus is 100nm and the *Sc* is 234,450). Therefore, if a mixture of red blood cells and viruses is released in pulses into a flow field, the viruses will leave the cells behind (with the high *Sc* equal to 10^7). Using Equation (4.5), it is obvious that some types of viruses will not satisfy the 0.5% criterion for separation. Significant separation will, however, occur in the overlap region, and then one can achieve further separation by repeating the process several times.

4.3.3 A Model for Particle Displacement

Einstein (40) developed the following relation for molecular dispersion in a non-turbulent field $\frac{d\overline{X^2}}{dt} = 2D$, where D is the molecular diffusivity and X is the displacement from the source. The most influential contribution to the theory of dispersion in a turbulent field is Taylor's description of the dispersion of particles from a point source in a homogeneous, isotropic turbulence (41). With respect to anisotropic turbulent flows, Batchelor (129) modified Taylor's theory to predict the statistical behavior of a cloud dispersed from a source in a turbulent boundary layer. We examine here whether Taylor dispersion can be used to reproduce the simulation results and whether particle separation can be predicted based on Taylor's and Batchelor's models, bypassing the need to conduct DNS and LST.

First, we examine the mean displacement of the particles in the streamwise and vertical directions. Results for selected *Sc* are presented in Figure **4.5**. It is obvious, however, that differences in the mean values of streamwise displacement should not be used alone in predicting separation with a criterion like the 0.5% criterion used above, since they only represent mean positions of the clouds without any indication of the spread of the clouds in *x*.

a)



b)

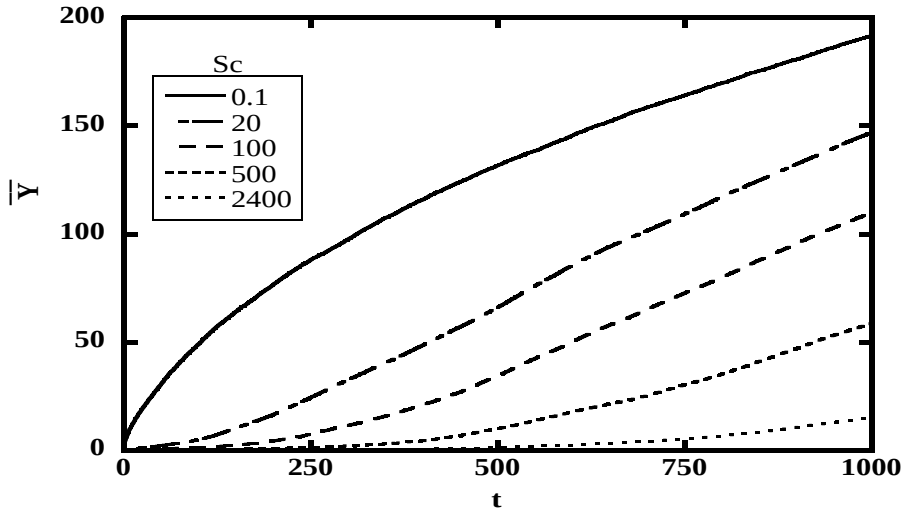


Figure 4.5 Mean displacement of particles with different Sc in: a) streamwise direction; b) vertical direction. Data obtained from LST simulations.

The displacement of particles in the vertical direction plays a significant role in determining streamwise velocity and position of a cloud. As previously described, particle clouds go through three different zones of development after they are released from a source at the wall. It appears that for every *Sc* the transition to zone III occurs

when the mean cloud distance from the wall is $\bar{Y} \approx 30$. At that point, at t = τ_{III}, the cloud enters the zone where turbulent convection dominates the dispersion process. Identifying the proper dispersion mechanism in each zone would help build a model to predict displacement in the channel. In zone I, our earlier study found that dispersion in the direction of the velocity gradient, *y*, agrees well with the theory of Einstein and Taylor (75). Since molecular diffusion is the dominant mechanism in this zone, we propose the following model for the mean vertical displacement:

$$\bar{Y} = C * Sc^{d} t^{e} \qquad \text{for } t < \tau_{95} \qquad (4.8)$$

The model contains the effect of molecular motion only. As previously discussed, the value of the diffusion step is estimated by a Gaussian distribution in each space direction with a zero mean and a standard deviation, σ, which is proportional to $Sc^{-1/2}$. The exponent d in Equation (4.8) can therefore be chosen to be $-\frac{1}{2}$. The coefficients *C* and *e* were then found to be 0.89 and 0.55, respectively, by fitting the equation with our LST data, as seen in Figure **4.6**.

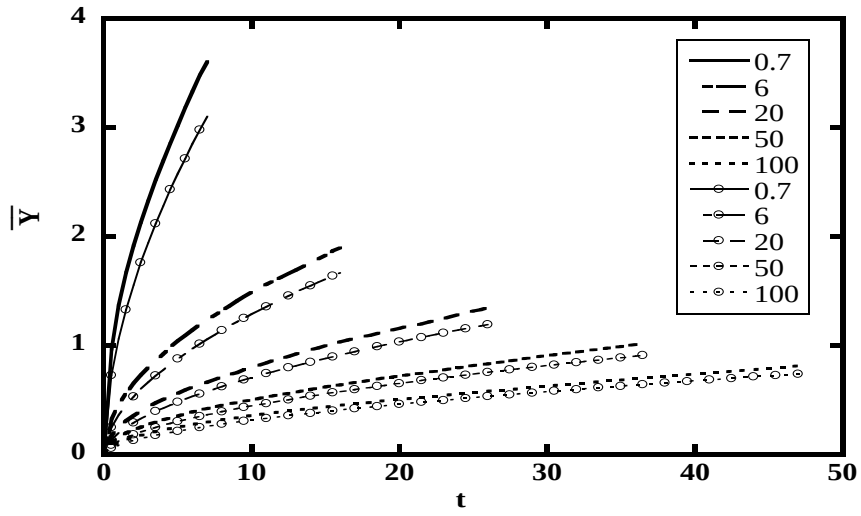


Figure 4.6 Prediction of vertical displacement in zone I: comparison between the model of Equation (4.8) (lines marked with open circles) and LST results (lines without any markings).

In the case of shear flow, as is the case with our channel geometry, Batchelor suggested that the following expression can be used to predict the average motion of particles dispersing in the turbulent constant stress region (129)

$$\bar{V} = \frac{d\bar{Y}}{dt} = bu^* \qquad (4.9)$$

where b = 0.2 should be a universal constant according to Batchelor. This expression implies that particles with different *Sc* will have the same mean vertical velocity. Plotting $\bar{Y}$ versus time for different *Sc* in the log layer region ($\bar{Y} \geq 30$ or $t \geq \tau_{III}$) can be used to compare our LST data to Batchelor's prediction, as seen in Figure **4.7**. It is observed that particles move in the vertical direction with almost constant velocities, though particles with different *Sc* have slightly different velocities, and low *Sc* particles tend to have higher velocities initially that decreases as time increases. Because of this, we propose that the Batchelor constant *b* has values that depend on the *Sc*, as shown in Table **4.2**. These values agree well with previously published results by different authors (130-132).

Table 4.2 Batchelor's constant b for different Sc

Sc	**b**
0.1	0.3
0.7	0.3
6	0.25
20	0.2
50 and above	0.15

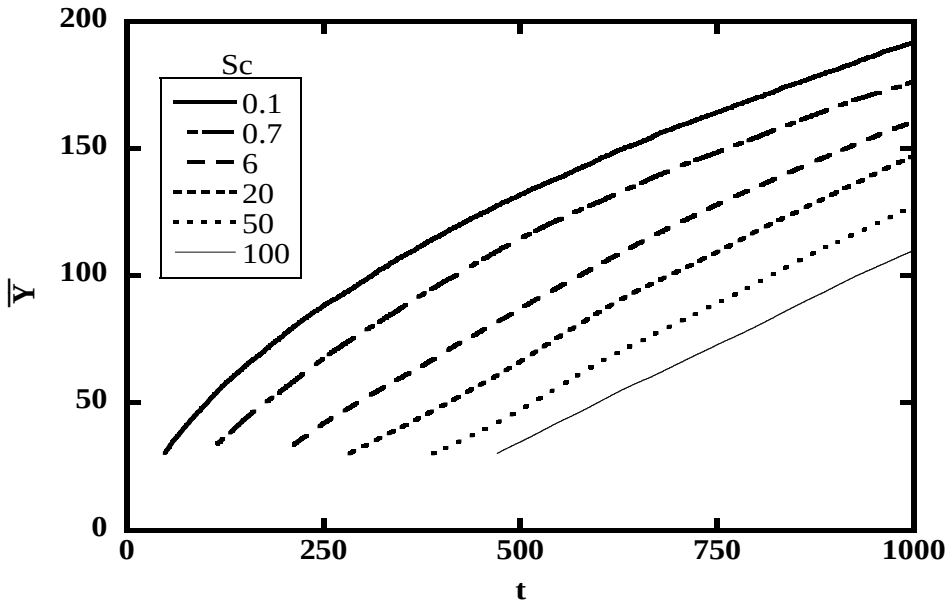


Figure 4.7 Mean vertical displacement of particles in the log layer. Data obtained from LST simulation.

Though diffusion mechanisms of particles in the vertical direction within zone I and zone III have been identified with corresponding description [Equations (4.8) and (4.9)], diffusion in the transition zone, starting from τ_{95} to τ_{III}, remains to be determined. Since the transition zone lies between zones I and III, we suggest the following expression to determine the vertical mean displacement for $\tau_{95} < t < \tau_{III}$, based on information from zones I and III:

$$\bar{Y}_t = \bar{Y}_{t-1} + \left[\frac{d\bar{Y}}{dt}_{t=\tau_{95}} + \left(\frac{t-\tau_{95}}{\tau_{III}-\tau_{95}}\right) * \left(b - \frac{d\bar{Y}}{dt}_{t=\tau_{95}}\right)\right] * \Delta t \qquad (4.10)$$

in which b is Batchelor's constant, and Δt is the time step between times t and (t-1). Using Equations (4.8) – (4.10) as a model, the mean vertical displacement of each *Sc* particle is plotted in Figure 4.8 and compared with LST results. Since separation of particles happens for $t < 200$, only results up to $t = 200$ are plotted in Figure 4.8. Reasonable agreement between our LST data and results from this model is obtained. It is worth noting that Equations (4.8) – (4.10) were developed based on the theories of

Einstein, Taylor and Batchelor, and this agreement encourages the use of these theories to predict mean displacement in a direction normal to the mean flow for small times.

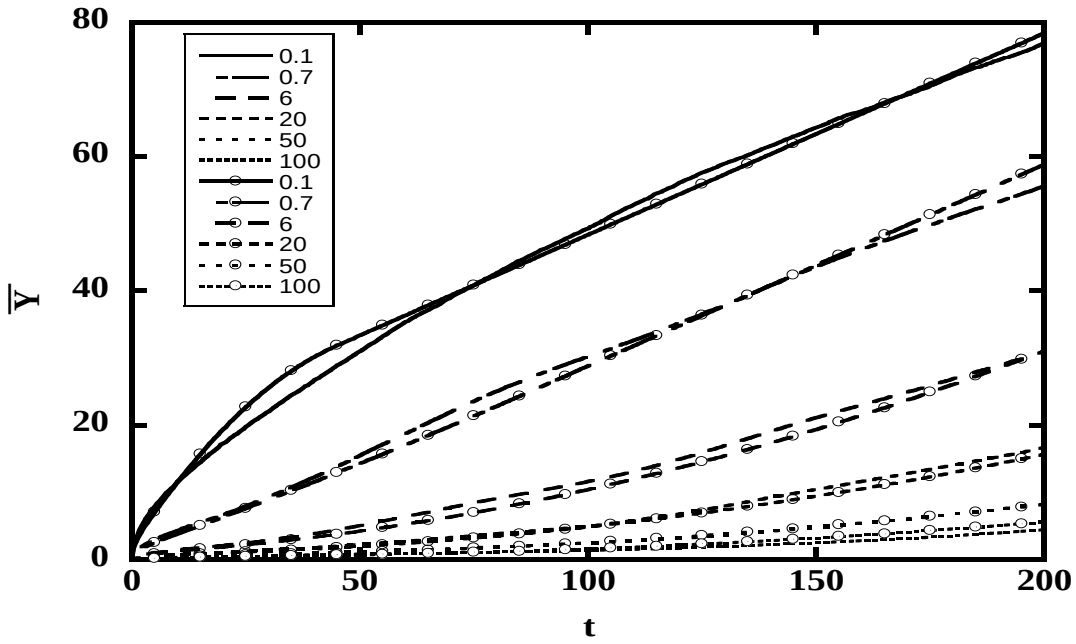


Figure 4.8 Mean vertical displacement of different Sc. Results obtained from the LST data (lines without markers) and with our model based on Equations (4.8)-(4.10) are presented (lines marked with open circles).

Batchelor (129) further assumed that a constant *c* exists such that the mean Lagrangian velocity of a particle cloud in the streamwise direction equals the Eulerian velocity located at c$\bar{Y}$, this is due to the decrease of dU/dy with height in the channel. Based on this assumption, we have the following equation

$$\bar{V}_x = \frac{d\bar{X}}{dt} = [\bar{U}(y)]_{y=c\bar{Y}} \qquad (4.11)$$

It is now necessary to determine the mean velocity in the channel. Based on our DNS study, the mean flow field velocity in the channel could be described as below

$y \leq 5$: $U = y$

$5 < y \leq 30$: $U = 4.9*\ln(y) - 3$

$30 < y$: $U = 2.6*\ln(y) + 4.5$

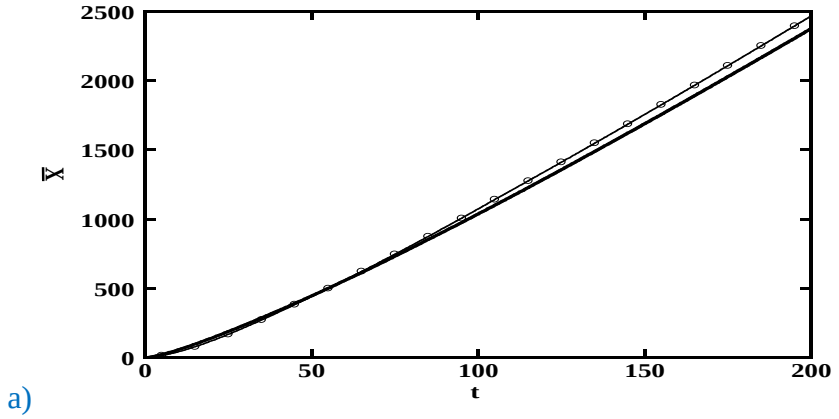
Having information of velocity in the channel and an appropriate constant c, one can use Equation (4.11) to calculate $\bar{V}_x$, thus obtain $\bar{X}$ of a particle cloud. Based on our LST data, c = 0.6 is the best fit, as seen in Figure **4.9**, and could be used in Batchelor's theory to predict mean streamwise displacement in the channel.

At this point, it is seen that modified Taylor and Batchelor's theories produce similar results to our DNS-LST method, in terms of mean displacement in *x* and *y* directions. A further attempt is made to determine if using mean displacement as a main tool could predict separation at reasonable accuracy. However, as explained above, the mean displacement should not be used alone in predicting separation with high purity criterion. Because of turbulent velocity fluctuations the particle clouds stretch forward and backward. The stretching of the clouds also depends on molecular diffusion. We hereby define the standard deviation (STD) for the particle position in each *Sc* by the following expression

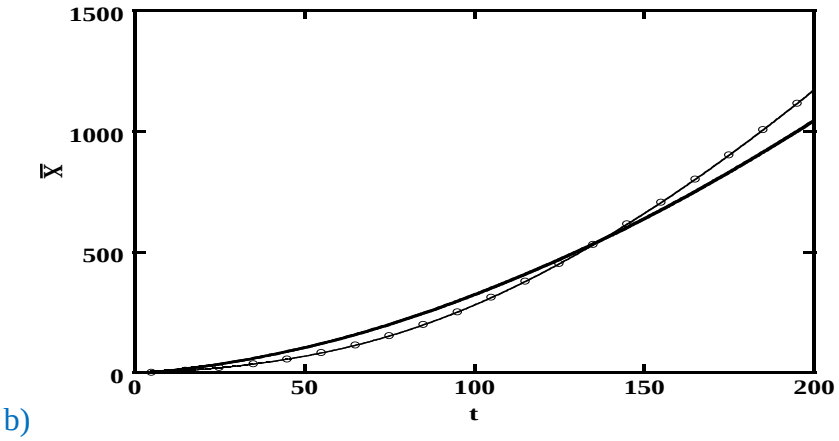
$$STD = \overline{(x - \bar{X})^2}^{1/2}$$

in which $\bar{X}$ represents mean location of the particle cloud that varies with time, and *x* indicates the location of each particle. Since no particle distribution function in *x* is available at this time, we assume that the concentration distribution in a particle cloud follows a normal distribution. Therefore, 99% of the particle population in the streamwise direction would lie within boundaries determined by adding and subtracting 2.5 times the STD to and from the mean streamwise displacement (which is also the cloud mean streamwise position). In Figure **4.10**, we plot calculations for two pairs of *Sc* that have been found to separate when applying the 0.5% purity criterion. For each *Sc*, the front and back boundaries of 99% of the population in the *x* direction are plotted as time increases, using $\bar{X}$ and STD from the LST data. The results inticate that clouds

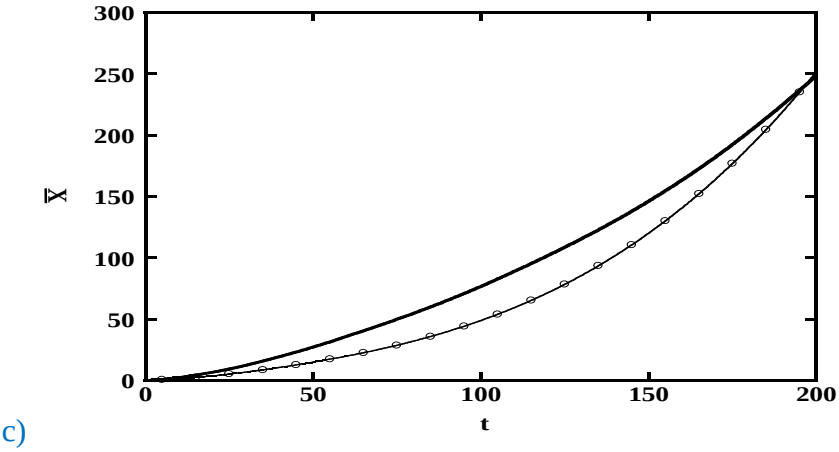
with *Sc* =0.7 and 30000 would not be able to separate from each other at any time earlier than 100, while that number is 512 for *Sc* = 6 and 7500. However, by counting the number of particles left in the overlap region, we found that *Sc* = 0.7 and 30000 would separate from time equal to 14, while *Sc* = 6 and 7500 separate from time equal to 45. The disagreement indicates that the normal distribution is not an accurate approximation for the concentration distribution in *x*, One should rely on previously presented tools, i.e., Equations (4.2) – (4.5), to predict separation. However, the models that we developed to predict $\bar{X}$ and $\bar{Y}$ could still be used for other applications, or to predict separation, if one could obtain a more accurate particle distribution function.



a)



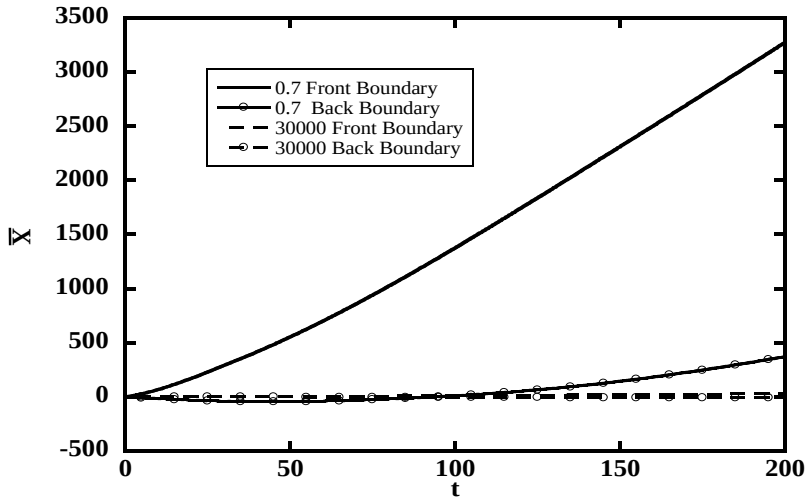
b)



c)

Figure 4.9 Mean streamwise displacement of different Sc: a) Sc = 0.1, b) Sc = 6, c) Sc = 100. Results are obtained from LST data (lined without markers) and Batchelor's model (lines marked with open circles).

(a)



(b)

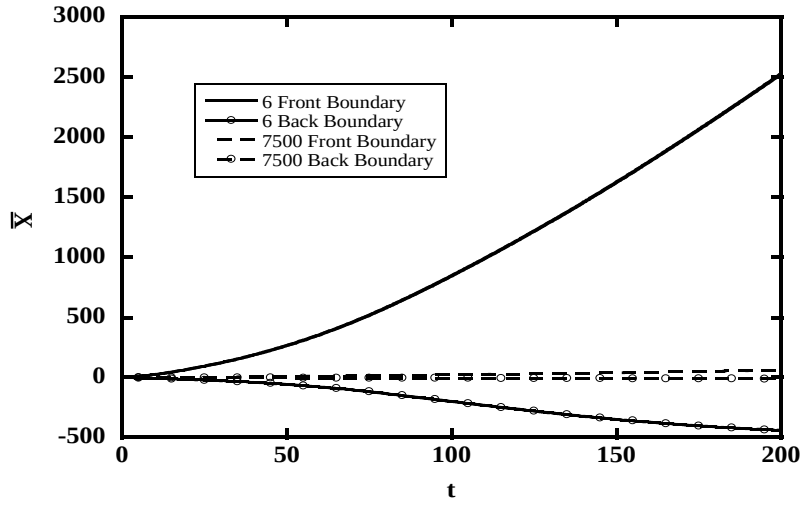


Figure 4.10 Front and back boundaries of 99% of population of clouds in the streamwise direction, using mean displacement and normal distribution to predict the concentration distribution. (a) Prediction for clouds with Sc = 0.7 and 30000 and (b) prediction for clouds with Sc = 6 and 7500

Chapter 5. Probability Density Function of a puff dispersing from the channel wall

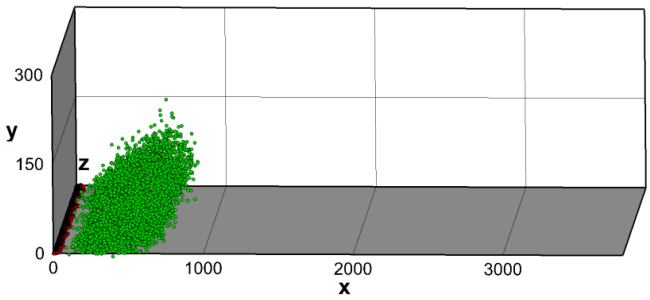
5.1 Introduction

One critical characteristic of turbulence is its ability to promote mixing. In fact, most particle transport related studies have focused on turbulent mixing (115-117, 133, 134) and particle dispersion (118-122, 135). On an opposite direction, we reported in Chapter 4 the separation of particles with different Schmidt numbers that happens when particles are released into turbulent flow field from the same location on a channel wall (136). Motion of two puffs of particles with Sc numbers of 0.1 and 500, released into the channel from the same line source on the bottom wall, is plotted in Fig. 1 in which separation of the two puffs was clearly observed.

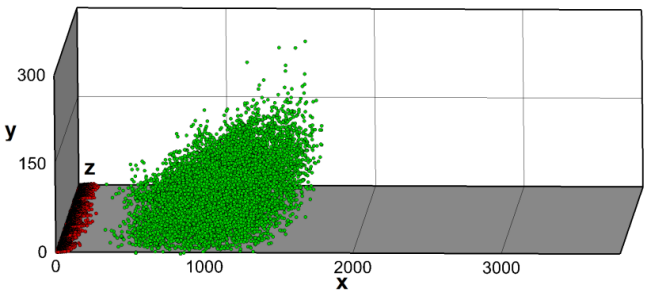
The mechanism behind this separation could be revealed when considering the development of an instantaneous cloud of particles released in a turbulent flow field – this cloud is usually called a puff. Experiment studies have found that there are different zones of development of a puff, which are distinct based on the physical mechanism of dispersion that is dominant in each zone (137, 138) Simulations have also shown that when markers are released into the flow field, they move through three stages: zone I, in which molecular diffusion dominates dispersion; zone II, which is a transition zone; and, finally, zone III, in which turbulent convection dominates dispersion (75). Separation between two clouds of particles with different diffusivity values was found to happen if the cloud with higher diffusivity enters zone III before the one with lower

diffusivity leave zone I. Turbulent convection, which is the dominant transport mechanism in zone III, accelerates the leading cloud and lead to separation of the two clouds.

a)



b)



c)

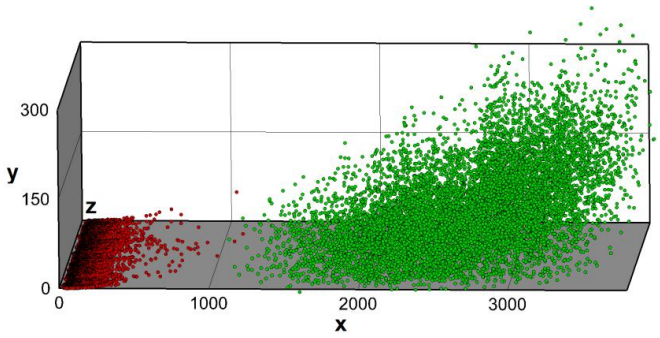


Figure 5.1 Locations of markers with Sc = 0.1 (green) and 500 (crimson) at different times from their simultaneous release: a) t = 50; b) t = 100; c) t = 220. Clear separation between the two clouds was observed in panel (b), while a thin overlap region was

observed at $x \approx 1000$ - 1200 in panel (c). (Only the bottom half of the channel is shown, from $y = 0$ to 300)

In the aforementioned study, we used Direct Numerical Simulation (DNS) and Lagrangian Scalar Tracking methods (LST) to simulate the turbulent flow field and track the particle motion. An attempt was also made to develop a reduced order model that could predict the location of the puffs and estimate separation, thus avoiding the need to perform DNS and LST. Batchelor's theory was modified to predict the statistical behavior of a puff dispersed from a source in a turbulent boundary layer and to estimate mean streamwise displacement of the puffs. While the agreement between Batchelor's theory and our numerical results was reasonable, there remained a concern as one would need to determine the lower and upper boundaries of the puff, in order to determine if separation could happen.

In this paper, we explore the form of the particles distribution and we present the finding that Gamma 3P distribution is an appropriate probability density function (pdf) for use in predicting location and concentration distribution of puffs of particles with different Schmidt numbers (Sc) diffusing from the wall of a channel. Estimation of parameters of the Gamma 3P distribution was successfully obtained. The use of Gamma 3P distribution could be found in estimating particles separation at different purity criteria, as well as predicting diffusion of particles in the channel for other applications.

5.2 Simulation parameters and procedure

Direct Numerical Simulation (DNS) and Lagrangian Scalar Tracking (LST) of mass markers have been used in this research. We employed the pseudospectral DNS algorithm presented by Lyons (63) and validated with experiments by Gunther(64). All variables are made dimensionless using the friction velocity, u*, and the kinematic viscosity of the fluid, ν, namely, the *viscous wall units*. The computational box has dimension of 4πh x 2h x 2πh in the streamwise, x, normal, y, and spanwise, z, directions, respectively, with a half channel height (h) of 150. There are 128 x 129 x 128 grid points in x, y, and z directions. Periodic boundary conditions with lengths of 4πh and 2πh are applied to simulate an infinitely long channel in x and z directions, respectively. The flowing fluid is an incompressible Newtonian fluid with constant density and viscosity in a channel with no-slip and no-penetration boundary conditions imposed at the rigid channel walls.

Passive scalar markers that do not affect the flow field were released into the channel to represent mass particles. The tracking algorithm of Kontomaris(71) was used to track individual trajectories of these markers in space and time in a Lagrangian framework, in conjunction with the DNS. The combined DNS/LST approach has previously been used in study of heat transfer in high Prandtl or Schmidt number fluids (69, 139). Discussion about the accuracy of this method and comparisons of the results with experimental findings can also be found in previous publications (67, 70, 74, 75).

We release the mass markers into the flow field after the velocity field reaches a stationary state, based on DNS results. If $\vec{V}(\vec{x}_o, t)$ is the Lagrangian velocity of a

particle at location $\vec{x}_o$ at time t = t_o = 0, then the position $\vec{X}(\vec{x}_o, t)$ of the marker at time t is determined as

$$\vec{V}(\vec{x}_o, t) = \frac{\partial \vec{X}(\vec{x}_o, t)}{\partial t} \qquad (5.1)$$

At this point we assume that a marker at any time has the velocity of the fluid particle on which it rides, which means the relation between the Lagrangian velocity and the Eulerian velocity $\vec{U}$ is $\vec{V}(\vec{x}_o, t) = \vec{U}[\vec{X}(\vec{x}_o, t), t]$. Molecular diffusion effects that could make the mass markers move off a fluid particle have been represented by adding a random walk on the marker motion after each simulation time step. The value of the diffusion step is estimated by a Gaussian distribution in each space direction with a zero mean and a standard deviation, σ, depending on the Schmidt number, Sc, ($\sigma = \sqrt{2\Delta t/Sc}$) where Δt is the time step of the simulation. In this study, we examined several values of Sc (Sc = 6, 20, 50, 100, 200, 500, 1000, 2400) representing different substances. 10,000 markers, initially distributed uniformly on a line located at the bottom wall in the spanwise direction at x=0, were released instantaneously for each Sc. The simulation was performed twice, and results from two realizations were used for averaging purpose.

5.3 Results and discussion

5.3.1 Statistical Analysis

Lagrangian scalar tracking method was used to track the motion and record location of each marker. We then created small bins in the streamwise direction, and used the bin locations and number of markers in each bin to determine pdf values for

the particle distribution in the streamwise direction at different times. The pdf value at a bin located at x_i was calculated as in the equation below:

$$pdf(x_i) = \frac{n(x_i)}{N * binsize}$$

in which $n(x_i)$ is the number of particles in the bin centered at x_i, while N is the total number of particles (10,000). Due to different molecular diffusivities corresponding to different Sc, it was found that one shall not use the same bin size for all Sc, especially in the viscous wall region. Instead of that, for each Sc number, the bin size was chosen to be equal to $\sigma = \sqrt{2\Delta t/Sc}$, as listed in Table 5.1.

Table 5.1 Values of bin size for different Sc numbers

Sc	σ
6	0.18257
20	0.10000
50	0.06325
100	0.04472
200	0.03162
500	0.02000
1000	0.01414
2400	0.00913

We used the Kolmogorov-Smirnov (KS) statistical test, which quantifies the distance between the empirical distribution function of the sample and the cumulative distribution function of the reference distribution, to conduct goodness-of-fit test between different pdf models and our data. We tested 65 different common pdf models,

available in the EASYFIT software (version 5.6), with the KS test. The null hypothesis was as follows: “The empirical pdf follows the tested pdf model.” The level of significance, ε, was chosen to be 0.2. By choosing ε = 0.2, the acceptance of the null hypothesis is more rigorous than acceptance at the usual choice of ε = 0.05. Note that, in the KS test, the critical value of the KS statistic decreases when ε increases and that the null hypothesis is rejected when the critical value is smaller than that of the test statistic of a data sample. Thus, at a given value of the calculated test statistic, testing for the null hypothesis at a higher ε increases the probability of rejecting the null hypothesis. Such a high level of ε has been used to test null hypothesis in other published studies (140-142). Table 5.2 is a display of P values of different pdf models for different Sc as simulation time increases. The null hypothesis is rejected if the P-value is lower than the level of significance ε. The three pdf models listed in Table 5.2, including inverse Gaussian, three-parameter (3P) Gamma and three-parameter (3P) Weibull, are those that gave the highest P-values in the KS test. Comparing these three models, we found that the three-parameter Gamma distribution is the most appropriate one, not only because of its high P-values but also because its parameters closely relate to the development of a puff, as is explained in details in the next section.

Table 5.2 P-values obtained from 3 pdf models: a) Inverse Gaussian; b) 3P Gamma; c) 3P Weibull with different Sc numbers at different time. Empirical data from one simulation were used in this case to determine the most appropriate pdf model for use, as P-values do not vary much between different simulations

a)

t^+	6	20	50	100	200	500	1000	2400
10	0.007	0.006	1.000	0.002	0.000	1.000	0.009	1.000
15	0.995	1.000	1.000	1.000	1.000	1.000	1.000	1.000
20	1.000	1.000	0.999	1.000	1.000	1.000	1.000	1.000
25	0.999	1.000	0.997	0.991	0.997	1.000	1.000	0.999
30	0.989	0.975	0.953	0.892	0.994	0.977	0.980	0.965
35	0.773	0.853	0.752	0.000	0.989	0.908	0.904	0.852
40	0.737	0.582	0.724	0.800	0.985	0.803	0.708	0.799
45	0.593	0.480	0.742	0.763	0.941	0.770	0.666	0.837
50	0.480	0.418	0.749	0.771	0.928	0.581	0.493	0.671
55	0.277	0.485	0.704	0.550	0.816	0.628	0.431	0.595
60	0.113	0.449	0.420	0.458	0.569	0.492	0.381	0.404
65	0.071	0.467	0.428	0.405	0.422	0.474	0.392	0.462
70	0.029	0.428	0.432	0.374	0.376	0.476	0.439	0.468
75	0.021	0.403	0.285	0.384	0.246	0.368	0.356	0.440

80	0.016	0.430	0.337	0.427	0.150	0.313	0.342	0.296
85	0.005	0.615	0.358	0.437	0.124	0.208	0.281	0.259
90	0.002	0.642	0.236	0.312	0.108	0.146	0.149	0.153
95	0.000	0.553	0.213	0.218	0.140	0.090	0.095	0.077
100	0.000	0.687	0.219	0.174	0.174	0.046	0.128	0.053

b)

t^+	6	20	50	100	200	500	1000	2400
10	1.000	0.966	0.987	0.986	0.974	0.998	0.913	0.967
15	0.995	0.993	0.935	0.858	0.940	0.850	0.962	0.864
20	0.985	0.969	0.844	0.867	0.936	0.875	0.918	0.829
25	0.985	0.939	0.914	0.962	0.999	0.994	0.943	0.866
30	1.000	0.999	0.976	0.998	1.000	0.986	0.976	0.916
35	1.000	0.998	0.984	0.000	0.990	0.927	0.951	0.924
40	1.000	0.994	0.909	0.975	0.955	0.976	0.858	0.741
45	1.000	0.971	0.835	0.921	0.913	0.950	0.798	0.599
50	1.000	0.869	0.761	0.975	0.901	0.802	0.615	0.715
55	0.913	0.683	0.924	0.985	0.977	0.767	0.549	0.815
60	0.687	0.516	0.943	0.973	0.994	0.848	0.528	0.826
65	0.651	0.472	0.884	0.896	0.931	0.871	0.601	0.734
70	0.540	0.338	0.953	0.985	0.929	0.983	0.694	0.939
75	0.419	0.373	0.961	0.987	0.959	0.948	0.724	0.817
80	0.340	0.293	0.760	0.999	0.755	0.777	0.946	0.774

85	0.236	0.318	0.850	0.971	0.897	0.922	0.941	0.844
90	0.150	0.285	0.738	0.994	0.859	0.888	0.991	0.837
95	0.065	0.165	0.564	0.958	0.830	0.970	0.987	0.809
100	0.033	0.081	0.423	0.972	0.900	0.957	0.998	0.669

c)

t+	6	20	50	100	200	500	1000	2400
10	0.912	0.688	0.707	0.697	0.695	0.820	0.604	0.642
15	0.750	0.725	0.579	0.534	0.599	0.545	0.566	0.502
20	0.693	0.581	0.505	0.549	0.591	0.475	0.542	0.476
25	0.604	0.461	0.511	0.500	0.724	0.716	0.486	0.464
30	0.830	0.761	0.563	0.719	0.725	0.667	0.522	0.506
35	0.798	0.717	0.650	0.000	0.537	0.643	0.477	0.598
40	0.741	0.586	0.412	0.518	0.464	0.527	0.332	0.253
45	0.791	0.529	0.380	0.347	0.348	0.469	0.231	0.177
50	0.719	0.402	0.294	0.392	0.335	0.238	0.169	0.261
55	0.421	0.221	0.361	0.456	0.342	0.298	0.149	0.255
60	0.199	0.119	0.295	0.373	0.403	0.217	0.094	0.213
65	0.105	0.113	0.280	0.217	0.305	0.205	0.098	0.187
70	0.085	0.064	0.379	0.320	0.393	0.340	0.136	0.202
75	0.159	0.071	0.240	0.378	0.395	0.347	0.185	0.160

80	0.130	0.060	0.126	0.361	0.314	0.334	0.303	0.132
85	0.082	0.051	0.142	0.265	0.295	0.429	0.302	0.177
90	0.038	0.038	0.076	0.308	0.319	0.344	0.376	0.126
95	0.037	0.014	0.071	0.345	0.264	0.376	0.335	0.128
100	0.019	0.007	0.068	0.281	0.223	0.397	0.349	0.113

5.3.2 Three-parameter Gamma distribution

The probability density function f(x) and cumulative distribution function F(x) could be determined from three parameters of the Gamma distribution, namely α, β, and γ as shown below

$$f(x) = \frac{(x-\gamma)^{\alpha-1}}{\beta^{\alpha} * \Gamma(\alpha)} exp^{-\frac{x-\gamma}{\beta}} \qquad F(x) = \frac{\Gamma_{\frac{x-\gamma}{\beta}}(\alpha)}{\Gamma(\alpha)} \qquad (5.2)$$

The physical meaning of the three parameters is explained here first. The first two parameters, α and β, are continuous shape and scale parameters, respectively (α, β > 0). The 3rd parameter, γ, is a continuous location parameter, which is also the lower boundary of the data domain.

As γ represents the lower boundary of our data domain, it is supposed to take value based on the location of the slowest moving particle in a puff. The problem now becomes locating the bin location that contains the slowest moving particle in a puff as it travels with time (for simplicity, we call the location of the center of this bin X_{bmin}). From our experience, this bin usually contains only a few particles. Unfortunately, this makes its location to be a random variable that varies with each simulation. In order to solve this problem, we decided to remove the slowest 100 particles (equivalent to 1% of the population) from our calculations. The bin with the slower particles now contains

more than just a few particles, and it could actually represent the lower boundary of our data domain in a more meaningful way.

At this point, it is necessary to check if the third parameters of the Inverse Gaussian, 3P Gamma and 3P Weibull distributions actually take values of the X_{bmin} location. Our argument is that, as the third parameters of these pdf models represent the lower boundary of a domain, they should match well with the X_{bmin} location. This would also make our prediction of this third parameter more reasonable, as we could base on location of the slowest moving particles. In Figure **5.2**, we plot the 3rd parameters of these pdf models and X_{bmin} from one of our simulations, for a few Sc, and it appears that only the Gamma and Weibull distributions satisfy our requirement. Taken into account the P-values from KS test listed in Table 5.2, the three-parameter Gamma distribution was chosen as our pdf model for use in predicting concentration distribution of a puff released from the channel wall.

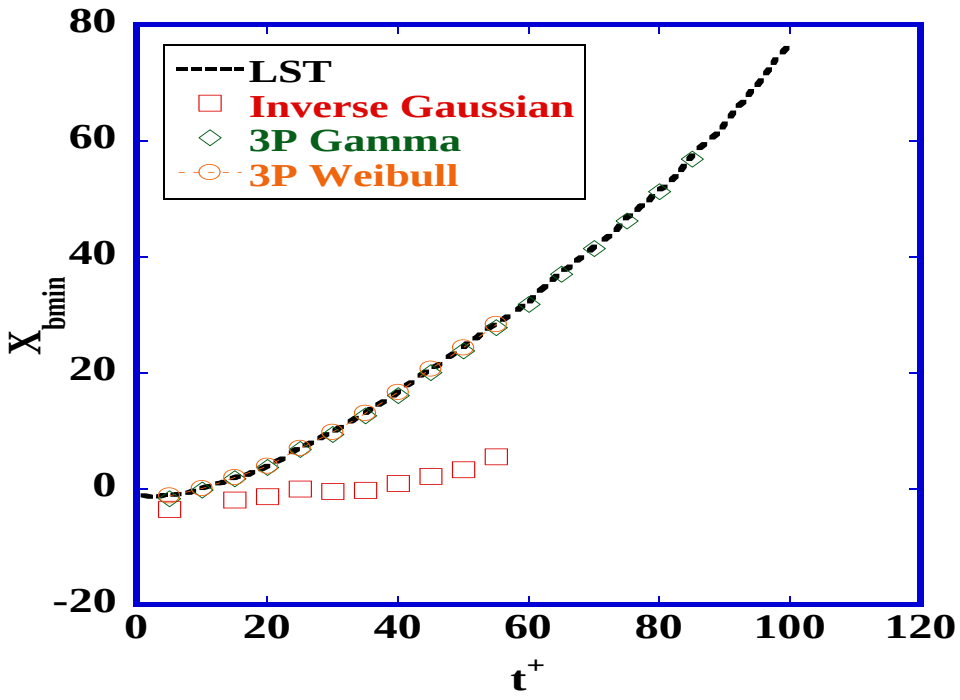
In this study, we try to predict three parameters of 3P Gamma distribution based on their relation to the shape and location of a puff. The following equations have proved to be useful in giving us an idea of how these three parameters could be determined by studying the puff development:

$$\mu - \gamma = \alpha * \beta \qquad (5.3)$$

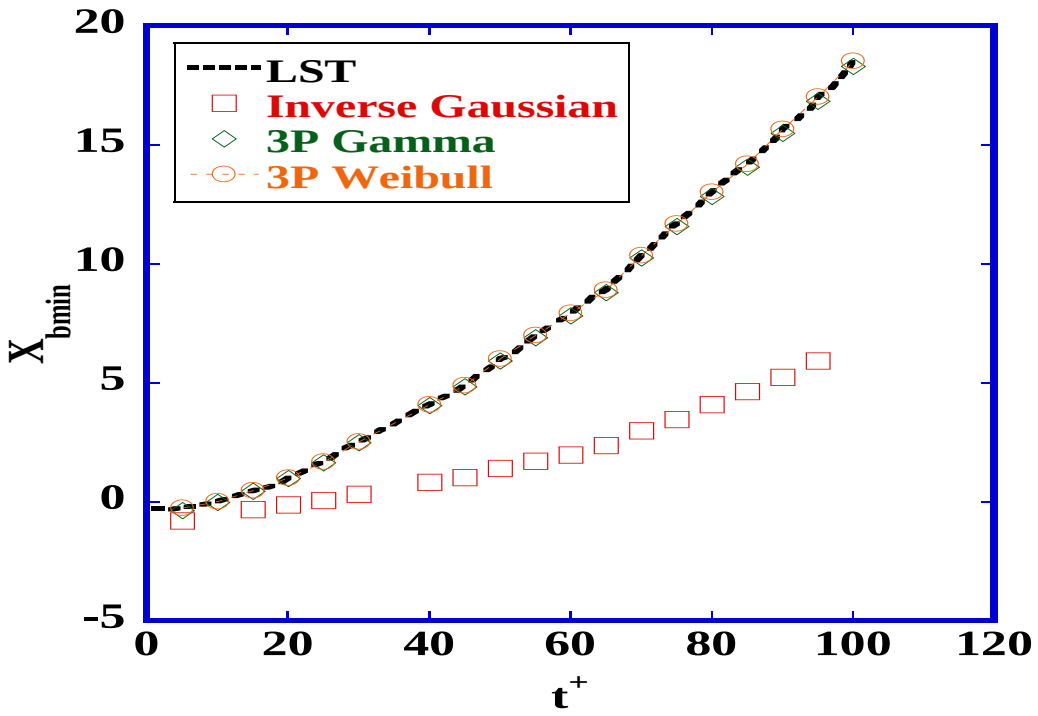
$$\mu - \beta = \text{mode} \qquad (5.4)$$

in which μ is the mean streamwise displacement of the puff, and mode is a location where there are most particles at, which is the location of a peak in the pdf. Note that, equations (3) and (4) are correct for α, β and γ provided by EasyFit for 3P Gamma distribution.

a)


LST
Inverse Gaussian
3P Gamma
3P Weibull
X_{bmin}
t^+
80
60
40
20
0
-20
0
20
40
60
80
100
120

b)


LST
Inverse Gaussian
3P Gamma
3P Weibull
χ_{bmin}
t^+
20
15
10
5
0
-5
0
20
40
60
80
100
120

c)

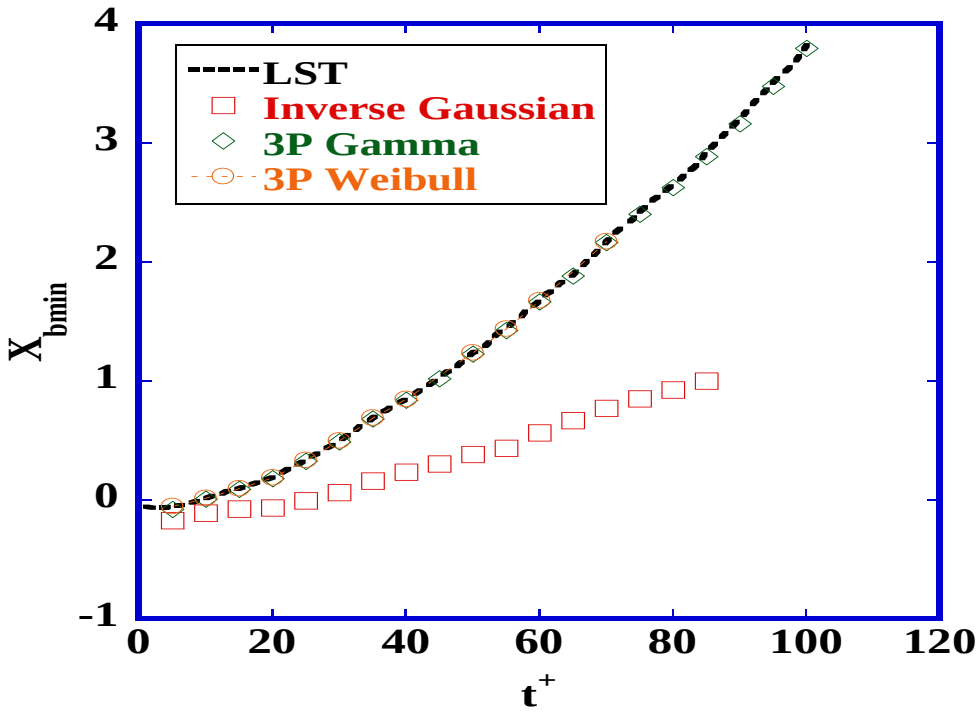


Figure 5.2 Plotting of Xbmin and 3rd parameters from Inverse Gaussian, 3P Gamma and 3P Weibull distribution for one simulation. a) Sc = 6; b) Sc = 100; c) Sc = 2400

Some background in particles dispersion are presented here again as that would be helpful for the rest of this study. Einstein (40) developed a relation that describes dispersion of particles in term of the mean-squared displacement from the source in the streamwise direction:

$$\frac{d\overline{X^2}}{dt} = 2D \qquad (5.5)$$

where D is the molecular diffusivity. Taylor (41) developed a similar relation for the rate of dispersion of fluid particles from a point source in homogeneous, isotropic turbulence:

$$\frac{d\overline{X^2}}{dt} = 2\overline{u^2}\int_0^t R^L(\tau)d\tau \qquad (5.6)$$

where $\overline{u^2}$ is the mean-square of the x-component of the velocity of fluid particles and R^L is the Lagrangian correlation coefficient. An important implication of Taylor's equation is that the history of the particle motion affects the rate of dispersion through R^L. At small times, the Lagrangian correlation coefficient is close to one, making the dispersion increases with time to the second power. At large times $R^L = 0$, and thus the dispersion changes linearly with time.

Dispersion of heat or mass markers introduces an additional complication, as they could move off a fluid particle as a result of molecular diffusion. A relation for dispersion in this case was developed by Saffman (42), using a material autocorrelation function, which correlates fluid velocity components along the trajectories of markers instead of fluid particles. Corrsin (43) studied line source diffusion in a homogeneous shear flow with a constant mean velocity gradient. The Lagrangian dispersion in the direction of the flow, X, was found to be different from the dispersion in the direction of the velocity gradient, Y, which is described by Taylor's analysis. It is

$$Y = \int_0^t v(t_1)dt_1 \qquad (5.7a)$$

$$X = \int_0^t [\frac{d\overline{U}}{dy} Y(t_1) + u(t_1)]dt_1 \qquad (5.7b)$$

where u and v are the particle velocities in the direction of the flow and in the direction of the velocity gradient, respectively. For large times the dispersion becomes

$$\overline{Y^2} = 2\overline{v^2}\tau_y^L t \qquad (5.8a)$$

$$\overline{X^2} = \frac{2}{3}(\frac{d\overline{U}}{dy})^2 \overline{v^2}\tau_y^L t^3 \qquad (5.8b)$$

where τ_y^L is the Lagrangian timescale in the y-direction. Equation (5.8b) suggests that at large time, the first order mean streamwise displacement X could be a function of $t^{3/2}$. In

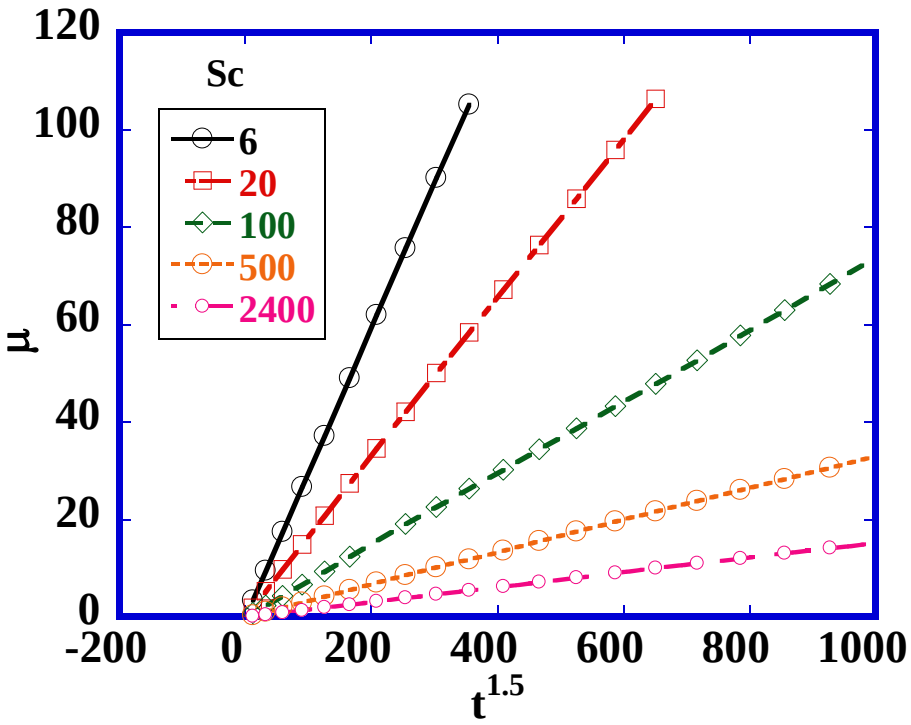
another study of turbulent dispersion in inhomogeneous and anisotropic turbulence, Papavassiliou (75) also found that for Sc between 0.7 and 50,000 , the mean streamwise displacement X is proportional to $t^{3/2}$ for time up to the end of Zone 1. Thus, we make an assumption that the μ in Equation (3) and (4) could be described as a linear function of $t^{3/2}$: $\mu = g*t^{3/2}$. This assumption proves to be correct as we plot μ versus $t^{3/2}$ for different Sc in Figure **5.3**a (note that only a few Sc are plotted for example). The coefficient g varies for each Sc, however, it was found to be a function of $Sc^{-0.5}$ as seen in Figure **5.3**b. Note that all results were obtained by taking average of 2 different realizations. The mean particle position at this point could be expressed as follows

$$\mu = 0.73 * Sc^{-0.5} * t^{1.5} \qquad (5.9)$$

As we are interested in development of a puff at short time, it is reasonable to assume that the mode also moves at similar rate to μ. Under this assumption, we also plotted the mode versus $t^{1.5}$ for different Sc in Figure **5.4**a. It appears that the mode could also be described as a linear function of $t^{3/2}$, with a coefficient k depending on Sc, as seen in Figure **5.4**b. The mode position is now calculated as in Eq. (5.10).

$$\text{Mode} = 0.39 * Sc^{-0.5} * t^{1.5} \qquad (5.10)$$

a)



b)

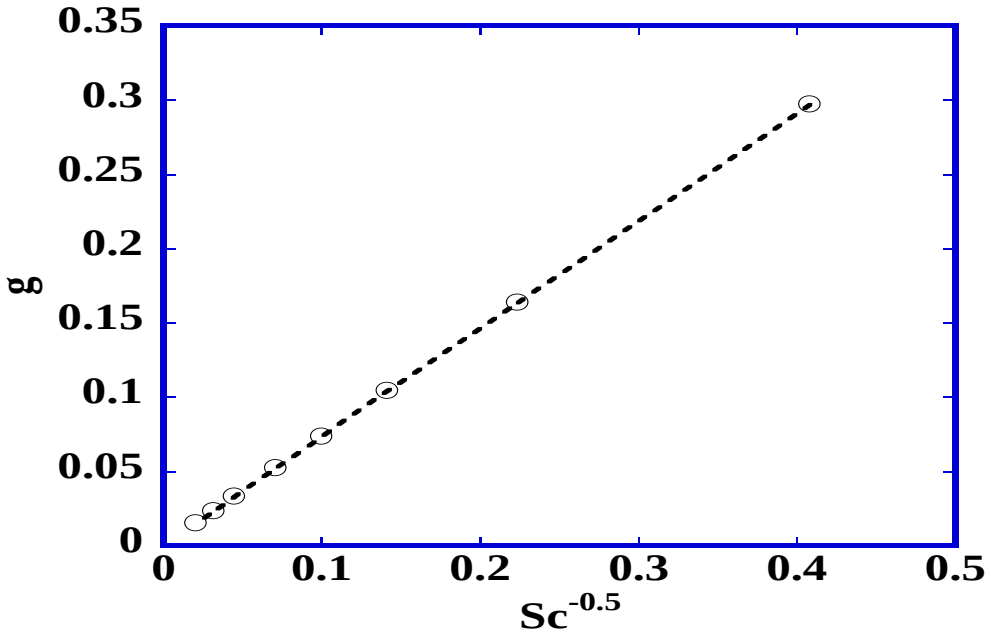
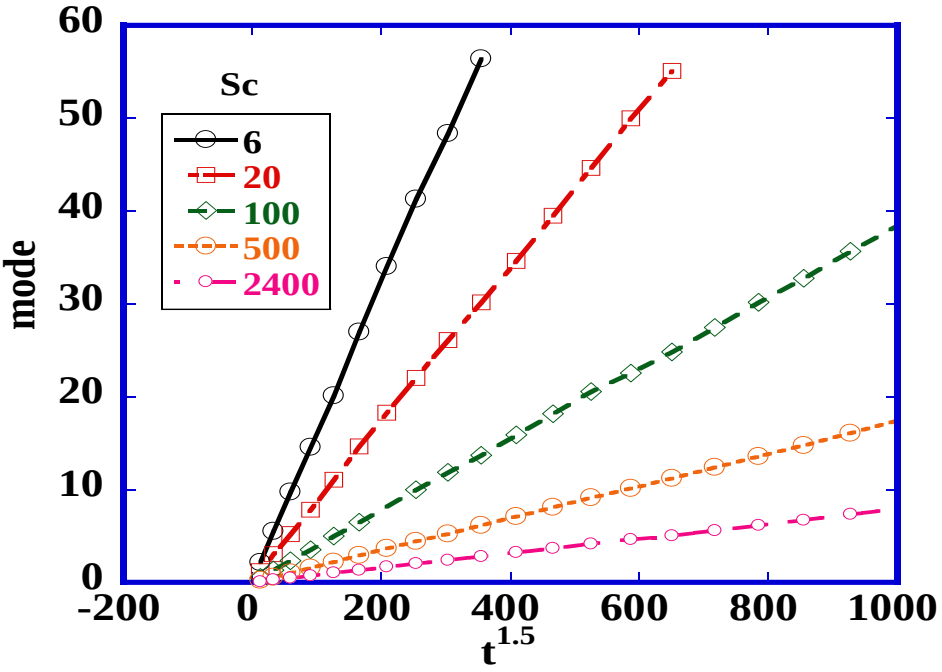


Figure 5.3 a) Plotting of Mean streamwise displacement versus $t^{1.5}$ for different Sc numbers. b) The coefficient g was found to be a function of $Sc^{-0.5}$

a)



b)

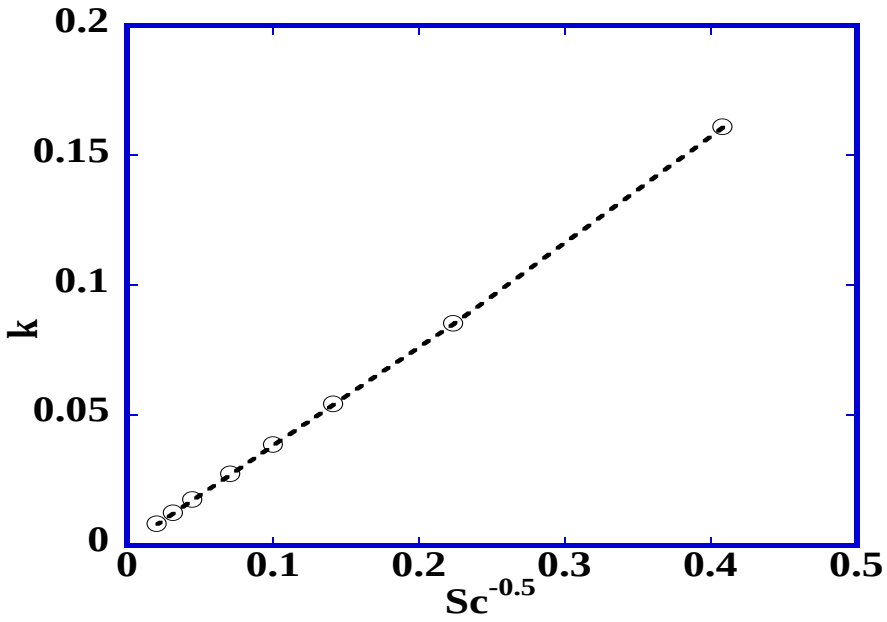


Figure 5.4 (a) Plotting of mode values versus $t^{1.5}$ for different Sc numbers. (b) The coefficient k was found to be a function of $Sc^{-0.5}$

At this stage, we need to determine value of γ by calculating X_{bmin} in order to solve equations (5.3) and (5.4). Note that at early time, some particles in this bin could travel into the negative streamwise direction due to effect of molecular motion in the viscous sub region. As this only happens at short times and does not affect much on our applications, we would focus on time larger than 10 only, which is the time that X_{bmin} starts taking positive values and keeps increasing.

Based on Taylor's analysis, the mean square displacement in x-direction increases with time to the second power at small times. How long this relation lasts could be determined by using the material timescale τ_y^L. Le (65) calculated and found that for particles with Sc between 0.1 and 50000, being released at a vertical location less than 1 viscous plus unit away from the wall, the material timescale τ_y^L is less than 5. As we are interested at time larger than 10, it could be expected that X_{bmin} increases with $t^{3/2}$ as in equation (5.8b). Being scaled with $Sc^{-0.5}$ to represent effect of molecular diffusion, equation (5.11) successfully captures X_{bmin}, whose values would be assigned to γ. Note that X_{bmin} values were taken as average from two different simulations, and comparison between simulation data and model in equation (5.11) is plotted in Figure **5.5**.

$$X_{bmin} * Sc^{1/2} = (0.186 * t^{3/2} - 8) \qquad 10 < t < 100 \qquad (5.11)$$

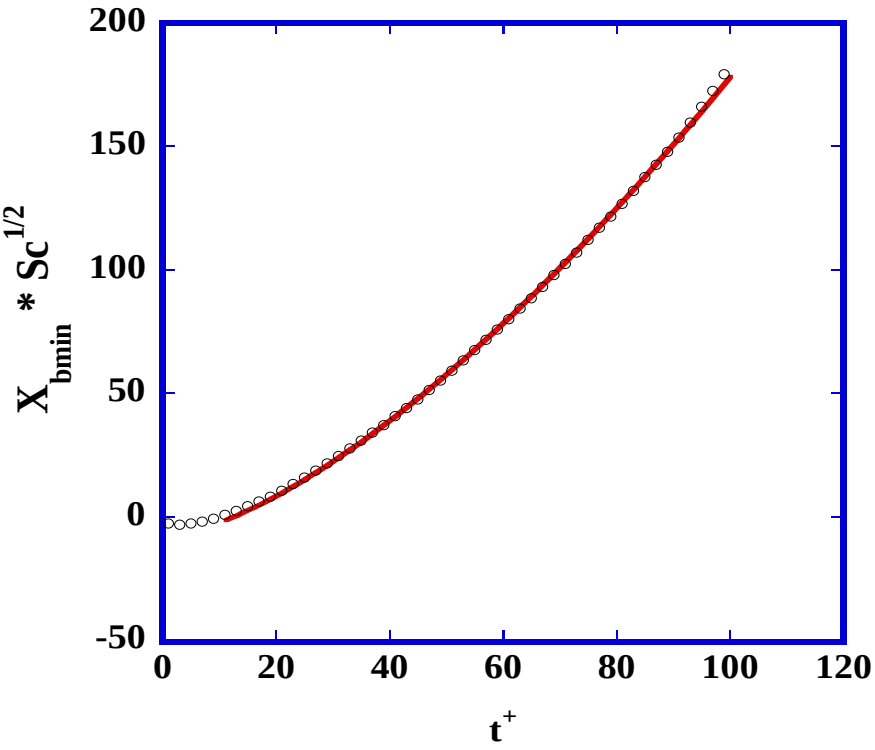


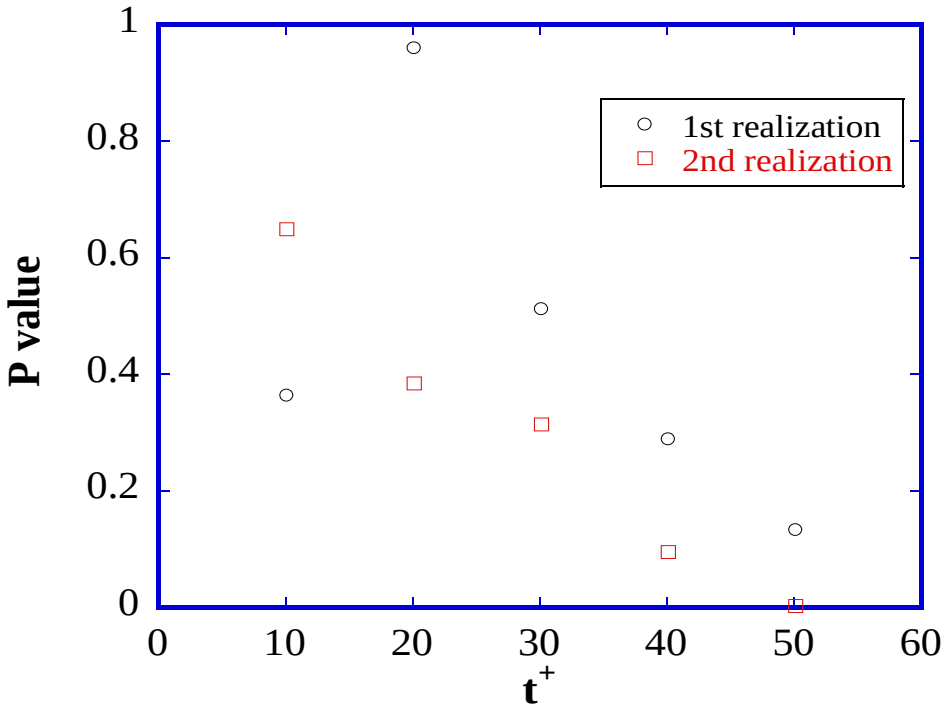
Figure 5.5 Scaling of X_{bmin} with $Sc^{1/2}$ for different Sc at different times. Results were taken average from 2 different simulations. o : simulation results; – : line obtained from equation (5.11)

5.3.3 Model Testing

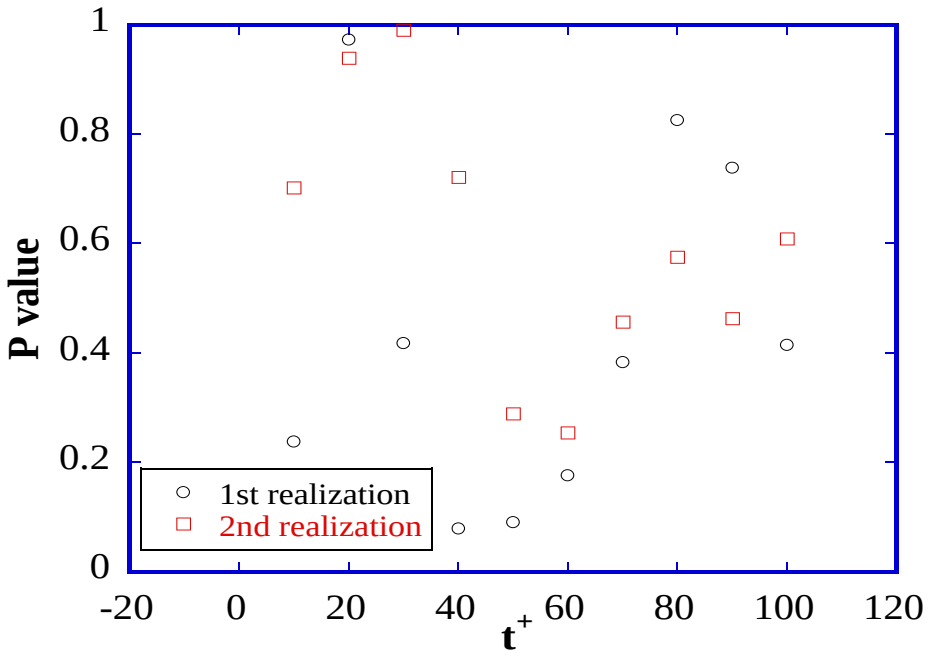
The Gamma 3P distribution was found as the most appropriate pdf model to describe the particle pdf in the streamwise direction. All the calculations above were obtained using average data from 2 simulations. Before applying the Gamma 3P distribution in other applications, we would like to test how well the calculated parameters perform in the goodness-of-fit test, using again the empirical distribution from 2 simulations. Using appropriate equations, we could calculate 3 parameters for each Sc number at corresponding time. We then used these parameters for 3P Gamma distribution on EasyFit and performed goodness-of-fit test. The results have been encouraging as seen in Figure **5.6**, with results from Sc = 6, 200 and 1000 presented as

examples. One can see that in most cases, the P-values are higher than 0.2. It can also be seen that there are some P-values smaller than 0.2; which means the null hypothesis would be rejected at significance level $\varepsilon = 0.2$. In order to determine how big the error is in case the null hypothesis gets rejected, we measure and report herein the difference in cumulative distribution function (CDF) between the empirical data from two simulations and results predicted by using 3P Gamma distribution. Three examples with Sc = 6, 200 and 1000 are presented in Figure **5.7**. Note that for each Sc, we measured the CDF errors at two different times: one at high P-values, and one at low P-values. By doing that, we could estimate the minimum and maximum CDF errors encountered by using the proposed pdf model. As one can see, the maximum CDF error was roughly 5%, which gave us more confidence in applying this pdf model in other applications.

a)



b)



c)

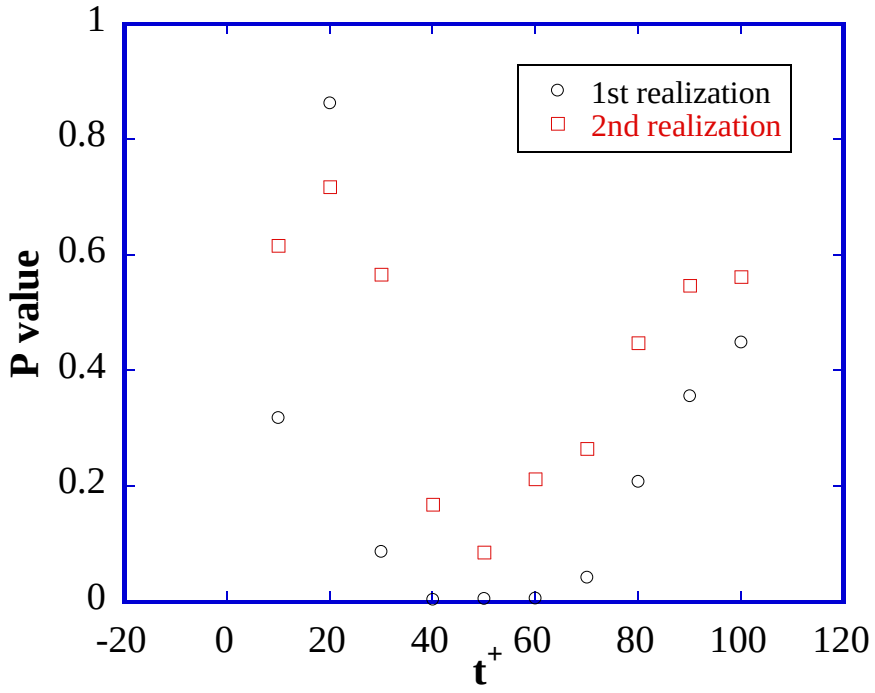
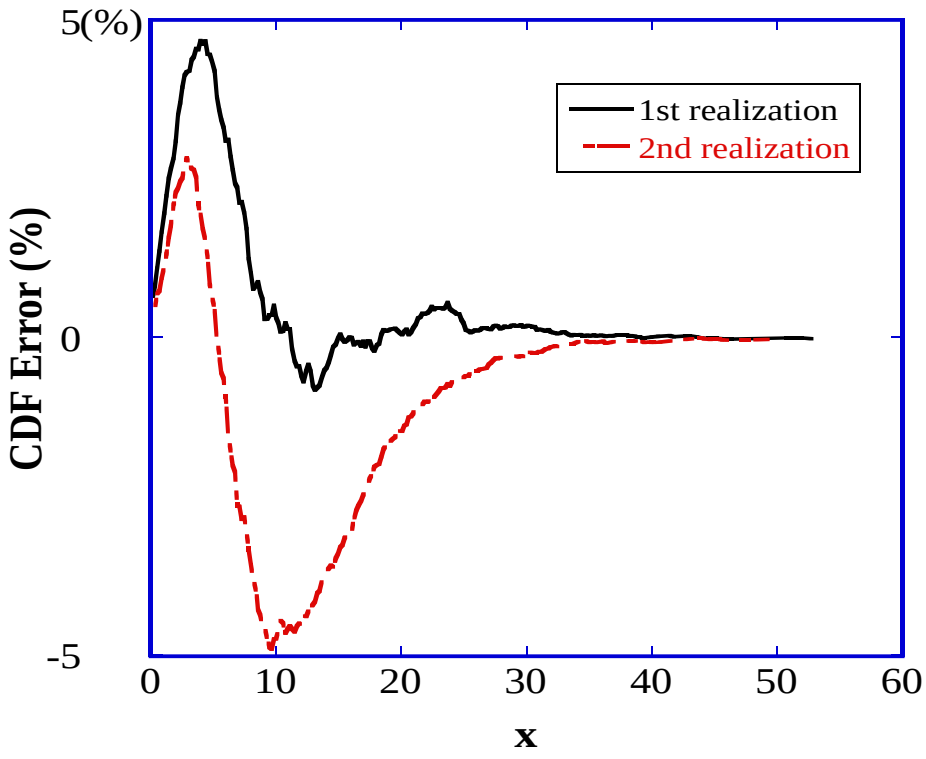
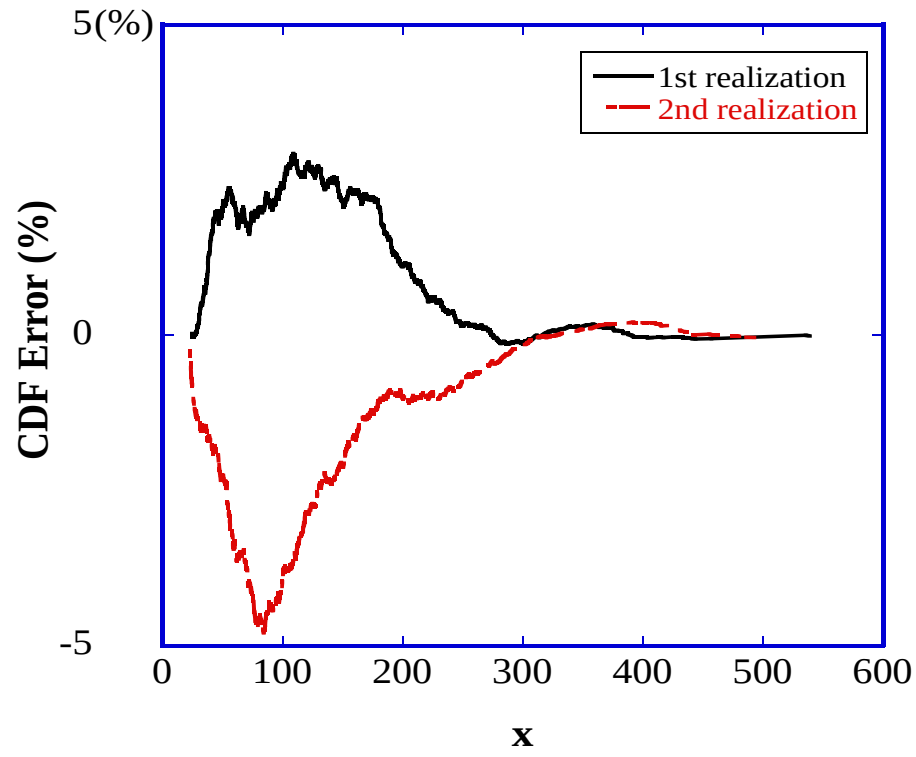


Figure 5.6 P-value obtained from goodness-of-fit test by using our pdf model and empirical data from 2 realizations; a) Sc = 6; b) Sc = 200; c) Sc = 1000

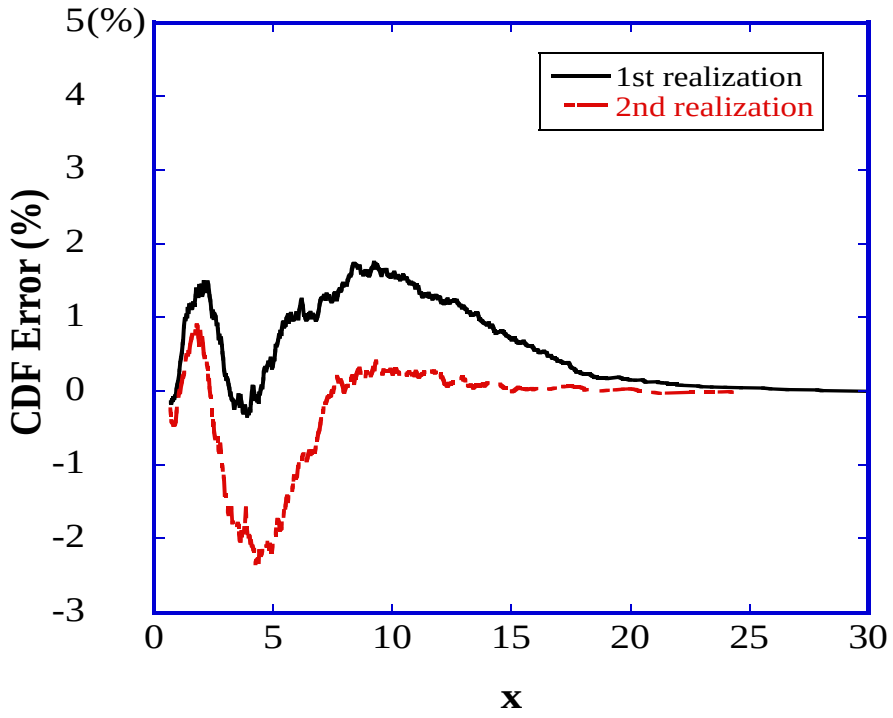
a)


5(%)
0
-5
CDF Error (%)
0
10
20
30
40
50
60
x
1st realization
2nd realization

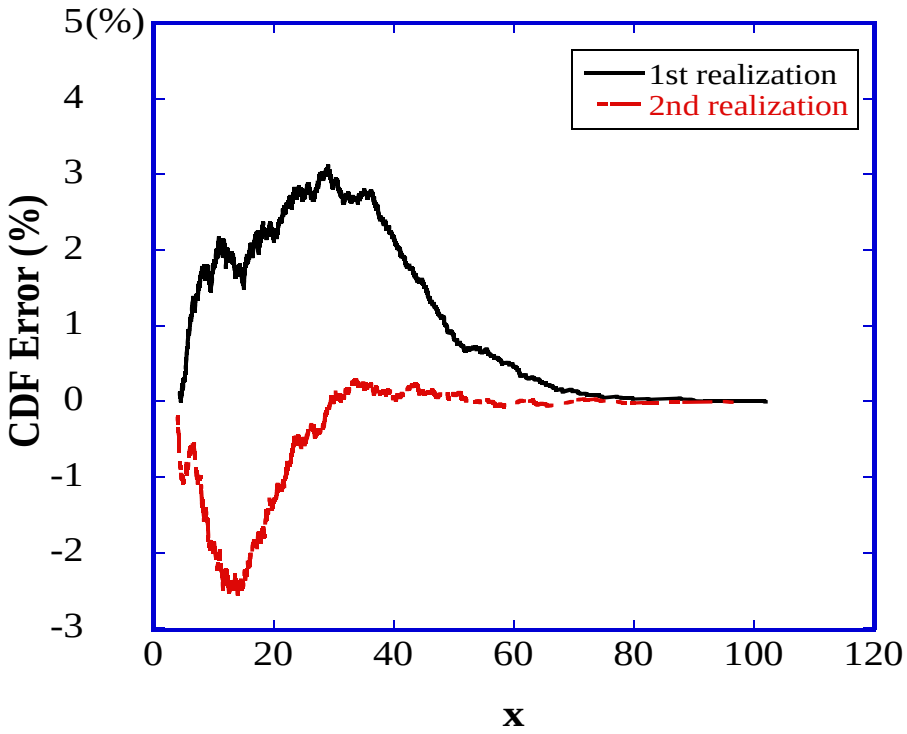
b)


5(%)
0
-5
CDF Error (%)
0
100
200
300
400
500
600
x
1st realization
2nd realization

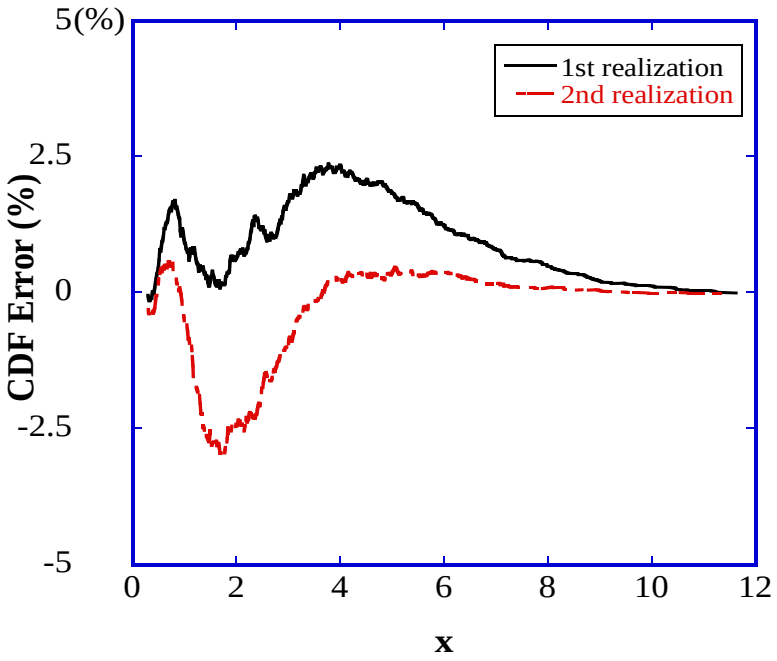
c)


5(%)
4
3
2
1
0
-1
-2
-3
CDF Error (%)
0
5
10
15
20
25
30
x
1st realization
2nd realization

d)


5(%)
4
3
2
1
0
-1
-2
-3
CDF Error (%)
0
20
40
60
80
100
120
x
1st realization
2nd realization

e)



f)

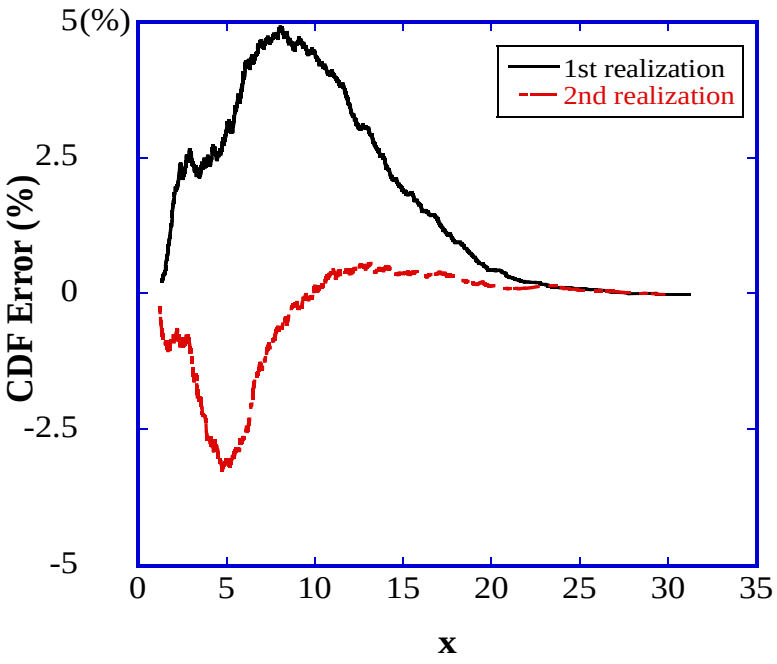


Figure 5.7 CDF error between using our pdf model and empirical data from 2 realizations for different Sc number. a) Sc = 6 at t^+ = 10; b) Sc = 6 at t^+ = 50; c) Sc = 200 at t^+ = 20; d) Sc = 200 at t^+= 50; e) Sc = 1000 at t^+ = 20; f) Sc = 1000 at t^+= 40

5.3.4 Application of the Gamma 3P distribution model

As mentioned earlier, particle separation in turbulent channel flow is one application where we could apply the Gamma 3P distribution. By plotting pdf of puffs with different Sc at different times, one can predict if the two puffs, released from a channel wall, would separate from each other or not. The idea is briefly presented in Figure **5.8**, where we plot pdf values of 2 puffs with Sc 50 and 2400, multiplied by corresponding bin sizes of each Sc, at $t^+ = 50$. As particles with Sc = 50 have larger molecular diffusivity, they would move faster and form the leading puff, while particles with Sc = 2400 are left behind and form the following puff. One can see that there exists an "overlap" region, ranging from the tail of the leading puff to the head of the following puff. The number of particles of each puff in this overlap region could be calculated to quantify separation ability.

We now apply the Gamma 3P distribution in predicting separation with different pairs of Sc number particles and compare with results obtained from the DNS-LST method. We report herein number of particles from both the leading and following puffs in the overlap region for every pair of Sc numbers. These results were obtained from 3 different simulations at $Re_\tau = 150$ and with using Gamma 3P distribution model.

The first pair of Sc to be tested is 6 and 2400, with number of particles from 2 puffs in the overlap region plotted in Figure **5.9**. We notice that the Gamma 3P distribution model predicts less particles from both the leading and following puffs in the overlap area, compared to results from 3 realizations. This could be explained due to the fact that we removed the slowest 1% particles from the tail of the leading puff, thus leading to a narrower overlap region. As the following puff is quite compact, this results

in a significant drop of the number of particles of this puff in the overlap area, as seen in Figure 5.9b. This effect, though, is less pronounced when we look at number of particles of the leading puff in the overlap region. In this specific case, one can add up to 100 particles of Sc = 6 into the overlap region. From our experience, separation usually happens when the number of particles of the leading puff in the overlap is small enough. This could be seen in Figure **5.9**, as the following puff has a lot more particles in the overlap, compared to the leading puff. Because of that, removing the slowest 1% particles from the tail of the leading puff does not affect much the separation prediction. Moreover, one may see that the 3 realizations have certain degree of random, uncertainty when we compare the results. Our pdf model, on the other hand, tends to provide average results from those 3 realizations, despite the fact that results from the 3rd realization were not used in developing this pdf model.

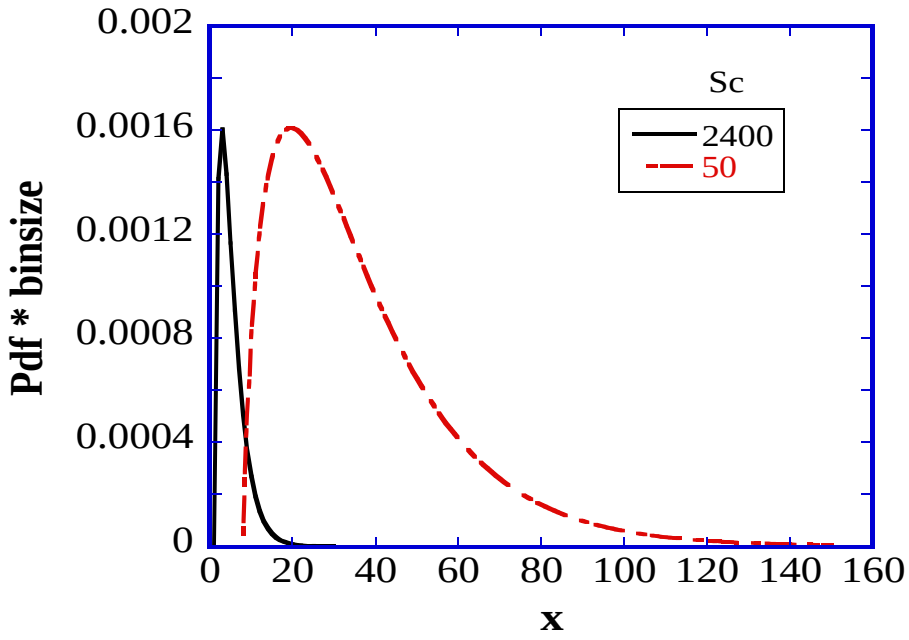
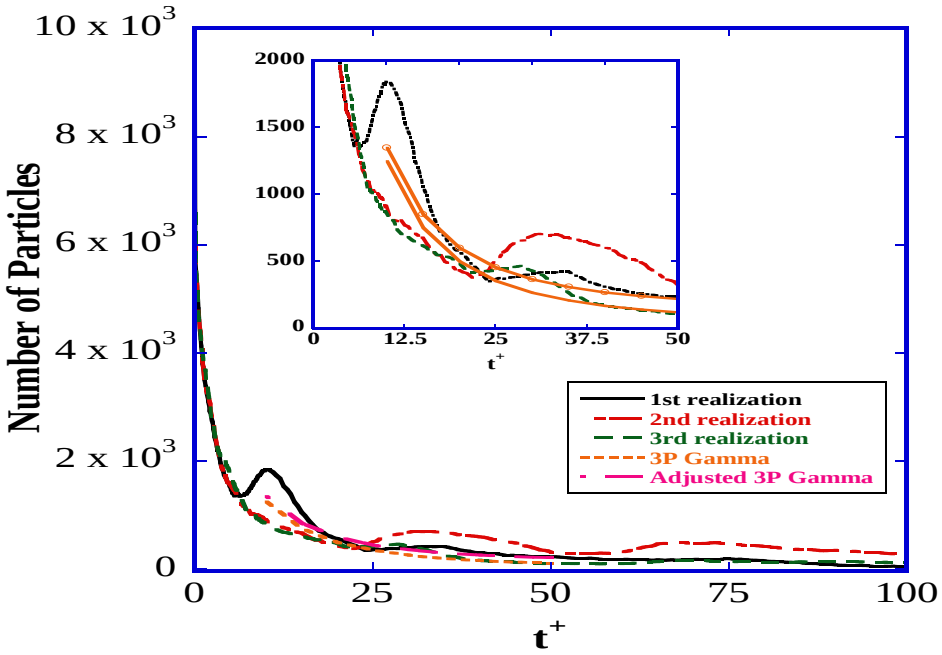


Figure 5.8 PDF of 2 puffs of particles with Sc 50 and 2400 at t+=50. Overlap area was clearly observed in this case, which implies that complete separation could not happen

a)



b)

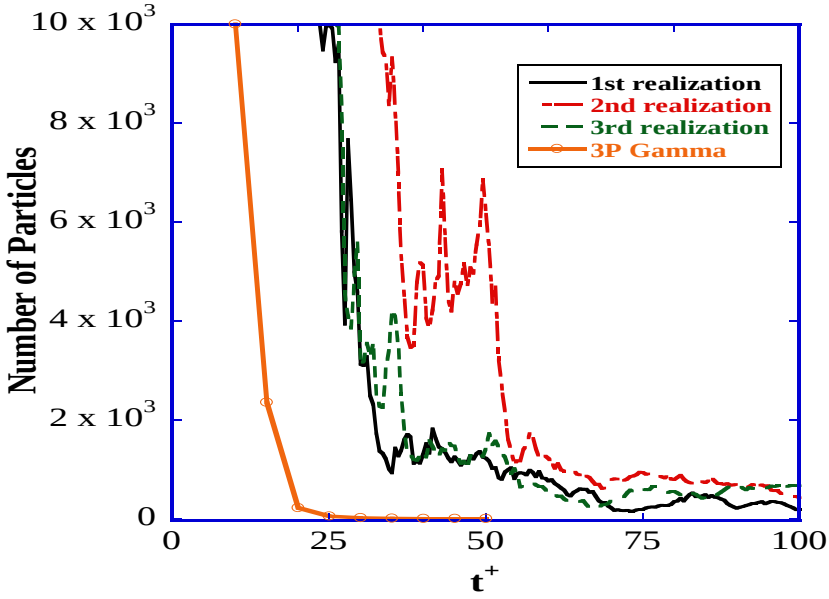
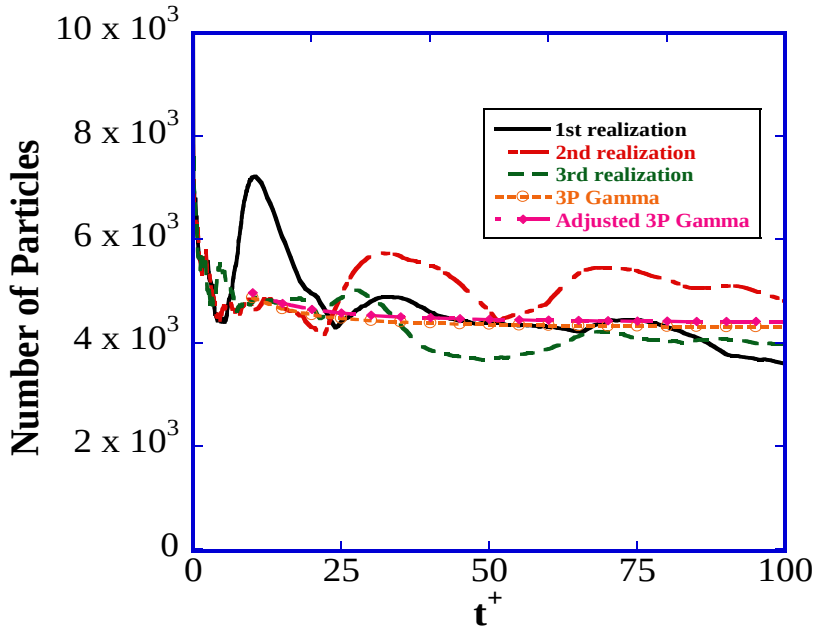


Figure 5.9 Use of Gamma 3P distribution to calculate number of particles in the overlap region and compare with results from DNS-LST method, pair of Sc numbers 6 and 2400; a) number of particles of the leading puff; b) number of particles of the following puff. The Adjusted 3P Gamma line adds 100 more particles to the number of particles of the leading puff in the overlap region.

Another example with pair of Sc numbers 50 and 2400 is also presented here. As predicted in our previous study (136), separation with 99.5% purity criteria, which means that less than 0.5% of population of either a leading puff or following one is present in the overlap region, cannot happen in this case. However, separation of the two puffs at a certain level still happens, as we can see in Figure **5.10**. It is interesting to see that our pdf model agrees well with 3 realizations, in terms of number of particles of Sc = 50 in the overlap region. As in the previous case, Gamma 3P underestimates how many particles of Sc = 2400 (the following puff) there are in the overlap region, compared to 3 realizations.

Even though the Sc numbers used in this study are limited up to 2400, we believe it would be of great convenience if this pdf model could be extrapolated to higher Sc numbers, for t^+ up to 100. Theoretically, within this time range, particles with Sc numbers higher than 2400 still stay in their zone 1, thus we could expect our pdf model to work with these Sc numbers. We applied the Gamma 3P distribution model to predict separation between two puffs of Sc 6 and 7500. The results are plotted in Figure **5.11**, where it is seen that our pdf model and 3 realizations give the same conclusion that these 2 puffs could be almost separated from each other.

a)



b)

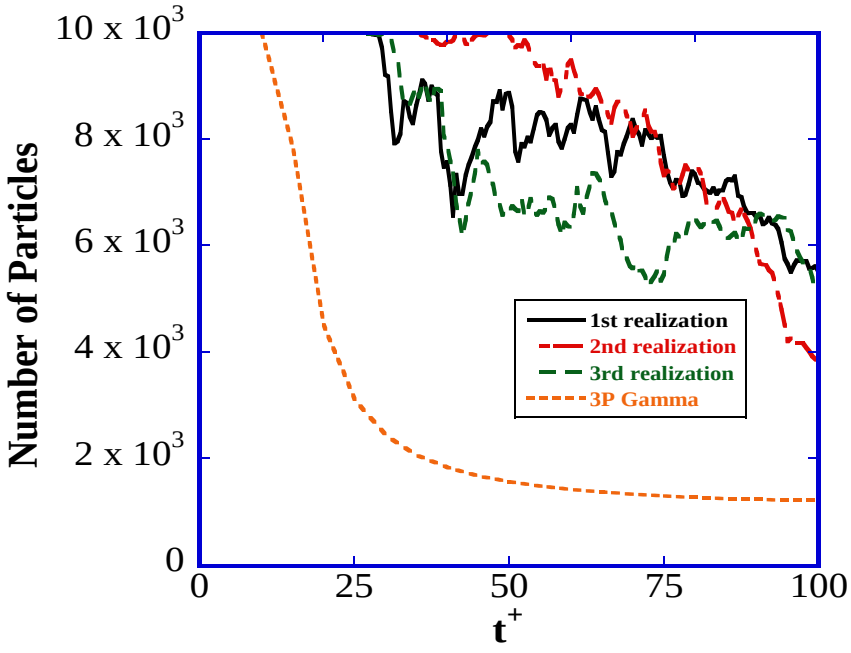
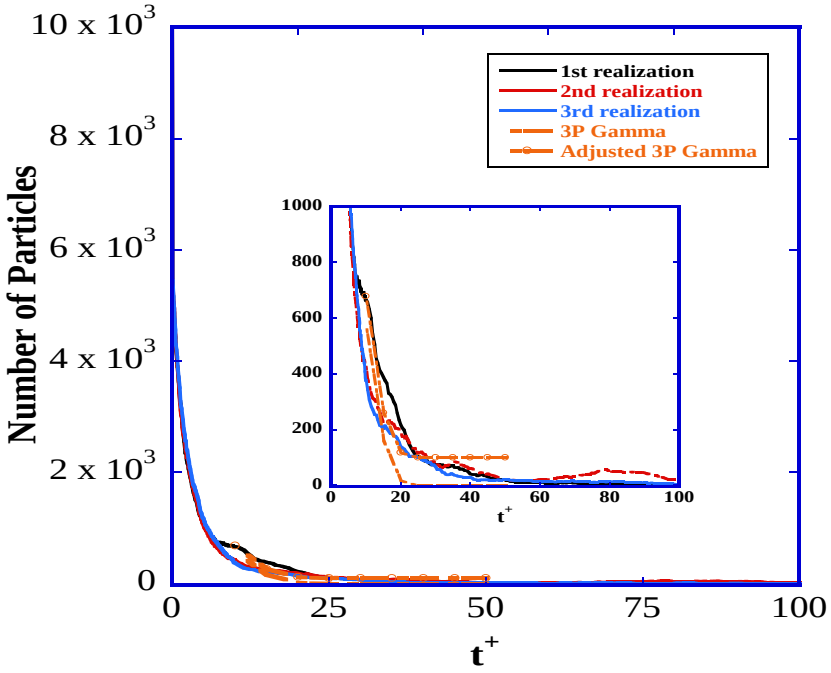


Figure 5.10 Use of Gamma 3P distribution to calculate number of particles in the overlap region and compare with results from DNS-LST method, pair of Sc numbers 50 and 2400; a) number of particles of the leading puff; b) number of particles of the

following puff. The Adjusted 3P Gamma line adds 100 more particles to the number of particles of the leading puff in the overlap region.

a)



b)

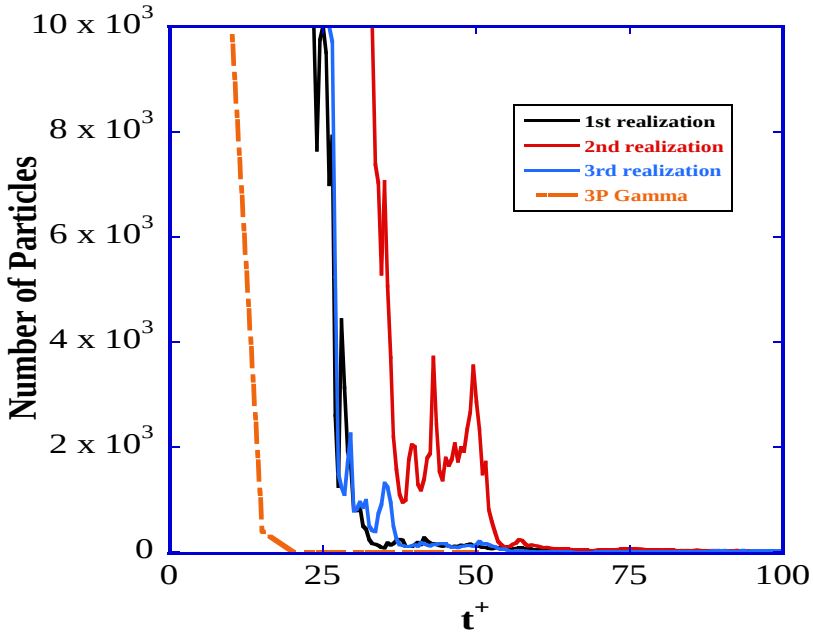


Figure 5.11 Use of Gamma 3P distribution to calculate number of particles in the overlap region and compare with results from DNS-LST method, pair of Sc numbers 6 and 7500; a) number of particles of the leading puff; b) number of particles of the

following puff. The Adjusted 3P Gamma line adds 100 more particles to the number of particles of the leading puff in the overlap region.

Chapter 6. Turbulent-Laminar Patterns in Poiseuille-Couette flow

6.1 Introduction

The coexistence of turbulent and laminar bands in wall-bounded shear flows at transitional regime has been observed and studied recently by several researchers. These bands are defined as essentially steady, spatially periodic pattern of distinct regions of turbulent and laminar flow emerges spontaneously from uniform turbulence near transition. They could be identified with large wavelength and an oblique angle they form to the streamwise direction. These patterns have been observed and verified in recent studies, including experiments on plane Couette flow and couter-rotating Taylor-Couette flow (45, 46), and in numerical simulations of plane Couette flow (52-54) and plane Poiseuille flow (55).

The results from above studies, though confirm existence of such patterns at transitional regime, also reveal that those patterns occur at quite different range of Reynolds number in plane Couette flow and plane Poiseuille flow. In plane Couette flow, the periodic regime in which laminar and turbulent regions are permanent occurs at $310 < Re < 390$ (52, 54). However, in plane Poiseuille flow, Tsukahara (55) found that the turbulent-laminar patterns exist at $Re \approx 1400$. This could be explained due to higher turbulent intensity and shear rate in plane Couette flow. However, this prevails some problems in reality, as fluidic devices generally contain more than one type of flows. A ventricular assist device (VAD) shown in Figure **6.1** is a great example of this

case, in which pipe flow and couter-rotating Taylor-Couette flow happen at the same time, and the volumetric flow rate is unchanged throughout the device.

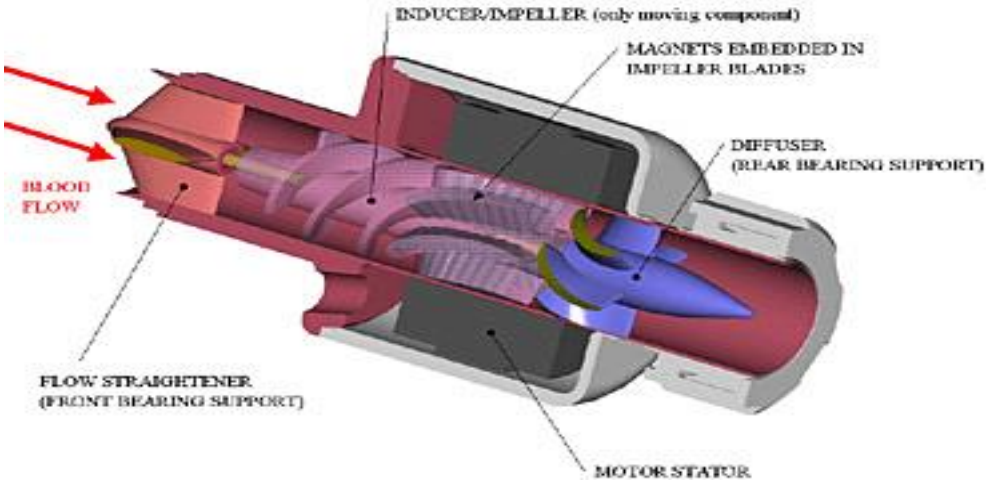


Figure 6.1 A Ventricular Assist Device (VAD) prototype

In this study, transition from plane Couette flow to plane Poiseuille flow at the same Reynolds number is examined. The objective is to study the difference in behavior of the turbulent-laminar patterns in plane Couette and plane Poiseuille flow, especially during the transition from Couette flow to Poiseuille flow. This research, though in its preliminary state, helps shed some light on understanding of these patterns during transition from one type of flow to another one.

6.2 Simulation parameters and procedure

In this study, we performed direct numerical simulation of a turbulent plane Couette flow and turbulent plane Poiseuille-Couette flow to investigate behavior of turbulent-laminar patterns as the flow goes from Couette to Poiseuille type. The flow was simulated in two computational boxes of sizes $30\pi h$ x $2h$ x $3\pi h$ with h = 80 and $100\pi h$ x $2h$ x $12\pi h$ with h = 24 in x, y and z directions, respectively (h is half of the

channel-height and is made dimensionless with the viscous length scale that is based on the kinematic viscosity of the fluid and the friction velocity, $u_\tau = \sqrt{\frac{\tau_w}{\rho}}$, where τ_w is the shear stress at the wall and ρ is the density of the fluid).

The flow was assumed to be periodic in the streamwise, *x*, and spanwise, *z*, directions with lengths of periodicity equal to the box size in those two directions. Plane Couette flow of an incompressible and Newtonian fluid was simulated at two frictional Reynolds numbers of 24 and 80, corresponding to two Reynolds numbers of 323 and 1247, based on half of the channel height and the wall velocity. For simplicity, both of two computational boxes had a resolution of 512 x 129 x 128 in *x, y, z* directions. A uniform mesh was used in *x* and *z*, while a non-uniform mesh based on Chebyshev collocation points was used in the *y* direction (63).

In this simulation, the Navier-Stokes equations were resolved and integrated in time by using a pseudo-spectral fractional step method mentioned above (63). This algorithm has been validated in simulating plane Poiseuille flow and plane Couette flow through comparisons with laboratory measurements and other DNS results at similar conditions (63, 64, 66).

In order to study difference in behavior of turbulent-laminar patterns in Couette flow and Poiseuille flow and how that happens, Poiseuille-Couette flow was simulated as a transition from plane Couette flow to plane Poiseuille flow at the same Reynolds number. Starting from a plane Couette flow in stationary state, the wall velocities were slightly reduced along with adding of pressure drop into the flow. This decreases Couette effect and increases Poiseuille effect, and the flow now becomes Poiseuille-Couette flow. If this procedure is repeated for enough times, the flow would become

plane Poiseuille flow eventually. The turbulent-laminar patterns are examined throughout the process to study co-effect of Couette flow and Poiseuille flow on these patterns.

In order to keep the plane Couette flow and plane Poiseuille flow at the same Reynolds number, we control the wall velocity U_w in the Couette flow and the mean centerline velocity U_c in the Poiseuille flow and keep $U_w = U_c$. The half channel height h is kept unchanged in each case, being either 24 or 80 in viscous wall units. As the wall velocity U_w in the Couette flow was reduced and pressure drop was added, the mean centerline velocity is different than zero. We denote the wall velocity and centerline velocity in the plane Poiseuille-Couette flow as U_w' and U_c', with a constraint that $U_w = U_c = U_w' + U_c'$. A parameter $R = U_c'/U_w$ is used to represent existence of Couette and Poiseuille flow in the system, with R = 0 represents plane Couette and R = 1 represents plane Poiseuille, while any value of R between $0 < R < 1$ represents plane Poiseuille-Couette flow.

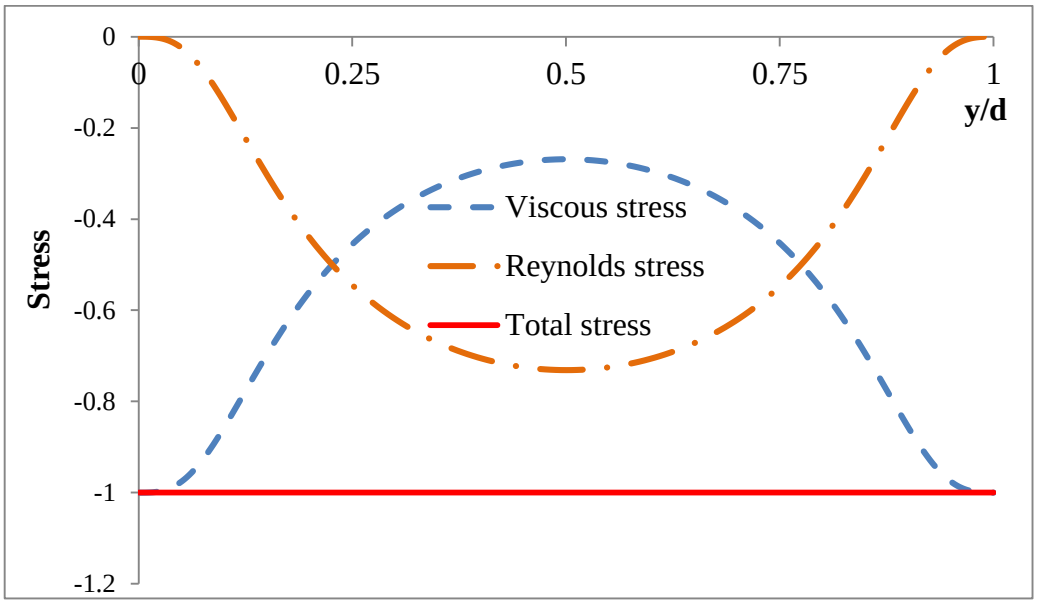
6.3 Results and discussion

6.3.1 Results at Re = 323 (Re_τ = 24)

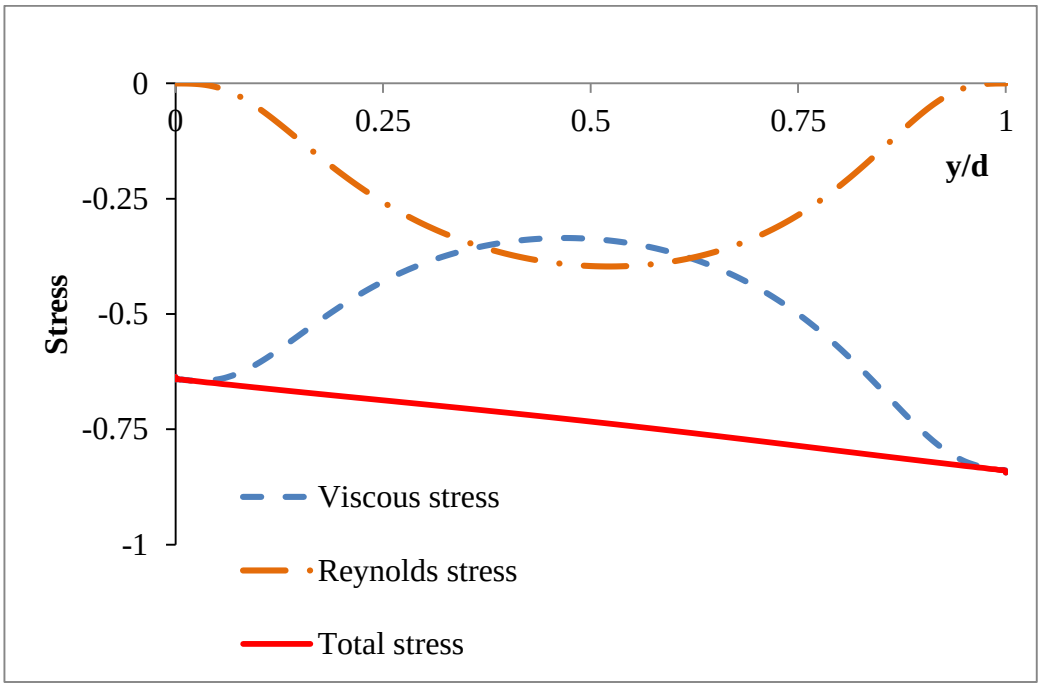
Simulations at three different R values (R = 0; 0.1; 0.2) were performed, and the stress distributions in the channel are plotted in Figure **6.2**. Shear stress distributions at R = 0 (plane Couette flow) indicates that there exist turbulent activities in the channel, due to the presence of Reynolds stress. However, the flow appears to be in transitional state rather than in uniform turbulent regime, which is not unexpected as the Reynolds number is not high. As R is increased, the shear stress distribution moves toward that of

a plane Poiseuille flow, and one can see that the flow has laminarized itself at R = 0.2 as Reynolds stress has become zero.

a)



b)



c)

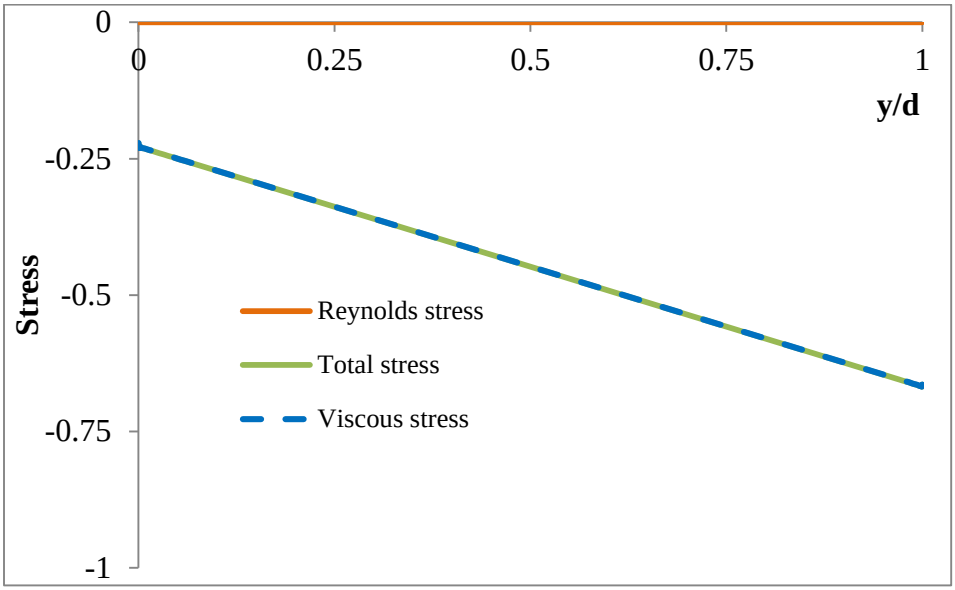


Figure 6.2. Stress distribution in (a) plane Couette flow; Poiseuille-Couette flow with (b) R = 0.1; (c) R = 0.2

Contour plot of streamwise fluctuating velocity at the midway plane y = 0 for the case of plane Couette flow (R=0) clearly reveals the coexistence of turbulent and laminar bands in the channel, as seen in Figure **6.3**. This is consistent with previous findings (52-54) and confirm that our simulation is capable of capturing these patterns. These patterns are even more obvious in Figure **6.4**, which shows that streamwise fluctuating velocity with magnitude of 6 (randomly chosen, including both positive and negative values) in the whole channel is well arranged into bands located at an oblique angle to the streamwise direction.

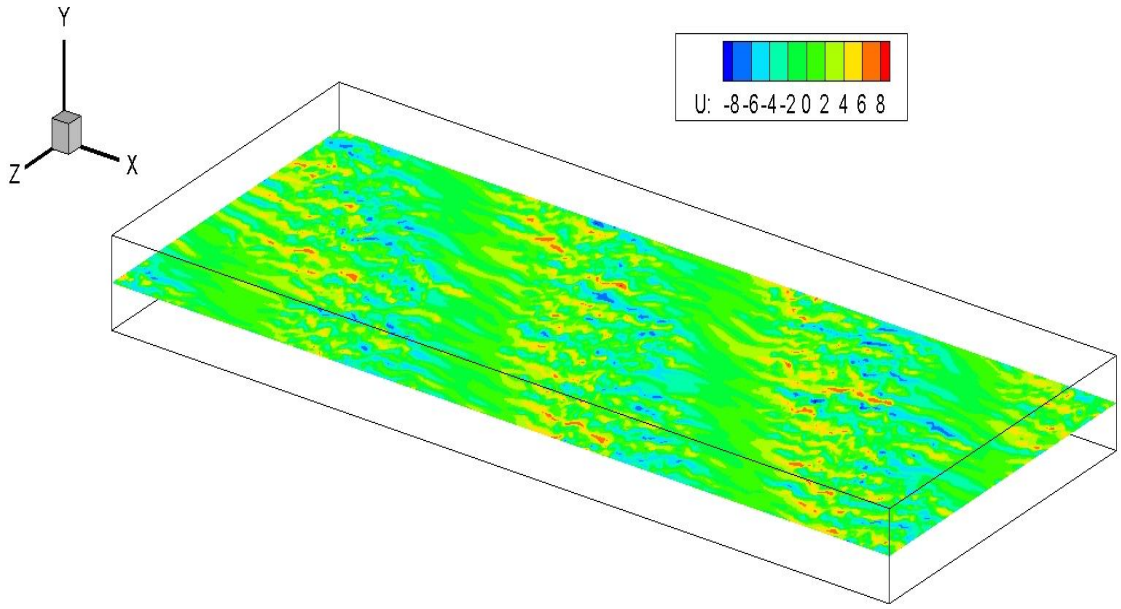


Figure 6.3. Contour plot of streamwise fluctuating velocity at midway plane y = 0 in a plane Couette flow (R=0). X is the streamwise direction

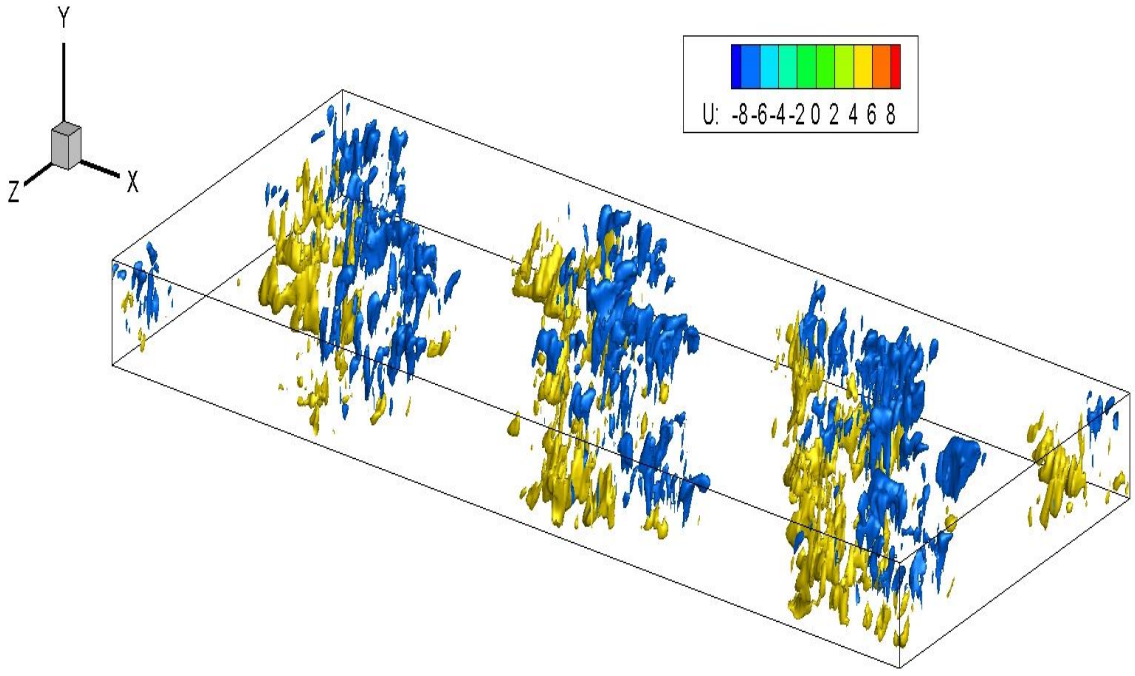


Figure 6.4. Streamwise fluctuating velocity with magnitude of 6 in the Couttle channel flow

These turbulent-laminar patterns, however, fade rapidly as the flow becomes Poiseuille-Couette flow even at small values of R. In Figure **6.5**, it is observed that those patterns have reduced in both quantity and magnitude at the midway plane of the channel as the flow becomes Poiseuille-Couette flow with R = 0.1. Snapshots of fluctuating velocity in streamwise and spanwise directions, shown in Figure **6.6**, also shows the weakening of such patterns.

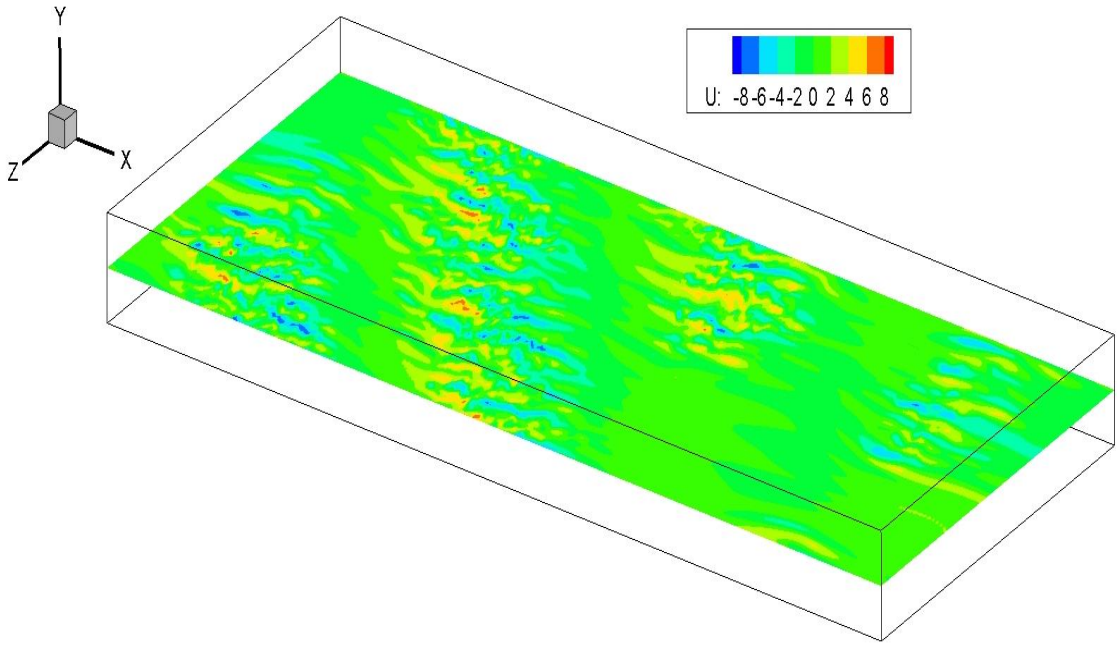


Figure 6.5. Contour plot of streamwise fluctuating velocity at midway plane y = 0 in a plane Poiseuille-Couette flow (R=0.1). X is the streamwise direction

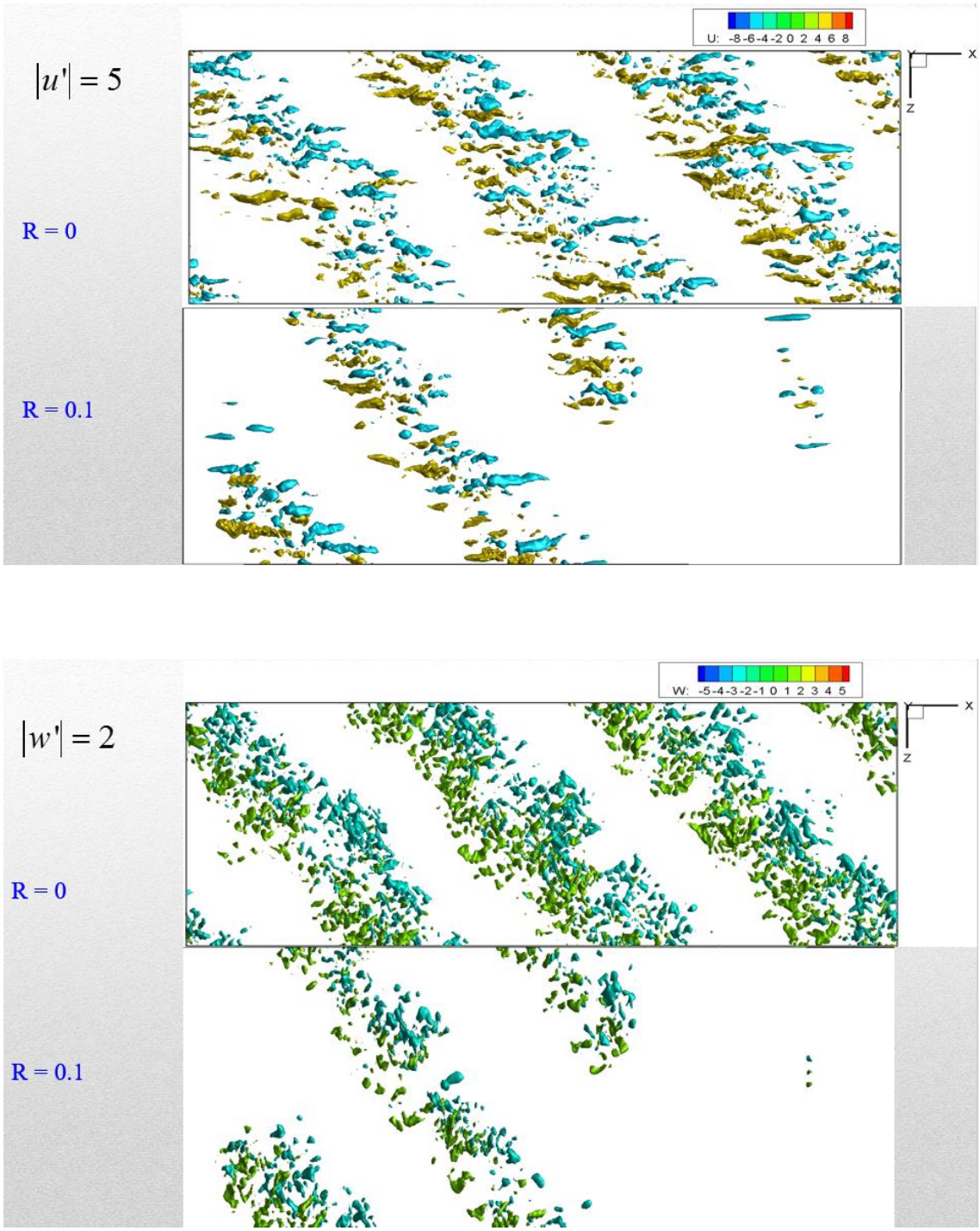


Figure 6.6. Fluctuating velocities in streamwise and spanwise direction at two random magnitude values at the midway plane y = 0 of a plane Couette flow (R=0) and plane Poiseuille-Couette flow (R=0.1)

The results above suggest that as the flow moves from pure Couette flow into Poiseuille-Couette flow at this Reynolds number, laminarization takes place rapidly and lead to weakening, then disappearing, of turbulent activities in the channel. This has led to disappearing of turbulent-laminar patterns as observed above. At R = 0.2, results in Figure **6.2** indicated that there would not be considerable turbulent activity in the channel. Thus, we believe that at R = 0.2, the flow has become laminar and there is no need to conduct further study at higher values of R, as the flow would eventually become laminar Poiseuille flow at R = 1.

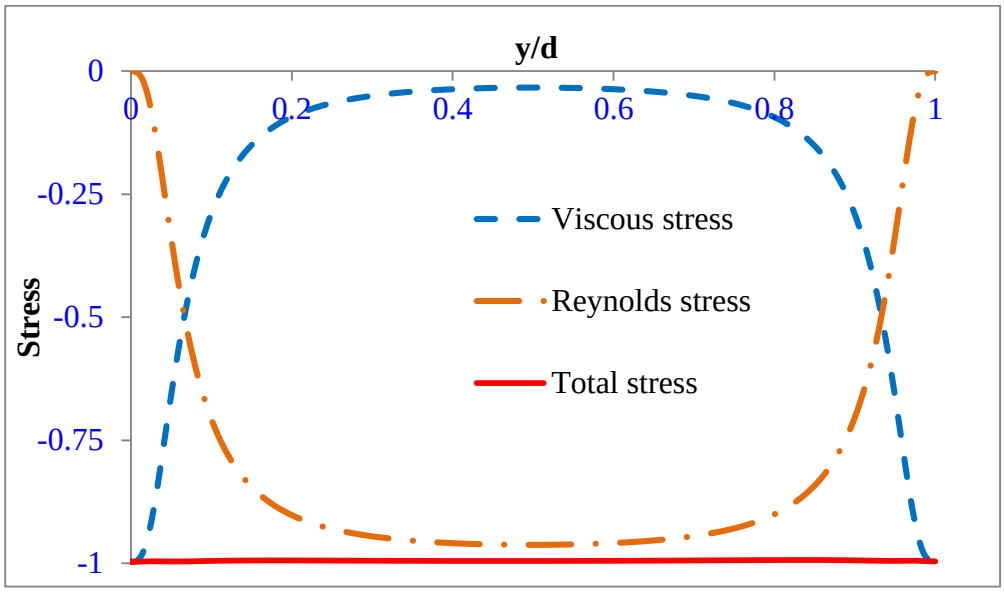
6.3.2 Results at Re = 1247 (Re_τ = 80)

Shear stress distribution in a channel of plane Couette flow (R=0) and Poiseuille-Couette flow (R=0.2; 0.5) is plotted in Figure **6.7**. These results suggest that uniform turbulence was obtained in the plane Couette flow at this Reynolds number. As the flow goes from Couette to Poiseuille-Couette type, the stress distribution profile is also modified toward that in a plane Poiseuille flow, with Reynolds stress still exists at both R = 0.2 and R = 0.5.

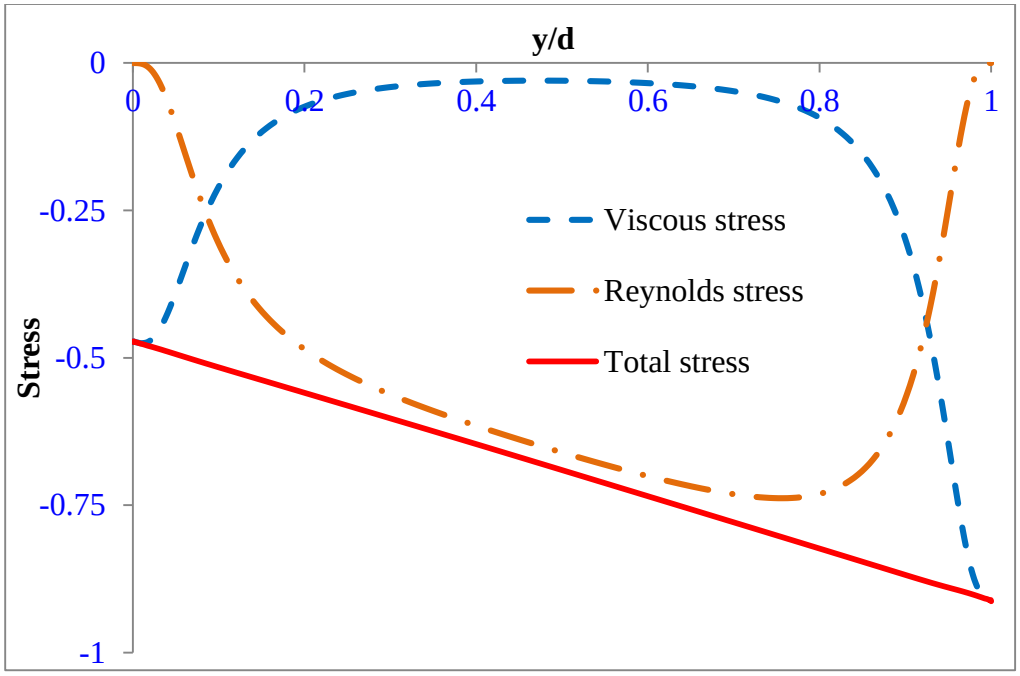
Plotting of streamwise fluctuating velocity at two magnitude values of 4 and 5 in Figure **6.8** and Figure **6.9** reveals interesting finding. High density of turbulent activities for R = 0 indicates that turbulence exist at this Reynolds number for plane Couette flow. As R increases from 0 to 0.5, it is obvious that turbulent intensity is reduced, which is not unexpected after studying the case at Re = 323. However, the most striking feature is that turbulent-laminar patterns seem to be created in a direction which forms an oblique angle to the streamwise direction. This is consistent with previous finding by

Tsukahara (55) who observed existence of turbulent-laminar bands in a Poiseuille flow at similar Reynolds number.

a)



b)



c)

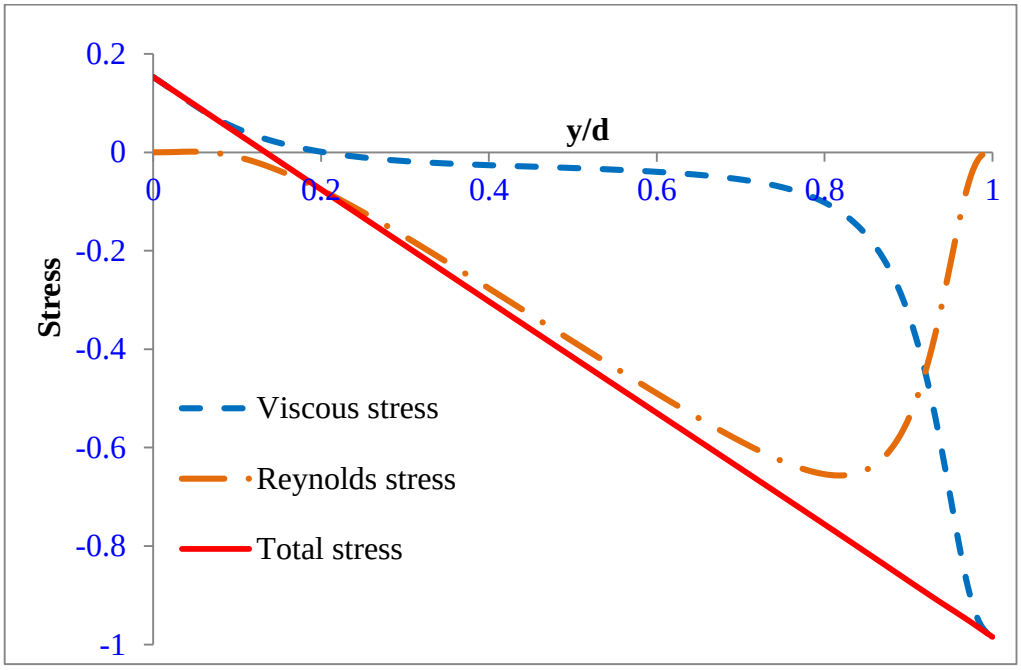


Figure 6.7. Shear stress distribution in (a) plane Couette flow; (b) plane Poiseuille-Couette flow at R = 0.2; (c) plane Poiseuille-Couette flow at R = 0.5

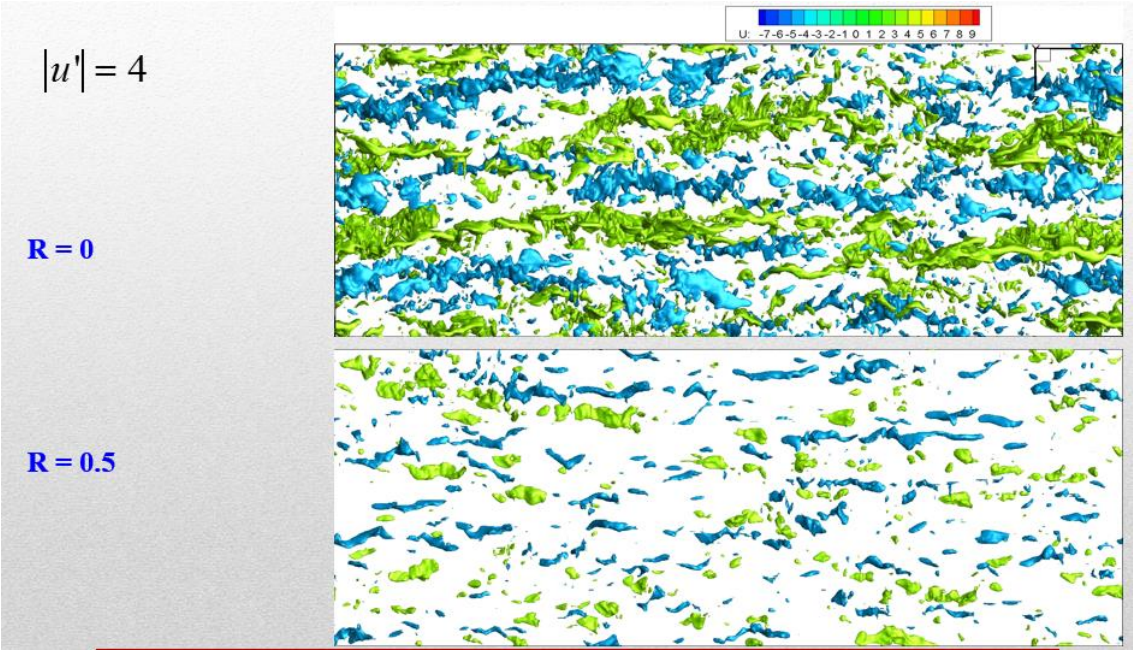


Figure 6.8. Streamwise fluctuating velocity with magnitude of 4 at a midway plane y = 0 in a plane Couette flow (R=0) and plane Poiseuille-Couette flow with R = 0.5

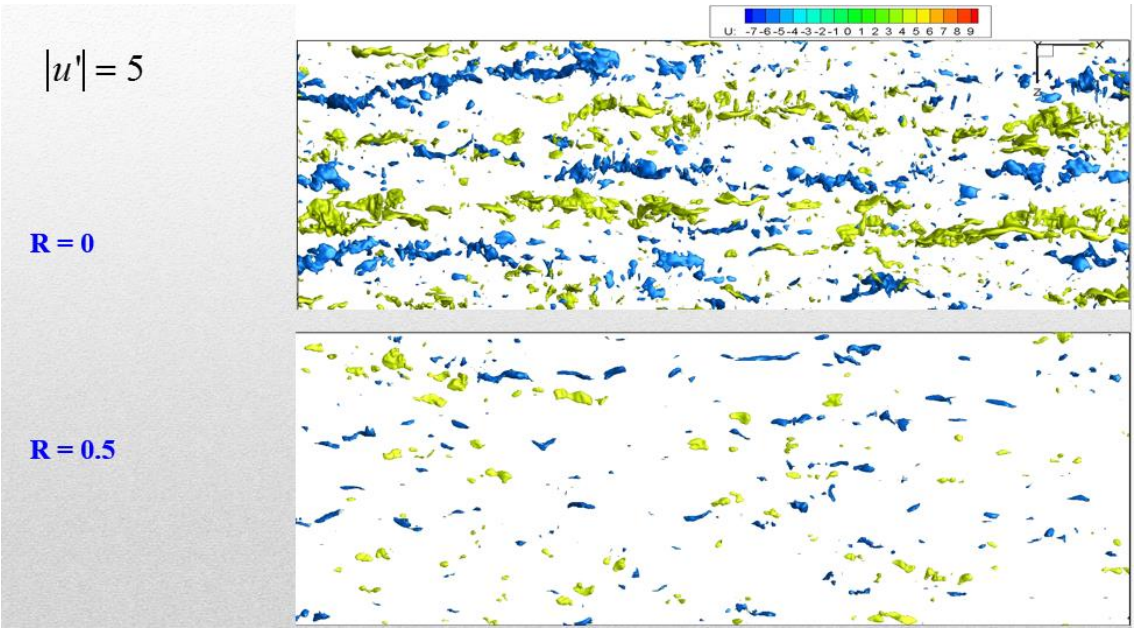


Figure 6.9. Streamwise fluctuating velocity with magnitude of 5 at a midway plane y = 0 in a plane Couette flow (R=0) and plane Poiseuille-Couette flow with R = 0.5

Chapter 7. Conclusions and Future work

7.1 Turbulent drag reduction over Superhydrophobic Surfaces

A significant level of drag reduction has been obtained on surfaces that are models of the behavior of SHSs using direct numerical simulation. Drag reduction is increased as the streamwise slip velocity on the channel wall increases. Certain changes have been observed in the flow structures. Longer, thicker, and weaker eddies appear in the viscous sublayer, compared to those in a flow with no slip and no drag reduction. In the region close to the wall with slip, sweep events that bring fast moving fluid toward the wall are decreased, while ejections taking slow moving fluid away from the wall are enhanced, disrupting the exchange of momentum between the outer flowtoward thewall region. In all three directions, values of fluctuating vorticity are significantly reduced. A similar trend is also observed with the fluctuating velocity dissipation rate. As the slip velocity is increased, the region where the spanwise fluctuating vorticity is larger than the streamwise vorticity expands farther into the center region of the channel.

The suppression of turbulence in the near-wall region is the result of the tendency of wall turbulence towards the one component limit in the Lumley triangle, in agreement with observations for turbulent drag reduction in other situations, most notably in cases of drag reduction with polymer additives. At this limiting state, a significant suppression of small scale turbulence can lead to rapid laminarization and significant drag reduction. The decrease of Reynolds stress, turbulence intensities, TKE production, vorticity, and dissipation rate are then consequences of this suppression.

7.2 Flow-induced separation in wall turbulence

In this work, particles with different diffusivities, represented by passive markers with different Sc, have been found to separate from each other in turbulent flow, under certain conditions. Separation is observed when there are large differences in the particle Sc, and would occur most effectively in cases where the particles are released from sources on the channel wall. An analysis of the stages of development of puff dispersion is the explanation of the mechanism responsible for the separation. A correlation is derived to relate the time at which separation begins to the ratio of the characteristic times of development of the two clouds. This flow-induced separation can be applied to separate microscopic and nanoscopic particles with different sizes, and could be a good solution in separating very small particles especially in very dilute systems. A model, based on Batchelor's extension of the Taylor dispersion theory for shear flows, has been developed to predict mean displacement of particles with different Sc in the streamwise and vertical directions with good agreement to our LST data. It was also found that information about the mean location is not enough to predict particle separation using a high purity criterion. Instead, one should rely on the previously presented correlation to predict separation in channels. The effect of the Reynolds number on flow-induced separation needs to be examined in future work.

7.3 Probability density function of a puff dispersing from the channel wall

The dispersing process of a puff of particles from the channel wall at $Re_\tau = 150$ was closely examined to obtain a probability density function (pdf) that could predict location and concentration distribution of particles in the puff. The Gamma 3P

distribution was found as an appropriate pdf model that satisfies our requirement. Estimation of the three parameters of the Gamma 3P distribution was also successfully obtained, based on the physics behind the dispersing process of the puff from the channel wall. Several calculations have been carried out to demonstrate agreement between results predicted by the Gamma 3P distribution and results generated using DNS/LST approach. The use of Gamma 3P distribution could be found in estimating particles separation at different purify criteria, as well as predicting diffusion of particles in the channel for other applications without employing the more accurate but expensive DNS/LST method.

7.4 Turbulent-Laminar patterns in transitional turbulence

Direct Numerical Simulation of plane Couette flow, Poiseuille flow and Poiseuille-Couette flow has revealed coexistence of turbulent and laminar bands at transitional regime. These turbulent-laminar patterns are unique for their large wavelength and an oblique angel they form with the streamwise direction. Higher level of turbulent activities were observed in Couette flow, compared to Poiseuille-Couette and Poiseuille flow at comparable Reynolds numbers, which is not unexpected due to higher shear rate in Coutte flow. At Re = 323, flow in plane Couette is in transitional regime and consists of turbulent and laminar bands altogether. However, flow in plane Poiseuille and Poiseuille-Couette flow at this Reynolds number appears to be in laminar state and no turbulent spots were observed. At Re = 1247, flow in plane Couette is in turbulent state and coexistence of turbulent and laminar patterns was not observed. As the flow moves from Couette to Poiseuille flow and goes through stages of Poiseuille-

Couette flow, turbulent intensity is reduced which lead to breaking of long coherent structures in streamwise direction and formation of turbulent-laminar patterns in a direction which forms an oblique angel to the streamwise direction.

7.5 Future Work

7.5.1 Flow-induced separation in wall turbulence

Results reported in this study was performed at Re_τ = 300. It is of great interest to examine effects of Reynolds number on the separation ability. It was found that the interplay between convection and diffusion plays an important role in this type of separation technique. Varying Reynolds number would significantly alter the interplay, thus lead to different results in separation ability. The project could be expanded to determine the optimum Reynolds number for separation, corresponding to a certain range of Sc numbers.

7.5.2 Probability density function of a puff dispersing from the channel wall

The Gamma 3P distribution was found in this study to be capable of predicting concentration distribution of a puff of particles dispersing from the channel wall at Re_τ=150. All the parameters of the model were calculated based on the physics behind dispersion of the puff. However, the Gamma 3P distribution model was found to work well for short time (t^+ up to 100). This study could be expanded to longer time when convection plays a more important role. The physics behind the dispersion would be different at large time, and may require use of a different pdf model. However, success in obtaining an appropriate pdf model at large time would help reduce computing cost

significantly and could help with other applications where downstream activities are mostly concerned.

Bibliography

1. Goldstein S (1965) *Modern Developments in Fluid Dynamics: An Account of Theory and Experiment Relating to Boundary Layers, Turbulent Motion and Wakes* (New York: Dover).
2. Batchelor GK (1985) *An Introduction to Fluid Dynamics* (Cambridge University Press).
3. Navier CLMH (1823) Mémoire sur les lois du Mouvement des Fluides. *Mem. Acad. R. Sci. Inst. France*:389-440.
4. Maxwell JC (1879) On stresses in rarified gases arising from inequalities of temperature. *Phil. Trans. R. Soc. Lond.*:231-256.
5. Rothstein JP (2010) Slip on Superhydrophobic Surfaces. *Annual Review of Fluid Mechanics* 42:89.
6. Lauga E & Stone HA (2003) Effective slip in pressure-driven Stokes flow. *Journal of Fluid Mechanics* 489:55-77.
7. Feuillebois F, Bazant MZ, & Vinogradova OI (2009) Effective Slip over Superhydrophobic Surfaces in Thin Channels. *Physical Review Letters* 102(2):026001.
8. Vinogradova OI (1999) Slippage of water over hydrophobic surfaces. *International Journal of Mineral Processing* 56(1-4):31-60.
9. JN I (1992) *Intermolecular and Surface Forces* (London: Academic).
10. Thompson PA & Troian SM (1997) A general boundary condition for liquid flow at solid surfaces. *Nature* 389:360-362.
11. Barrat J-L & Bocquet L (1999) Large Slip Effect at a Nonwetting Fluid-Solid Interface. *Physical Review Letters* 82(23).
12. Li H, *et al.* (2001) Super-"Amphiphobic" Aligned Carbon Nanotube Films. *Angew. Chem. Int. Ed. 2001* 40:1743-1746.
13. Bhushan B & Jung YC (2008) Wetting, adhesion and friction of superhydrophobic and hydrophilic leaves and fabricated micro/nanopatterned surfaces. *Journal of Physics: Condensed Matter* 20(22).
14. Nosonovsky M & Bhushan B (2008) Roughness-induced superhydrophobicity: a way to design non-adhesive surfaces. *Journal of Physics: Condensed Matter* 20(22).
15. Que're' D & Reyssat M (2008) Non-adhesive lotus and other hydrophobic materials. *Philosophical Transactions of the Royal Society A* 366:1539.
16. Barthlott W & Neinhuis C (1997) Purity of the sacred lotus, or escape from contamination in biological surfaces. *Planta* 202(1).
17. Koch K, Bhushan B, & Barthlott W (2008) Diversity of structure, morphology and wetting of plant surfaces. *Soft Matter*.
18. Wagner P, Furstner R, Barthlott W, & Neinhuis C (2003) Quantitative assessment to the structural basis of water repellency in natural and technical surfaces. *Journal of Experimental Botany* 54(385):1295-1303.
19. Bhushan B & Jung YC (2006) Micro- and nanoscale characterization of hydrophobic and hydrophilic leaf surfaces. *Nanotechnology* 17(11).
20. Onda T, Shibuichi S, Satoh N, & Tsujii K (1996) Super-Water-Repellent Fractal Surfaces. *Langmuir* 12(9):2125-2127.

21. R B (2003) Self-cleaning surfaces--virtual realities. *Nat Mater* 2:301-306.
22. McHale G, Shirtcliffe NJ, & Newton MI (2004) Contact-Angle Hysteresis on Super-Hydrophobic Surfaces. *Langmuir* 20:10146-10149.
23. Bico J, Marzolin C, & Quere D (1999) Pearl drops. *Europhysics Letters* 47.
24. Chen W, *et al.* (1999) Ultrahydrophobic and Ultralyophobic Sufaces: Some comments and examples. *Langmuir* 15:3395-3399.
25. Sakai M, *et al.* (2006) Direct observation of internal fluidity in a water droplet during sliding on hydrophobic surfaces. *Langmuir* 22:4906-4909.
26. Ou J, Perot B, & Rothstein JP (2004) Laminar drag reduction in microchannels using ultrahydrophobic surfaces. *Physics of Fluids* 16(12):4635-4643.
27. Ou J & Rothstein JP (2005) Direct velocity measurements of the flow past drag-reducing ultrahydrophobic surfaces. *Physics of Fluids* 17(10).
28. Gogte S, *et al.* (2005) Effective slip on textured superhydrophobic surfaces. *Physics of Fluids* 17(5):051701.
29. Tretheway DC & Meinhart CD (2002) Apparent fluid slip at hydrophobic microchannel walls. *Physics of Fluids* 14(3).
30. Choi C-H & Kim C-J (2006) Large Slip of Aqueous Liquid Flow over a Nanoengineered Superhydrophobic Surface. *Physical Review Letters* 96(6):066001.
31. Min T & Kim J (2004) Effects of hydrophobic surface on skin-friction drag. *Physics of Fluids* 16(7).
32. Martell MB, Perot JB, & Rothstein JP (2009) Direct numerical simulations of turbulent flows over superhydrophobic surfaces. *Journal of Fluid Mechanics* 620:31-41.
33. Martell MB, Rothstein JP, & Perot JB (2010) An analysis of superhydrophobic turbulent drag reduction mechanisms using direct numerical simulation *Physics of Fluids* 22(6):065102.
34. Daniello RJ, Waterhouse NE, & Rothstein JP (2009) Drag reduction in turbulent flows over superhydrophobic surfaces. *Physics of Fluids* 21.
35. Philip JR (1972) Flows satisfying mixed no-slip and no-shear conditions. *Journal of Applied Mathematics and Physics* 23.
36. Philip JR (1972) Integral Properties of Flows Satisfying Mixed No-slip and No-shear conditions. *Journal of Applied Mathematics and Physics* 23.
37. Nakabayashi K, Kitoh O, & Katoh Y (2004) Similarity laws of velocity profiles and turbulence characteristics of Couette-Poiseuille turbulent flows. *Journal of Fluid Mechanics* 507:43-69.
38. Thurlow EM & Klewicki JC (2000) Experimental study of turbulent Poiseuille-Couette flow. *Physics of Fluids* 12(4):865-875.
39. Spencer NB, Lee LL, Parthasarathy RN, & Papavassiliou DV (2009) Turbulence structure for plane Poiseuille-Couette flow and implications for drag reduction over surfaces with slip. *The Canadian Journal of Chemical Engineering* 87:38.
40. Einstein A (1905) Uber die von der molekular-kinetischen Theorie der Warme geforderte Bewegung von in ruhenden Flussigkeiten suspendierten Teilchen. *Annales de Physique* 17:549.
41. I. TG (1921) Diffusion by continuous movements. *Proceedings of the London Mathematical Society* 24A.

42. Saffman PG (1960) On the effect of molecular diffusivity in turbulent diffusion. *Journal of Fluid Mechanics* 8:273-283.
43. Corrsin S (1959) Progress report on some turbulent diffusion research. *Advanced Geophysics* 6:161-164.
44. Hanratty TJ (1956) Heat transfer through a homogeneous isotropic turbulent field. *AIChE Journal* 2.
45. Prigent A, Gregoire G, Chate H, & Dauchot O (2003) Long-wavelength modulation of turbulent shear flows. *Physica D* 174:100-113.
46. Prigent A, Gregoire G, Chate H, Dauchot O, & Saarloos Wv (2002) Large-scale finite-wavelength modulation within turbulent shear flows. *Physical Review Letters* 89(1).
47. Coles D (1965) Transition in circular Couette flow. *Journal of Fluid Mechanics* 21(3):385-425.
48. Atta CV (1966) Exploratory measurements in spiral turbulence. *Journal of Fluid Mechanics* 25(3):495-512.
49. Andereck CD, Liu SS, & Swinney HL (1986) flow regimes in a circular couette system with independently rotating cylinders. *Journal of Fluid Mechanics* 164:155-183.
50. Hegseth JJ, Andereck CD, Hayot F, & Pomeau Y (1989) Spiral turbulence and phase dynamics. *Physical Review Letters* 62(3).
51. Goharzadeh A & Mutabazi I (2001) Experimental characterization of intermittency regimes in the Couette-Taylor system. *The European Physical Journal B* 19:157-162.
52. Barkley D & Tuckerman LS (2005) Computational Study of Turbulent Laminar Patterns in Couette Flow. *Physical Review Letters* 94.
53. Barkley D & Tuckerman LS (2007) Mean flow of turbulent-laminar patterns in plane Couette flow. *Journal of Fluid Mechanics* 576:109-137.
54. Barkley D & Tuckerman LS (2011) Patterns and dynamics in transitional plane Couette flow. *Physics of Fluids* 23.
55. Tsukahara T, Seki Y, Kawamura H, & Tochio D (2005) DNS of turbulent channel flow at very low Reynolds numbers. *Proceedings of the Fourth International Symposium on Turbulence and Shear Flow Phenomena*:935-940.
56. Dong S (2009) Evidence for internal structures of spiral turbulence. *Physical Review E* 80.
57. Dong S & Zheng X (2011) Direct numerical simulation of spiral turbulence. *Journal of Fluid Mechanics* 668.
58. Meseguer A, Mellibovsky F, Avila M, & Marques F (2009) Instability mechanisms and transition scenarios of spiral turbulence in Taylor-Couette flow. *Physical Review E* 80.
59. Kim J, Moin P, & Moser R (1987) Turbulence statistics in fully developed channel flow at low Reynolds number. *Journal of Fluid Mechanics* 177:133-166.
60. Kuroda A, Tomita Y, & Kasagi N (1992) Direct Numerical Simulation of Passive Scalar Field in a Turbulent Channel Flow. *Journal of Heat Transfer* 114(3).

61. Moin P & Mahesh K (1998) Direct Numerical Simulation: a tool in turbulence research. *Annual Review of Fluid Mechanics* 30(1).
62. Kasagi N & Shikazono N (1995) Contribution of Direct Numerical Simulation to Understanding and Modelling Turbulent Transport. *Proceedings: Mathematical and Physical Sciences* 451.
63. Lyons SL, Hanratty TJ, & McLaughlin JB (1991) Large-scale computer simulation of fully developed turbulent channel flow with heat transfer. *International Journal for Numerical Methods in Fluids* 13:999-1028.
64. Gunther A, Papavassiliou DV, Warholic MD, & Hanratty TJ (1998) Turbulent flow in a channel at a low Reynolds number. *Experiments in Fluids* 25(5-6):503-511.
65. Le PM & Papavassiliou DV (2005) Turbulent Dispersion from Elevated Line Sources in Channel and Couette Flow. *AIChE Journal* 51(9):2402-2414.
66. Papavassiliou DV & Hanratty TJ (1997) Interpretation of large-scale structures observed in a turbulent plane Couette flow. *International Journal of Heat and fluid flow* 18(1):55-69.
67. Papavassiliou DV & Hanratty TJ (1997) Transport of a passive scalar in a turbulent channel flow. *International Journal of Heat and Mass Transfer* 40:9.
68. Papavassiliou DV & Hanratty TJ (1995) The use of Lagrangian methods to describe turbulent transport of heat from a wall. *Ind. Eng. Chem. Res.* 34:3359-3367.
69. Srinivasan C & Papavassiliou DV (2011) Direction of scalar transport in turbulent channel flow. *Physics of Fluids* 23(11).
70. Srinivasan C & Papavassiliou DV (2011) Prediction of the turbulent Prandtl number in wall flows with Lagrangian simulations. *Industrial & Engineering Chemistry Research* 50.
71. Kontomaris K & Hanratty TJ (1992) An Algorithm for Tracking fluid particles in a spectral simulation of turbulent channel flow. *Journal of Computational Physics* 103(2).
72. Srinivasan C & Papavassiliou DV (2011) Direction of scalar transport in turbulent channel flow. *Phys. Fluids* 23:115105.
73. Karna AK & Papavassiliou DV (2012) Near-wall velocity structures that drive turbulent transport from a line source at the wall. *Phys. Fluids* 24:035102.
74. Papavassiliou DV (2002) Turbulent transport from continuous sources at the wall of a channel *International Journal of Heat and Mass Transfer* 45:14.
75. Papavassiliou DV (2002) Scalar dispersion from an instantaneous line source at the wall of a turbulent channel for medium and high Prandtl number fluids. *International Journal of Heat and fluid flow* 23:12.
76. Srinivasan C & Papavassiliou DV (2011) Prediction of the Turbulent Prandtl Number in Wall Flows with Lagrangian Simulations. *Ind. Eng. Chem. Res.* 50:8881.
77. Mitrovic BM & Papavassiliou DV (2003) Transport Properties for Turbulent Dispersion from Wall Sources. *AIChE Journal* 49(5).
78. Hanjalic K & Launder BE (1972) Fully developed asymmetric flow in a plane channel *Journal of Fluid Mechanics* 51:301-335.

79. Kuroda A & Kasagi N (DNS Database of Turbulence and Heat Transfer. http://www.thtlab.t.u-tokyo.ac.jp/.
80. Stone PA, Waleffe F, & Graham MD (2002) Toward a Structural Understanding of Turbulent Drag Reduction: Nonlinear Coherent States in Viscoelastic Shear Flows. *Physical Review Letters* 89(20):208301.
81. Li W & Graham MD (2007) Polymer induced drag reduction in exact coherent structures of plane Poiseuille flow. *PHysics of Fluids* 19(8):083101.
82. Fukagata K, Kasagi N, & Koumoutsakos P (2006) A theoretical prediction of friction drag reduction in turbulent flow by superhydrophobic surfaces. *Physics of Fluids* 18(5):051703.
83. Housiadas KD & Beris AN (2005) Direct numerical simulations of viscoelastic turbulent channel flows at high drag reduction. *Korea-Australia Rheology Journal* 17(3):131.
84. Lombardi P, Angelis VD, & Banerjee S (1996) Direct numerical simulation of near-interface turbulence in coupled gas-liquid flow. *Physics of Fluids* 8(6):1643.
85. Panton RL (1997) *Self-sustaining Mechanisms of Wall Turbulence* (Computational Mechanics Publications, Southampton).
86. Lumley JL & Newman GR (1977) The return to isotropy of homogeneous turbulence *Journal of Fluid Mechanics* 82:161-178.
87. Jovanovic J & Hillerbrand R (2005) On peculiar property of the velocity fluctuations in wall-bounded flows. *Thermal Science* 9(1):3-12.
88. George WK & Hussein HJ (1991) Locally Axisymmetric Turbulence. *J. Fluid Mech.* 233:1-23.
89. Laufer J (1982) Flow Instability and Turbulence. *Structure of Turbulence in Heat and Mass transfer*.
90. Dimitropoulos CD, Sureshkumar R, & Beris AN (1998) Direct Numerical Simulation of Viscoelastic Turbulent Channel Flow Exhibiting Drag Reduction: Effect of the Variation of Rheological Parameters. *Journal of Non-Newtonian Fluid Mechanics* 79:433-468.
91. Tamano S, Graham MD, & Morinishi Y (2011) Streamwise variation of turbulent dynamics in boundary layer flow of drag-reducing fluid. *Journal of Fluid Mechanics* 686:352.
92. Sajeesh P & Sen AK (2013) Particle separation and sorting in microfluidic devices: a review. *Microfluid Nanofluid*.
93. Oakey J, Allely J, & Marr DWM (2002) Laminar-Flow-Based Separations at the Microscale. *Biotechnol. Progr.* 18:1439.
94. Takagi J, Yamada M, Yasuda M, & Seki M (2005) Continuous particle separation in a microchannel having asymmetrically arranged multiple branches. *Lab on a Chip* 5:778-784.
95. Yamada M, Nakashima M, & Seki M (2004) Pinched Flow Fractionation: Continuous Size Separation of Particles Utilizing a Laminar Flow Profile in a Pinched Microchannel. *Anal. Chem.* 76:5465-5471.
96. Park JS & Jung HI (2009) Multiorifice Flow Fractionation: Continuous Size-Based Separation of Microspheres Using a Series of Contraction/Expansion Microchannels. *Anal. Chem.* 81:8280-8288.

97. Bhagat AAS, Kuntaegowdanahalli SS, & Papautsky I (2008) Enhanced particle filtration in straight microchannels using shear-modulated inertial migration. *Phys. Fluids* 20(10):101702.
98. Crowley TA & Pizziconi V (2005) Isolaiton of plasma from whole blood using planar microfilters for lab-on-a-chip applications. *The Royal Society of Chemistry 2005* 5:922-929.
99. Redkar SG & Davis RH (1995) Cross-Flow Microfiltration with High-Frequency Reverse Filtration. *American Institute of Chemical Engineering Journal* 41(3):501.
100. Kuberkar V, Czekaj P, & Davis R (1998) Flux enhancement for membrane filtration of bacterial suspensions using high-frequency backpulsing. *Biotechnol. Bioeng.* 60(1):77-97.
101. Aran K, *et al.* (2011) microfiltration platform for continuous blood plasma protein extraction from whole blood during cardiac surgery. *Lab Chip* 11:2858-2868.
102. Lo Mc & Zahn JD (2012) Development of a multi-compartment microfiltration device for particle fractionation. *16th international conference on miniaturized systems for chemistry and life sciences*.
103. Yamada M & Seki M (2005) Hydrodynamic filtration for on-chip particle concentration and classification utilizing microfluidics. *The Royal Society of Chemistry 2005* 5:1233-1239.
104. Yamada M & Seki M (2006) Microfluidic Particle Sorter Employing Flow Splitting and Recombining. *Anal. Chem.* 78:1357-1362.
105. Wang X-B, *et al.* (2000) Cell separation by Dielectrophoretic Field-flow-fractionation. *Analytical Chemistry (Washington)* 72(4).
106. Gaal O (1980) *Electrophoresis in the Separation of Biological Macromolecules* (John Wiley & Sons Ltd).
107. Gascoyne PRC & Vykoukal J (2002) Particle separation by dielectrophoresis. *Electrophoresis* 23:1973-1983.
108. Gagnon ZR (2011) Cellular dielectrophoresis: Applications to the characterization, manipulation, separation and patterning of cells. *Electrophoresis* 32(18):2466-2487.
109. Gimbert LJ, Haygarth PM, Beckett R, & Worsfold PJ (2005) Comparison of Centrifugation and Filtration Techniques for the Size fractionation of colloidal material in soil suspensions using sedimentation field flow fractionation. *Environmental Science & Technology* 39(6):5.
110. Juen S, *et al.* (1992) Technology and photoluminescence of GaAs Micro-and Nanocrystallites. *Superlattices and Microstructures* 11(2).
111. Giddings JC (1973) The Conceptual Basis of Field-Flow Fractionation. *J. Chem. Educ.* 50(10).
112. Giddings JC (1993) Field-Flow Fractionation: Analysis of Macromolecular, Colloidal, and Particulate Materials. *Science* 260:1456-1465.
113. Giddings JC, Yang FJF, & Myers MN (1976) Flow Field-Flow Fractionation: A Versatile New Separation Method. *Science* 193:1244.
114. Lenshof A & Laurell T (2010) Continuous separation of cells and particles in microfluidic systems. *Chem. Soc. Rev.* 39:1203-1217.

115. Valino L, Dopazo C, & Ros J (1994) Quasistationary Probability Density Functions in the Turbulent Mixing of a Scalar Field. *Physical Review Letters* 72(22).
116. Shraiman BI & Siggia ED (1996) Symmetry and Scaling of Turbulent Mixing. *Physical Review Letters* 77(12).
117. Schumacher J & Sreenivasan KR (2003) Geometric Features of the Mixing of Passive Scalars at High Schmidt Numbers. *Physical Review Letters* 91(17).
118. Rivera MK & Ecke RE (2005) Pair Dispersion and Doubling Time Statistics in Two-Dimensional Turbulence. *Physical Review Letters* 95(19):194503.
119. Ott S & Mann J (2000) An experimental investigation of the relative diffusion of particle pairs in three-dimensional turbulent flow. *Journal of Fluid Mechanics* 422:17.
120. Snyder WH & Lumley JL (1971) Some measurements of particle velocity autocorrelation functions in a turbulent flow. *Journal of Fluid Mechanics* 48:31.
121. Beck C (2007) Statistics of Three-Dimensional Lagrangian Turbulence. *Physical Review Letters* 98(6):064502.
122. Bourgoin M, Ouellette NT, Xu H, Berg J, & Bodenschatz E (2006) The role of pair dispersion in turbulent flow. *Science* 311:4.
123. Chaves M, Eyink G, Frisch U, & Vergassola M (2001) Universal Decay of Scalar Turbulence. *Physical Review Letters* 86(11):2305-2308.
124. Shlien DJ & Corrsin S (1976) Dispersion measurements in a turbulent boundary layer. *Int. J. Heat Mass Transfer* 19:285-295.
125. Poreh M & Cermak JE (1964) Study of the diffusion from a line source in turbulent boundary layer. *Int. J. Heat Mass Transfer* 7:1083-1095.
126. Bird RB, Stewart WE, & Lightfoot EN (2006) *Transport Phenomena* (Wiley) 2 Ed.
127. Berg HC (1993) *Random Walks in Biology* (Princeton University Press, Princeton, NJ).
128. Harvey RA, Champe PC, & Fisher BD (2007) *Microbiology* (Lippincott Williams & Wilkins).
129. Batchelor GK (1964) Diffusion from sources in a turbulent boundary layer. *Archiwum Mechaniki Stosowanej* 3.
130. Cermak JE (1963) Lagrangian similarity hypothesis applied to diffusion in turbulent shear flow. *Journal of Fluid Mechanics* 15:16.
131. Malhotra RC & Cermak JE (1963) Wind-tunnel modelling of atmospheric diffusion. *Journal of Geophysical Research* 68(8):4.
132. Deardorff JW (1974) Differences between eddy coefficients for instantaneous and continuous vertical diffusion into the neutral surface layer. *Boundary-Layer Meteorology* 5:7.
133. Watanabe T, Sakai Y, Nagata K, & Hayase T (2015) Turbulent mixing of passive scalar near turbulent and non-turbulent interface in mixing layers. *Physics of Fluids* 27(8).
134. Eswaran V & Pope SB (1988) Direct Numerical Simulations of the turbulent mixing of a passive scalar. *Physics of Fluids* 31(3).
135. Biferale L, *et al.* (2005) Lagrangian statistics of particle pairs in homogeneous isotropic turbulence. *Physics of Fluids* 17(11).

136. Nguyen Q, Srinivasan C, & Papavassiliou DV (2015) Flow-induced separation in wall turbulence. *Physical Review E* 91.
137. Shlien DJ & Corrsin S (1976) Dispersion measurements in a turbulent boundary layer. *International Journal of Heat and Mass Transfer* 19.
138. Poreh M & Cermak JE (1964) Study of diffusion from a line source in a turbulent boundary layer. *International Journal of Heat and Mass Transfer* 7.
139. Karna AK & Papavassiliou DV (2012) Near-wall velocity structures that drive turbulent transport from a line source at the wall. *Physics of Fluids* 24(3).
140. Papavassiliou NHPRSVNRTDV (2014) Bulk stress distributions in the pore space of sphere-packed beds under Darcy flow conditions. *Physical Review E* 89.
141. Papavassiliou RSVSBVVISDV (2010) Distribution of flow-induced stresses in highly porous media. *Applied Physics Letters* 97.
142. Ehrlich SHDDMPR (1988) Distribution of the Bay Checkerspot Butterfly, Euphydryas editha bayensis: Evidence for a Metapopulation Model. *The American Naturalist* 132(3).